A Tunable Dual-Species Rubidium-Argon Beam Source for Controlled Doped Cryogenic Crystal Growth

Senior Honors Thesis

Department of Physics and Astronomy
Northwestern University

Isaac K. Cross

Advisor: Prof. Brian C. Odom

2026

Abstract

Doped cryogenic noble gas crystals are a promising platform for precision measurement, easily offering on order $\rho \sim 10^{16}$ dopants/cm^3 to be probed simultaneously, and have the potential for competitive electron electric dipole moment (eEDM) sensitivity. However, current crystals suffer from short inhomogeneous coherence times $T_2^* \sim 10$–100 μs that are 10^3–10^4 times shorter than the homogeneous limit $T_2 \sim 0.1$ s, severely undermining their statistical advantage. To systematically investigate the relationship between crystal growth conditions and coherence, I have developed a novel, tunable dual-species Rubidium-Argon beam source utilizing a nozzle array of 231 microcapillaries (ID = 100 μm, $L = 7.62$ mm) that co-deposits a collimated mixed Rb-Ar beam onto a cryogenic substrate, with independent flux control over both species via a calibrated mass-flow controller and a heated Rb reservoir with variable-conductance leak valve. Characterization via 780 nm absorption spectroscopy of the ^{85}Rb D_2 line yields a conservative approximate beam half-angle divergence of $\theta_{1/2} = 1.4 \pm 0.6°$, a total Rb flux of approximately 2.5–3.0×10^{10} atoms/s, a capture efficiency of $23 - 41\%$ at the growth substrate, and an inferred dopant density of order 10^{17} atoms/cm^3 and crystal growth at $\sim$2 μm/hr at current operating conditions. In a complementary study, a Monte Carlo simulation of dipole-dipole-induced inhomogeneous broadening demonstrates that at the densities typical of existing doped rare-gas crystals ($\rho \lesssim 10^{16}$ atoms/cm^3), dipolar interactions predict linewidths nearly two orders of magnitude smaller than observed, identifying structural disorder and multiple trapping sites as the dominant decoherence mechanism, while also establishing that a target density of $\rho \sim 10^{15}$ atoms/cm^3 in structurally improved crystals would be sufficient to reach dipolar-limited T_2^* in the millisecond regime.

Contents

1 Introduction and Overview **1**

2 Background: Doped Cryogenic Noble Gas Crystals **2**

2.1 Promise of the Platform: High Density and Statistical Power 3

2.2 Coherence in Doped Crystals 4

2.2.1 What Limits T_2^* 5

2.3 Odom Lab's Goal: Improved Crystal Quality → Improved Coherence Time 6

3 Beam Source **7**

3.1 Crystal Growth Chamber and Design Constraints 7

3.2 Design Overview 8

3.3 Nozzle Design: Microcapillary Array 8

3.3.1 Flow Regime and Beam Divergence 9

3.3.2 Crystal Growth Rate and Conductance 10

3.3.3 Dopant Density 11

3.3.4 Nozzle Parameters and Array Geometry 12

3.3.5 CAD Design and Machining 13

3.3.6 Microcapillary Assembly and Loading 14

3.4 Rubidium Dopant Source 17

3.4.1 Rb Reservoir and Vapor Pressure Control 17

3.4.2 Rb Loading Procedure 18

3.5 Custom Nichrome Heaters 18

3.5.1 Nozzle Heater 19

3.5.2 Rb Heaters 21

3.6 Argon Gas Handling System 21

3.6.1 Impurity Estimates 23

3.7 Beam Source Full Assembly 25

4 Beam Characterization: Setup and Methods **27**
4.1 Rb-Ar Beam Characterization Chamber . . . 27
4.2 Rubidium Absorption Spectroscopy: Optical Setup . . . 29
4.2.1 Laser source and controller . . . 29
4.2.2 Probing Desired Transition . . . 29
4.2.3 Spatial scanning and periscope system . . . 30
4.2.4 780 nm Probe Beam Characterization . . . 31
4.3 Signal Conditioning: Filter-Amplifier Circuit . . . 34
4.3.1 Validity of Conditioned Signal for Relative Absorption . . . 35
4.4 Data Acquisition and Analysis Pipeline . . . 36
4.5 Divergence Measurement . . . 37
4.5.1 Capture Efficiency . . . 39
4.6 Flux Measurement . . . 39
4.6.1 Column Density from Beer-Lambert Law . . . 40
4.6.2 Linear Density and Flux . . . 41
4.6.3 Isotopic and Hyperfine Population Corrections . . . 41

5 Beam Characterization: Results and Discussion **43**
5.1 Beam Divergence: Pure Rubidium . . . 44
5.1.1 Method A: Single-Zone Nozzle Geometry . . . 44
5.1.2 Method B: Two-Zone Differential . . . 46
5.2 Beam Divergence: Dual-Species Rb-Ar Beam . . . 46
5.3 Discussion: Fit Model and Data Quality . . . 48
5.4 Discussion: Mean Free Path and Flow Regime . . . 49
5.5 Summary and Discussion of Results . . . 50
5.5.1 Example Crystal Growth . . . 51

6 Spin-Spin Interaction Broadening: Monte Carlo Simulation **53**
6.1 Spin-Spin Interaction Model . . . 54
6.1.1 Transition frequency and Zeeman coefficient . . . 54
6.1.2 Dipole magnetic field . . . 55
6.2 Monte Carlo Method . . . 55
6.2.1 Sampling dopant configurations . . . 55
6.2.2 Assigning spin states and orientations . . . 55
6.2.3 Computing the field and frequency shift . . . 57
6.2.4 Extracting the linewidth and T_2^* . . . 57
6.3 Verifying Simulation Against Analytic Estimate . . . 58

6.3.1 Comparing Simulation to Analytic Estimate 59
6.4 Results 60
6.4.1 Sensitivity to simulation parameters 60
6.4.2 Comparison to experimental data 60
6.5 Discussion and Limitations 63
6.5.1 Implications for the dominant broadening mechanism 63
6.5.2 Consequences for growing Rb doped-crystals 64
6.5.3 Model limitations 65

A Cad Drawings **71**

B Rubidium **73**

C Rubidium Absorption Data **75**
C.0.1 Rb Beam 75
C.0.2 Rb-Ar Beam 75
C.0.3 Comparison of All Beam Profile Plots 75

D Dipole-Dipole Broadening Monte Carlo Simulation Code **81**

List of Figures

2.1 Artistic rendition of an alkali-doped rare-gas crystal. The blue array represents the host rare-gas lattice, while the red spheres with arrows represent embedded dopant atoms and their spin. 3

3.1 Schematic cross-section of the dual-species beam source. Ar is admitted through a mass-flow controller and mixed with Rb vapor from the heated reservoir before both species pass through the microcapillary nozzle array and travel $\sim$0.5 m to the cryogenic growth substrate. 8

3.2 Microcapillary array nozzle from Senaratne et al. [17], showing the triangular capillary bundle clamped into a CF flange. 9

3.3 Estimated growth rate as a function of oven pressure and temperature for the $N_{\text{rows}} = 21$ nozzle. The solid black line marks $\lambda_{Ar} = ID_{\text{cap}}$ and the dashed black line marks $\lambda_{Ar} = 10\,ID_{\text{cap}}$; the desired operating regime lies below one of these boundaries, but it is currently unclear which. Chapter 5 argues we are currently able to operate to at least $\lambda_{Ar} = 20\,ID_{\text{cap}}$ (Eq. 5.3) 13

3.4 Same as Fig. 3.3 but with the color scale zoomed to the lower growth-rate regime accessible when enforcing $\lambda_{Ar} \gtrsim 10\,ID_{\text{cap}}$. 14

3.5 A single microcapillary ($ID = 100$ μm, $OD = 200$ μm) shown next to a human hair for scale. 15

3.6 SolidWorks model of the 3D-printed nozzle assembler. The triangular extrusion mates with the CF flange slot to hold the nozzle at 45ř during capillary loading. 15

3.7 Nozzle assembly setup. The modified CF flange is held at 45ř in the 3D-printed assembler. Tape boundaries surround the work area to recover any dropped capillaries. The glass container at upper right holds the capillaries submerged in methanol prior to placement. 16

3.8 Capillaries clumped together by methanol surface tension. Lifting these clumps and depositing them into the triangular slot allows many capillaries to be placed simultaneously. 16
3.9 **(a)** Nozzle face toward the mixing chamber; **(b)** nozzle face toward the growth substrate. 17
3.10 Stainless steel cylindrical test reservoir wrapped in a custom Nichrome-mica heater 19
3.11 Temperature versus time for the stainless steel test reservoir wrapped with different numbers of Nichrome coil turns 20
3.12 Example zig-zag Nichrome routing pattern used for the nozzle heater. . . 20
3.13 Assembled dual-species beam source labeling all heaters. See Fig. 3.18 for the same image with other beam source components labeled. 21
3.14 Schematic of the Ar gas handling system. A coarse ball valve controls upstream pressure, a pressure gauge ensures the flow controller operates within its specified inlet pressure range of 11.5–160 PSIA [35], and a downstream leak valve and coiled capillary tube provide additional conductance reduction. All fittings are stainless-steel Swagelok. 22
3.15 Helium leak test result for the Ar gas handling system, showing a leak rate at or below the instrument floor of 7.5×10^{-10} Torr L/s. 24
3.16 **Cross-sectional CAD render of the dual-species beam source assembly.** Argon enters through the Ar gas inlet (top, blue arrow) and Rubidium vapor enters from the heated reservoir (bottom, red arrow) through the reservoir valve. Both species mix in the mixing chamber before passing through the microcapillary nozzle (purple arrow). The pneumatic bypass valve allows the system to be pumped down without flowing gas through the capillaries, reducing pump-down time. 25
3.17 **External CAD render of the dual-species beam source assembly.** The exterior view shows the overall geometry of the assembled source, including the optical viewport on the mixing chamber. Component labels are consistent with Fig. 3.16. 26
3.18 **Assembled dual-species beam source.** Component labels correspond to those in the CAD renders of Figs. 3.16 and 3.17. The Ar gas handling hardware visible at left connects to the flow meter and the rest of the gas handling system. Heater foil and wiring are described in Fig. 3.13. 26

4.1 **Schematic diagram of dual-species beam source characterization setup.** 28
4.2 **Image of dual-species beam source characterization chamber.** . . 29
4.3 Image of dual-species beam source characterization chamber and optics . 29
4.4 Simplified optics diagram of probe beam preparation for Rb beam spectroscopy and analysis. 30
4.5 Rb absorption spectrum from collimated Rb beam probed perpendicularly to Rb beam propagation. Due to high collimation Doppler broadening is negligible, allowing one to fully resolve all hyperfine excited state transitions. 31
4.6 Periscope setup to move probe beam up and down along Rb beam and record its spatial profile, ... 32
4.7 Gaussian fit to the 780 nm probe beam intensity profile imaged on a ThorCam DCC1545 camera. 32
4.8 Raw photodetector output showing the $\sim 1\,\mathrm{V}$ DC background with 250 Hz, 4 mV sawtooth modulation from the laser frequency scan. $\sim 0.05\,\%$ fractional absorption signal. 34
4.9 Schematic of the two-stage signal-conditioning circuit. 35
4.10 Photograph of the assembled filter-amplifier circuit. 35
4.11 **Data acquisition and analysis pipeline visualized**. (a) Full sawtooth ramp showing two rising and two falling sweeps used as independent samples. (b) Degree-2 polynomial background fit (green) to subtract from each ramp. (c) Lorentzian fit to the absorption feature after background removal to extract relative absorptions. 36
4.12 Diagram of how divergence is defined using method A. Eq. 4.11 38
4.13 Diagram of how divergence is defined using method B. Eq. 4.13 39

5.1 Zone 1 pure-Rb spatial profile fitted with a Gaussian. The relatively large reduced chi-squared indicates the Gaussian is not an ideal model for the Zone 1 profile; see Sec. 5.4. 44
5.2 Zone 1 pure-Rb spatial profile fitted with a Lorentzian. The Lorentzian provides a substantially better reduced chi-squared at Zone 1. The origin of this improvement and its physical significance are discussed in Sec. 5.4. 45
5.3 Zone 2 pure-Rb spatial profile fitted with a Gaussian. The Gaussian fit quality improves at the farther zone, consistent with the beam profile becoming more Gaussian-like as it propagates (Sec. 5.4). 45

5.4 Zone 2 pure-Rb spatial profile fitted with a Lorentzian. At Zone 2 the gap in fit quality between Lorentzian ($\chi^2_\nu = 1.78$) and Gaussian ($\chi^2_\nu = 2.18$) narrows compared to Zone 1, suggesting the two models may converge as the beam expands. 46
5.5 Rb-Ar dual-species beam spatial profile fitted with a Gaussian. $\chi^2_\nu \approx 5.5$ indicates a poor Gaussian fit to profile, consistent with the same behavior seen in the pure-Rb data. 47
5.6 Rb-Ar dual-species beam spatial profile fitted with a Lorentzian. As with the pure-Rb Zone 1 data, the Lorentzian fit quality is better than Gaussian. 47
5.7 Triangular microcapillary array image superimposed on the Rb-Ar spatial absorption profile (Gaussian fit). The array orientation matches the periscope and probe beam sweep direction. A visible gap between the nozzle clamp and CF flange (bottom) could be consistent with Rb escaping outside the capillary array, potentially explaining the elevated left-side tail. 49

6.1 Example Monte Carlo realization of a dopant configuration. The central test dopant is fixed at the origin, while all other dopants are placed randomly and uniformly in a cubic volume of side L at target density ρ. For each realization, the dipole magnetic field from all neighbors is summed at the origin and converted to a hyperfine transition frequency shift of the central test dopant. 56
6.2 Example histogram $H(\Delta\nu)$ of Monte Carlo frequency shifts. Each bin counts how often a given shift $\Delta\nu$ appears over many random configurations of neighboring dopants. The histogram is fit to a Lorentzian (Eq. (6.16)) to extract an effective inhomogeneous linewidth Γ, which is then mapped to a coherence time $T_2^* = 1/(\pi\Gamma)$. 58
6.3 Monte Carlo simulated T_2^* versus dopant density (blue squares) compared to the Kittel-Abrahams analytic dipolar limit (black line), evaluated for the ^{85}Rb transition $|F = 3, m_F = -1\rangle \to |F = 3, m_F = 0\rangle$ with $g_F = 1/3$. Both curves follow $T_2^* \propto 1/\rho_{\text{dopant}}$ scaling, and agree to within a factor of ~ 2 across five orders of magnitude of density. 60
6.4 Dependence of the simulated T_2^* on the three pumping and alignment efficiency parameters (p_F, p_{m_F}, p_{align}) for ^{85}Rb at fixed density. All other efficiencies are held at 1.0 while each is varied individually. The result is relatively insensitive to all three, with p_{m_F} producing the largest effect at up to a factor of ~ 2. 61

6.5 Simulated versus experimental inhomogeneous broadening for several neighboring m_F transitions within the $F = 3$ ground-state manifold of ^{85}Rb in solid parahydrogen, using values reported in Ref. [11]. 62
6.6 Comparison between experimental inhomogeneous linewidths for ^{85}Rb in solid neon at densities $\rho \sim 10^{16}\,\text{atoms/cm}^3$ [10] and the dipole-dipole-limited values predicted by the Monte Carlo model. At these "low" densities, the simulated broadening is nearly two orders of magnitude smaller than observed. 63
6.7 Dipole-dipole inhomogeneous broadening model for the $|F = 1, m_F = 1\rangle \rightarrow |F = 2, m_F = 2\rangle$ microwave transition of ^{23}Na in solid neon at a dopant density of $\rho \sim 3 \times 10^{16}\,\text{atoms/cm}^3$ [14]. The experimental inhomogeneous linewidth is approximately 980 kHz, whereas the model predicts only about 2.29 kHz, more than two orders of magnitude lower. 64

A.1 Sketch of modified 2.75" CF flange. Cut to fit triangular array of microcapillaries as discussed in Sec. 3.3 71
A.2 Sketch of clamp to pressure fit microcapillary array into modified flange in Fig. A.1. Discussed in Sec. 3.3 72
A.3 Sketch of stainless steel strontium reservoir discussed in Sec. 3.5 72

B.1 Certificate of Analysis of rubidium used and discussed in this thesis [30] . 73
B.2 Rubidium vapor pressure curve [25] 74

C.1 Pure Rb beam spatial absorption profile at Zone 1 (2.46" from nozzle). Each panel shows the photodetector signal with a Lorentzian fit at a given probe height y. 76
C.2 Unattenuated absorption signal at Zone 1 (probe position 450, bypassing amplifier), used to determine absolute absorption fraction for flux rescaling. 76
C.3 Pure Rb beam spatial absorption profile at Zone 2 (12.3" from nozzle). Each panel shows the photodetector signal with a Lorentzian fit at a given probe height y. 77
C.4 Unattenuated absorption signal at Zone 2 (probe position 500, bypassing amplifier), used to determine absolute absorption fraction for flux rescaling. 78
C.5 Mixed Rb-Ar beam spatial absorption profile at Zone 1 (2.46" from nozzle). Each panel shows the photodetector signal with a Lorentzian fit at a given probe height y. 79

C.6 Unattenuated absorption signal for the Rb-Ar beam (probe position 450, bypassing amplifier), used to determine absolute absorption fraction for flux rescaling. 80
C.7 Overlay of all Rb beam spatial absorption profiles and divergence fits across all measurement runs and zones. Gaussian and Lorentzian fits are shown for direct comparison. 80

List of Tables

2.1 Comparison of leading eEDM experiments. and doped crystals in terms of coherence time and N. 4

5.1 Beam Characterization Summary 51

Acknowledgments

I have deeply enjoyed my time at Northwestern and getting to know and work with Brian Odom since my freshman year. I feel I have grown an amount I never *knew* was possible thanks to both his guidance and the independence and trust he has given me. I am also very thankful to have been able to share our love for ice cream and introduce the best ice cream of all time to him: Graeter's!

I would also like to thank Tim Kovachy for allowing me to work in his lab in order to gain the training required to build this beam source in Brian Odom's lab, and for planning this from the start with Brian. I also want to thank Tim for always being open to any questions and discussions — from this thesis itself, to rotating black holes when working on a class project. He has been a massive support throughout my undergrad career.

I am also incredibly grateful for all the support I have gotten from Sharika Saraf. She was the first person I interacted with consistently when beginning work in Tim's lab and taught me many of the most foundational and important skills I have used in research, from vacuum cleaning and assembly, CAD design, heater and electronic design, and general lab techniques.

Xing Fan was also a great support during the design of my characterization chamber. And importantly, he was was big reason I began believing in my abilities more and continued motivating me to work hard.

I have also greatly enjoyed recently beginning to mentor others, getting to work with Haley Randall and Brandon Lofton. I can tell they are both very interested in and devoted to research and the goals of our projects, and I always enjoy answering (or at least attempting to answer) their questions. I look forward to seeing what they'll accomplish. Please take care of yourselves though — there is much more to life than physics and research (it took me a lil too long to realize that)! I am also incredibly thankful for getting to know and spend time with the other undergraduate who has been in the lab alongside me for longer, Joel Adhiambo. Joel I have greatly enjoyed getting to know you and our fun conversations when working on whatever.

Outside of physics, I would not be who I am without all my friends, but especially not without Boomshaka! Boomshaka has allowed me to continue expressing myself and continue my music and drumming career. I have grown so much both as a musician and a person thanks to everyone in it. It has always been an important escape and a much-needed break from all the physics and schoolwork.

Throughout most of my time at Northwestern, I have been lucky enough to live in the same city as my sister Kirby. She has always been one of the few constants in my life and someone I have always been able to go to for support. I am truly thankful for all the love, jokes, and time we have gotten to spend together these past years.

The person who originally got me interested in science and eventually physics was my grandfather, Jerome Collins. In a family of primarily creatives, he was the only scientist. We would always talk about my math and science classes and he was always so excited to hear about anything I was up to. I wish I could talk to you about all the research and work I have accomplished, but I know you'd be proud. I also need to thank him for somehow making the most amazing PB&J sandwiches known to man — I still don't know how he made them so well.

I wouldn't be here without both my Mom and Dad (both literally and figuratively). The support you have given me throughout my life to always chase my dreams and believe in myself has paid off. Thank you both as well for the enormous financial support you have provided, which allowed me to focus my time on my studies rather than finances — I am truly lucky. Thank you, Dad, for always letting me experiment in the backyard, even when the neighbors started asking about the loud bangs when I tried to make a rocket. The constant room you've given me to explore my life and interests has meant so much.

I would also like to take a moment to thank Northwestern Undergraduate Research for helping fund me over the summer. I must also acknowledge that the study resulting in this thesis was assisted by a grant from the Undergraduate Research Grant Program, administered by Northwestern University's Office of Undergraduate Research. However, the conclusions, opinions, and other statements in this publication are the author's and not necessarily those of the sponsoring institution.

Finally, throughout my time in Brian's lab, I have had the incredible mentorship and friendship of Daniel Lutes. I will always appreciate everything he has taught me and his seemingly endless depth of knowledge. I also would not be where I am without the countless times he has helped look over and improve grants, grad school applications, and even this thesis — sometimes at the very last minute — to get them in the best shape possible (given the limited time that my procrastination sometimes left him). I truly do not think I would be the researcher and person I am today without Daniel's help and

constant support, and for that I am deeply thankful.

Chapter 1

Introduction and Overview

Through this thesis I outline the primary work I have carried out in the Odom Lab at Northwestern University toward growing and studying doped cryogenic noble gas crystals for precision measurement. My primary project has been the development of a novel, tunable dual-species Rubidium-Argon beam source to control the growth of these doped crystals and allow for systematic studies between growth parameters and crystal quality and coherence times. The beam source uses an array of microcapillaries to collimate and deliver a mixed Rb-Ar beam to a cryogenic growth substrate, with independent control over both Rb and Ar flux to scan a wide range of both dopant densities and crystal growth rates. A secondary project is also reported on the development of a Monte Carlo simulation of dipole-dipole interaction induced inhomogeneous broadening between dopants, developed to better understand possible sources of decoherence in these crystals.

Chapter 2 provides brief background on doped cryogenic crystals, covering their major promises and current limitations. Chapters 3, 4, and 5 cover the design, characterization methods, and current characterization results of my Rb-Ar beam source in detail. Finally, Chapter 6 presents the Monte Carlo simulation, discusses its results, and considers its implications for doped crystal growth.

Chapter 2

Background: Doped Cryogenic Noble Gas Crystals

Doped inert cryogenic crystals offer a promising platform for fundamental physics research, including high-precision measurements and searches for physics beyond the Standard Model. By embedding atoms or molecules (dopants) inside an inert cryogenic crystal, one creates what amounts to an "artificial vacuum" (Fig. 2.1). The crystal serves as a chemically inert host lattice that isolates the dopants, holding them in place for arbitrarily long interrogation times [1, 2]. This pristine environment enables precise measurements of quantum properties such as the electron electric dipole moment (eEDM)–one of the most sensitive probes for new physics that could explain the matter-antimatter asymmetry of the universe–as well as potential applications in dark matter searches and quantum information science [2, 3].

When grown with sufficient quality these crystals are optically transparent, enabling standard atomic, molecular, and optical (AMO) techniques for state preparation and readout of the embedded dopants. Although the crystal lattice does perturb dopant properties (optical absorption and fluorescence lines are broadened and red-shifted by tens to hundreds of nanometers relative to their gas-phase values) excited-state lifetimes remain comparable to free-space values [4, 5], and optical pumping of electron spin states has been demonstrated with varying degrees of efficiency [6].

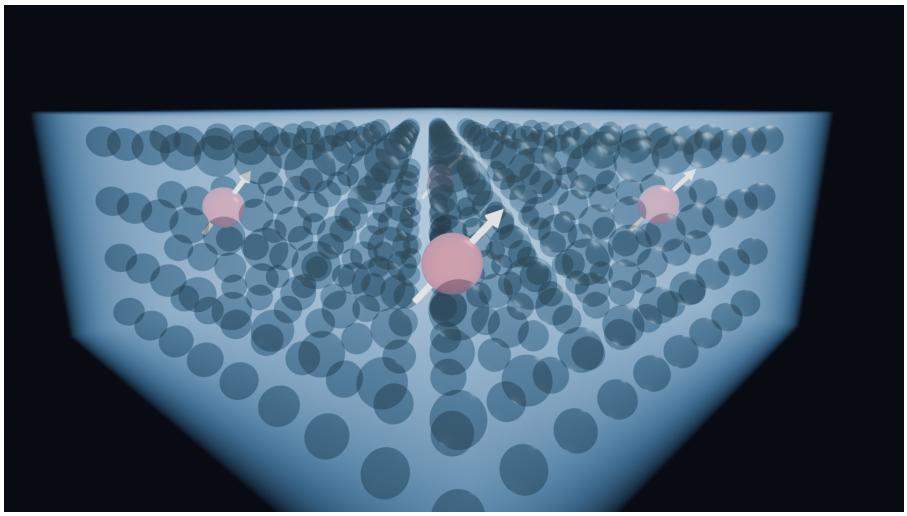


Figure 2.1: Artistic rendition of an alkali-doped rare-gas crystal. The blue array represents the host rare-gas lattice, while the red spheres with arrows represent embedded dopant atoms and their spin.

2.1 Promise of the Platform: High Density and Statistical Power

The central attraction of doped cryogenic crystals for precision measurement is their ability to simultaneously interrogate an enormous number of dopant atoms or molecules. This matters because the statistical sensitivity of spin-precession measurement, such as an eEDM measurement, scales as

$$\sigma_{\mathrm{EDM}} \propto \frac{1}{T_2^* \sqrt{N}}, \tag{2.1}$$

where T_2^* is the ensemble coherence time and N is the total number of interrogated spins. A crystal capable of holding $N \sim 10^{16}$ dopants/cm^3 (very reasonable for this platform) could give an enormous gain in statistical sensitivity compared to other platforms.

As a concrete benchmark, consider one of the most competitive eEDM measurements ACME-II. ACME-II spent approximately 350 hours collecting data in a beam of a few hundred thousand molecules per second, yielding $N \sim 10^{12}$ total molecules interrogated [7]. A mm scale doped cryogenic crystal with $\rho \sim 10^{16}$ dopants/cm^3 and $T_2^* \sim 1$ ms could, in principle, achieve the same statistical uncertainty as ACME-II in seconds rather than weeks–assuming one dopes with molecules that have similar eEDM enhancement factors to ACME-II's. Table 2.1) compares leading eEDM experiments coherence and interrogated spins to current doped crystals.

Table 2.1: Comparison of leading eEDM experiments. and doped crystals in terms of coherence time and N.

Platform	T_2	T_2^*	N	Note
ACME-II beam [7]		2–3 ms	$\sim 10^{12}$	$\sim$ 350 hours data collection
JILA Ion trap [8]		3 s	$\sim 10^{8}$	$\sim$ 620 hours data collection
Cs in He crystal [9]		0.1 s	$\sim 10^{9}/\text{cm}^3$	High T_2^*, but low density
Rb in Ne crystal [10]	0.1 s	10 μs	$\sim 10^{16}/\text{cm}^3$	High density, poor T_2^*

Table 2.1 makes clear the platform's promise and current short falling. In terms of N doped crystals easily surpass the top platforms, especially when you remember that these crystals can continuously measure the same dopants over and over. That is while beams and ion traps continuously load and probe new molecules over hundreds of hours to reach their reported N, doped crystals can already have a higher number of dopants immediately available, and these same dopants can be probed over and over again. However, the current T_2^* in these high-density crystals are so short that the advantage from N is lost. An important note that will be brought up shortly though, is that the homogeneous relaxation time T_2 remains high. These short T_2^* times are the central problem the Odom lab is working to resolve.

2.2 Coherence in Doped Crystals

To understand why T_2^* is so short in existing high-density crystals, and, why there is good reason to believe it can be dramatically improved, it is necessary to distinguish between three coherence timescales that all appear in these systems: T_1, T_2, and T_2^*.

T_1 is the longitudinal relaxation time and sets how quickly the spin population difference relaxes back to thermal equilibrium. Physically, T_1 is governed by spin-lattice relaxation and interactions between dopants and phonons in the host crystal. It is the longest of the three coherence time in these systems, often reaching hundreds of milliseconds to seconds [10].

T_2 is the homogeneous transverse relaxation time. It characterizes the decay of the transverse spin components and the loss of spin phase, arising from processes that are local and irreversible. The exact mechanism limiting T_2 in these crystals does not seem to have a clear explanation I can find. Experimentally, T_2 is extracted from a Hahn echo measurement, which refocuses the dephasing from static frequency inhomogeneities and isolates the true homogeneous decay. Rb-doped crystals can commonly get $T_2 \sim 0.1$ s [10, 11].

T_2^* is the *ensemble* transverse relaxation time, and it is what limits sensitivity in a Ramsey-type measurements, like those used for an eEDM experiment and many other quantum sensing platforms. In a real experiment we never probe a single dopant but an ensemble of N dopants that each experience slightly different local environments within the crystal. These local variations shift each dopant's resonant frequency by a slightly different amount. Even if every individual spin has a long homogeneous T_2, the ensemble-averaged transverse magnetization dephases rapidly as the spins accumulate differential phase offsets. This ensemble dephasing time, T_2^*, is related to T_2 by

$$\frac{1}{T_2^*} \approx \frac{1}{T_2} + \frac{1}{T_2^{\text{inhom}}}, \tag{2.2}$$

where T_2^{inhom} is an effective timescale set by the width of the static frequency distribution across the ensemble [12]. In most doped crystals to date, $T_2^{\text{inhom}} \ll T_2$, so T_2^* is entirely dominated by inhomogeneous broadening rather than by the true homogeneous T_2 [3, 10, 11, 13].

For Rb in solid neon, Dargyte et al. report $T_2 \approx 0.1$ s but $T_2^* \approx 10$ μs at dopant densities around $\rho \sim 10^{16}$ atoms/cm^3 [10]. Similarly, for Rb in solid parahydrogen, Upadhyay et al. find $T_2 \approx 0.1$ s but $T_2^* \sim 100$ μs at comparable densities [11]. The crystal platform thus already supports millisecond-scale homogeneous coherence. The question is why the ensemble coherence is 10^3-10^4 times shorter.

2.2.1 What Limits T_2^*

One crucial question in the doped cryogenic rare-gas crystal community is what primarily limits the ensemble coherence time T_2^*. The primary consensus seems to suggest that short T_2^* can largely be attributed to electrostatic interactions with the host matrix and static inhomogeneity in the crystal structure (i.e. strain, defects, and multiple trapping sites) [11]. There is some belief that dipole-dipole interactions between dopants may also contribute significantly [14]. I address this debate in Chapter 6, where a Monte Carlo simulation of dipole-dipole-limited T_2^* is developed for range of species, densities, and transitions and shows that dipole-dipole interactions are too small to account for most observed decoherence at typical growth densities–further supporting structural disorder as the dominant mechanism. However, at certain "higher" densities (described in Sec. 6.4.2), simulated dipole-dipole interactions approach or match T_2^* within an order of magnitude, suggesting some of the disagreement may come from these different density regimes.

However, with structural disorder as the dominant mechanism at densities we plan to

grow at, improving crystal quality or growing more uniform, single-crystal samples with fewer trapping sites and less strain, should be able to push T_2^* significantly closer to T_2 or more likely to the dipole-dipole-limited T_2^*. With the observed $T_2 \sim 0.1$ s there is clearly much room to improve T_2^* in these crystals.

2.3 Odom Lab's Goal: Improved Crystal Quality → Improved Coherence Time

In order to address electrostatic inhomogeneities from grain boundaries, single crystals will be grown prior to growing doped layers on top. This is done by first growing a crystal out of a liquid phase, which is known as the Bridgman–Stockbarger technique, and has been demonstrated for noble gases like Argon [15]. The Odom lab has developed these techniques in parallel with the dual-species beam source so that they can be combined to study effects on coherence time. Rather than using separate sources for the dopant and the noble gas, a single co-deposition nozzle combines both species, making the growth rate and dopant density more straightforward to control simultaneously [16]. A key research goal of the Odom lab is to systematically explore the optimal conditions for growing these crystals — factors such as dopant density and growth rate both affect crystal quality and the resulting T_2^* coherence time — so the beam source is designed to cover a wide range of growth conditions. We also plan to perform X-ray diffraction analysis at Argonne National Laboratory to directly assess crystal quality. The design of the beam source that enables this is described in Chapter 3.

Chapter 3

Beam Source

3.1 Crystal Growth Chamber and Design Constraints

The Bridgman–Stockbarger geometry imposes strict constraints on the beam source design. The chamber must fit inside an X-ray diffractometer at Argonne National Laboratory—where we plan to perform diffraction analysis to assess crystal quality—and must satisfy UHV requirements for the inner growth chamber. Together these impose tight size constraints: the beam must travel roughly half a meter through a tube of $\sim 1\,\mathrm{cm}$ inner diameter, with this distance also serving to reduce heat loads from the hot oven on the cryocooler.

Rather than using separate sources for the dopant and the noble gas, it proved simpler to combine them into a single co-deposition nozzle. This choice also offers advantages for doped-crystal growth, as it makes the growth rate and dopant density more straightforward to control simultaneously [16].

A key research goal of the Odom lab is to systematically explore the optimal conditions for growing these crystals. Factors such as dopant density and growth rate both affect crystal quality and the resulting T_2^* coherence time, so we wish to cover a wide range of growth conditions. Growth rates in these crystals typically fall in the range ~ 10–100 μm/hr [10, 16], with dopant densities commonly near 10^{16} dopants/cm^3. The Odom group also aims to access much slower growth rates (~ 1 μm/hr) and lower dopant densities, possibly down to 10^{14} dopants/cm^3.

In this chapter I describe the design choices I made to realize a tunable dual-species Rb-Ar beam source for doped cryogenic crystal growth.

3.2 Design Overview

With a target dopant density of 10^{16} dopants/cm^3, the ratio of Ar atoms to Rb atoms inside the oven is roughly $N_{Ar}/N_{Rb} \sim 10^6$. Since $N_{Ar} \gg N_{Rb}$, the conductance and flow properties of the nozzle are governed almost entirely by the much more abundant Ar, and the Rb atoms are carried through under essentially the same flow conditions. I therefore design the nozzle first to achieve the required Ar flow rate and beam collimation, then set the Rb partial pressure independently to reach the target dopant density.

Ar is supplied and regulated through a mass-flow controller, while Rb is supplied by a heated reservoir and variable-conductance leak valve. Both species are mixed in a common mixing chamber before passing through a collimating microcapillary nozzle array toward the growth substrate. A block diagram of the beam source layout is shown in Fig. 3.1.

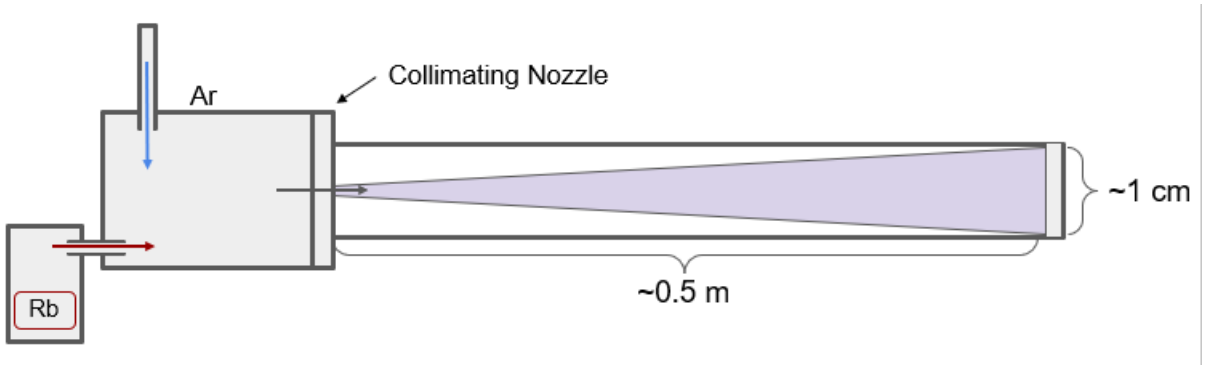


Figure 3.1: Schematic cross-section of the dual-species beam source. Ar is admitted through a mass-flow controller and mixed with Rb vapor from the heated reservoir before both species pass through the microcapillary nozzle array and travel $\sim 0.5\,\mathrm{m}$ to the cryogenic growth substrate.

The remainder of this chapter describes each subsystem in turn: the nozzle design and the flow physics that govern it (Sec. 3.3), the Rb dopant source (Sec. 3.4), beam-source heaters (Sec. 3.5) the Ar gas handling system (Sec. 3.6), and finally the physical assembly of the complete beam source (Sec. 3.7).

3.3 Nozzle Design: Microcapillary Array

To achieve the relatively large Ar fluxes needed for the target growth rates while maintaining tight beam collimation, I use an array of microcapillaries following the design of Senaratne et al. [17]. A triangular groove is machined into a CF flange normal to its surface and an array of microcapillaries is packed into it. A close-fitting clamp is pressed

down onto the array and secured with screws, clamping the capillaries in place. Wire EDM is used to machine both the triangular groove and the clamp contact surfaces to the precision required to keep all capillaries mutually parallel and normal to the nozzle face, ensuring a well-collimated beam. The original design from Senaratne et al. is shown in Fig. 3.2.

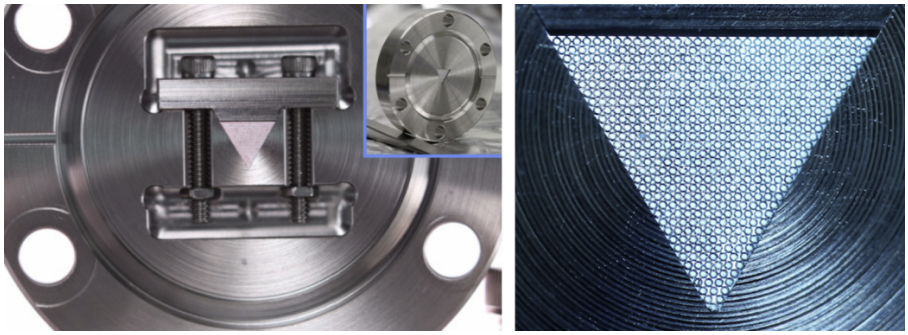


Figure 3.2: Microcapillary array nozzle from Senaratne et al. [17], showing the triangular capillary bundle clamped into a CF flange.

3.3.1 Flow Regime and Beam Divergence

The flow regime of the gas through the capillaries is characterized by the Knudsen number

$$Kn = \frac{\lambda}{L_{\text{char}}}, \tag{3.1}$$

where λ is the mean free path and L_{char} is the relevant characteristic length [18]. The mean free path is

$$\lambda = \frac{k_B T}{\sqrt{2}\,\pi\sigma^2 P}, \tag{3.2}$$

where P is the pressure and σ is the collision cross-section [19]. Since $N_{Ar} \gg N_{Rb}$, both are species dominated by Ar interactions, and the flow regime of both species is set by the Ar partial pressure and cross-section.

When evaluating Eq. 3.1 for flow through a capillary, the relevant length scales are the inner diameter ID_{cap} and the tube length L_{cap}, which define two Knudsen regimes. The fully molecular regime ($\lambda \gg L_{\text{cap}}$, $Kn(L) \gg 1$) applies when particles are expected to traverse the entire tube without colliding. The intermediate regime ($ID_{\text{cap}} \lesssim \lambda \lesssim L_{\text{cap}}$) describes the case where molecules collide within the tube but the mean free path exceeds the tube diameter. Fully viscous flow ($\lambda \ll ID_{\text{cap}}$) applies when the mean free path is much smaller than the tube diameter. We never plan to operate in the fully viscous regime.

In the molecular-flow regime, the half-angle divergence of gas leaving a single tube of inner diameter ID and length L is estimated from the geometric aspect ratio,

$$\theta_{1/2} = \arctan\left(\frac{ID}{L}\right). \tag{3.3}$$

Senaratne et al. report that even in the intermediate regime ($ID_{\text{cap}} \lesssim \lambda \lesssim L_{\text{cap}}$) the divergence remains as same as is expected for $\lambda \gg L_{\text{cap}}$ regime, attributing this to the gas density decreasing along the capillary so that the local mean free path grows enough to restore molecular-flow-like behavior before the gas exits [17]. An alternative expression for capillary divergence appears in the literature [20],

$$\theta_{1/2} \approx 1.68 \times \frac{ID}{L}, \tag{3.4}$$

which gives a somewhat larger estimate for the same geometry. The physical interpretation of and relationship between these two expressions is not entirely clear to me, and I did not fully appreciate the distinction when originally designing the nozzle. The characterization measurements in Chapter 5 will help determine which better describes the realized beam. It is also not fully clear how single-tube divergence scales to a full multi-capillary array, and I hope to explore this further in future work.

3.3.2 Crystal Growth Rate and Conductance

Following Senaratne et al. [17], I use the molecular-flow conductance formula to estimate the nozzle throughput. The following equations primarily follow from [19]. For a single tube of length L and inner diameter D in the molecular regime,

$$C_{\text{mol}} = \frac{\pi}{12}\,\overline{v}\,\frac{D^3}{L}, \tag{3.5}$$

where $\overline{v}$ is the mean thermal speed from the Maxwell-Boltzmann distribution,

$$\overline{v} = \left(\frac{8k_BT}{\pi m}\right)^{1/2}, \tag{3.6}$$

with k_B the Boltzmann constant and m the particle mass. For an array of N_{cap} identical capillaries, the total nozzle conductance is

$$C_{\text{Nozzle}} = N_{\text{cap}} \cdot C_{\text{cap}}. \tag{3.7}$$

The gaps between capillaries in the array are assumed to contribute negligible relative to the actual conductance through the capillaries, or that it will be small enough (within order of magnitude) so that it is easy to correct for later.

The throughput—the rate at which gas leaves the oven—at oven pressure P_{oven} is

$$Q = (P_{\text{oven}} - P_{\text{growth chamber}})\, C_{\text{Nozzle}} \approx P_{\text{oven}}\, C_{\text{Nozzle}}, \tag{3.8}$$

since $P_{\text{oven}} \gg P_{\text{growth chamber}}$. Converting to a mass flow rate,

$$\dot{m}_{Ar} = \frac{Q\, M_{Ar}}{R\, T_{\text{Nozzle}}}, \tag{3.9}$$

where M_{Ar} is the molar mass of argon and R is the ideal gas constant. Assuming the Ar beam is distributed uniformly over a circular growth substrate of radius r_{gs} with 100%capture efficiency, and using the solid argon density ρ_{Ar} [21], the linear growth rate is

$$\dot{h} = \frac{\dot{m}_{Ar}}{\rho_{Ar}\, \pi r_{gs}^2}. \tag{3.10}$$

A more accurate treatment would account for the finite beam width and imperfect capture efficiency, but these to first order just add a pre-factor.

3.3.3 Dopant Density

Since $P_{Ar} \gg P_{Rb}$, the nozzle is designed first to satisfy the Ar-flow and growth-rate requirements, with the Rb partial pressure set independently to achieve the desired dopant density. Using the ideal gas law (valid at the low pressures and high temperatures expected inside the oven), the ratio of Rb to Ar atoms is

$$\frac{N_{Rb}}{N_{Ar}} = \frac{P_{Rb}}{P_{Ar}}. \tag{3.11}$$

Assuming this ratio is preserved through the nozzle and at the growth substrate, the dopant density is set by the number density of Ar atoms in the solid crystal,

$$n_{Ar}^{\text{crystal}} = \frac{\rho_{Ar}\, N_A}{M_{Ar}} \approx 2.67 \times 10^{22}\ \text{cm}^{-3}, \tag{3.12}$$

where N_A is Avogadro's number, giving

$$\rho_{\text{dopant}} = \frac{P_{Rb}}{P_{Ar}}\, n_{Ar}^{\text{crystal}}. \tag{3.13}$$

Here P_{Ar} is set by the Ar flow rate once the oven reaches steady state, and P_{Rb} is controlled via the Rb reservoir and valve as described in Sec. 3.4.

3.3.4 Nozzle Parameters and Array Geometry

I use the same microcapillary stock as Senaratne et al., sourced from MicroGroup [17, 22], modifying only the length to set the desired aspect ratio and beam divergence.

The beam must travel $\sim 0.5\,\mathrm{m}$ through a $\sim 1\,\mathrm{cm}$-ID tube to the growth substrate. Treating the nozzle as a point source gives a geometric half-angle constraint of $\theta_{1/2} \lesssim 0.7°$. This approximation is not strictly valid since the nozzle has finite extent (discussed further in Chapter 5), but it provides a useful bound for the initial design. Including margin for machining tolerances and for possible angular misalignment of connecting flanges, I selected capillaries of $ID = 100\ \mu\mathrm{m}$ (0.004 in [22]) cut to a length of 7.62 mm, giving

$$\theta_{1/2} = \arctan\left(\frac{100\ \mu\mathrm{m}}{7.62\ \mathrm{mm}}\right) \approx 0.75°. \tag{3.14}$$

Note on design equation: The geometric estimate of Eq. 3.14 was used during the initial nozzle design, as it reproduces the divergences reported by Senaratne et al. for their microcapillary array [17]. The expression of Eq. 3.15 was not applied at design time, but is included here for completeness:

$$\theta_{1/2} = 1.68 \times \frac{100\,\mu\mathrm{m}}{7.62\,\mathrm{mm}} \approx 1.26°. \tag{3.15}$$

The multiple measured divergence results of Chapter 5 can be consistent with both estimates depending on method used, and the discrepancy between them is addressed there.

The capillaries are stacked in an equilateral-triangle array: each successive row (from the apex) contains one additional capillary, so the total count for N_{rows} rows is

$$N_{\mathrm{cap}} = \frac{N_{\mathrm{rows}}(N_{\mathrm{rows}} + 1)}{2}, \tag{3.16}$$

and the triangle side length is

$$S = OD_{\mathrm{cap}} \times N_{\mathrm{rows}}, \tag{3.17}$$

where $OD_{\mathrm{cap}} \approx 200\ \mu\mathrm{m}$ (0.008 in [22]) is the capillary outer diameter. Balancing growth-rate requirements against assembly complexity, I chose $N_{\mathrm{rows}} = 21$, giving $N_{\mathrm{cap}} = 231$

capillaries and $S \approx 4.2\,\text{mm}$. A more systematic optimization of the geometry would be worthwhile in future iterations of the design.

Plugging these values into Eqs. 3.5–3.10 produces the growth-rate heat maps of Figs. 3.3 and 3.4. The overlaid contour lines show where $\lambda_{Ar} = ID_{\text{cap}}$ (solid) and $\lambda_{Ar} = 10\,ID_{\text{cap}}$ (dashed), marking the approximate boundaries of the molecular-flow regime. Enforcing $\lambda_{Ar} \gtrsim ID_{\text{cap}}$ allows growth rates up to $\sim$150 μm/hr, while the more conservative $\lambda_{Ar} \gtrsim 10\,ID_{\text{cap}}$ limit restricts the accessible range to $\lesssim$ 15 μm/hr. Current characterization results (Ch. 5) are consistent with operating under the $\lambda_{Ar} \gtrsim 10\,ID_{\text{cap}}$ condition, though further measurements are needed to establish the exact boundary. Throughout this analysis I apply the molecular conductance formula, Eq. 3.5, even in the intermediate regime $L_{\text{cap}} > \lambda_{Ar} > ID_{\text{cap}}$, following Senaratne et al. [17]; the accuracy of this approximation near the $\lambda_{Ar} \sim ID_{\text{cap}}$ boundary remains an open question for future characterization.

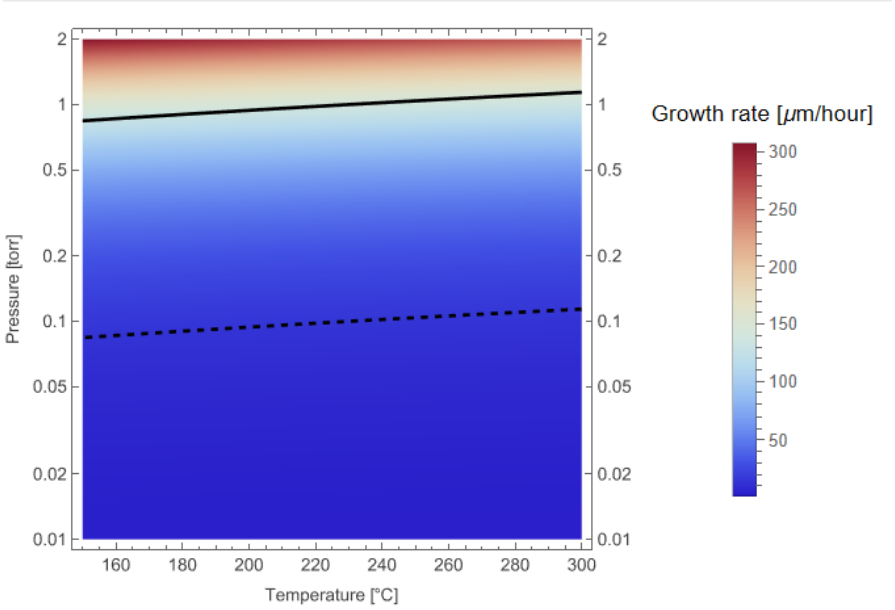


Figure 3.3: Estimated growth rate as a function of oven pressure and temperature for the $N_{\text{rows}} = 21$ nozzle. The solid black line marks $\lambda_{Ar} = ID_{\text{cap}}$ and the dashed black line marks $\lambda_{Ar} = 10\,ID_{\text{cap}}$; the desired operating regime lies below one of these boundaries, but it is currently unclear which. Chapter 5 argues we are currently able to operate to at least $\lambda_{Ar} = 20\,ID_{\text{cap}}$ (Eq. 5.3)

3.3.5 CAD Design and Machining

With the array geometry established, I adapted the Senaratne et al. design to fit our specifications. For $N_{\text{rows}} = 21$ rows with $OD_{\text{cap}} = 0.008\,\text{in}$, the nominal side length is

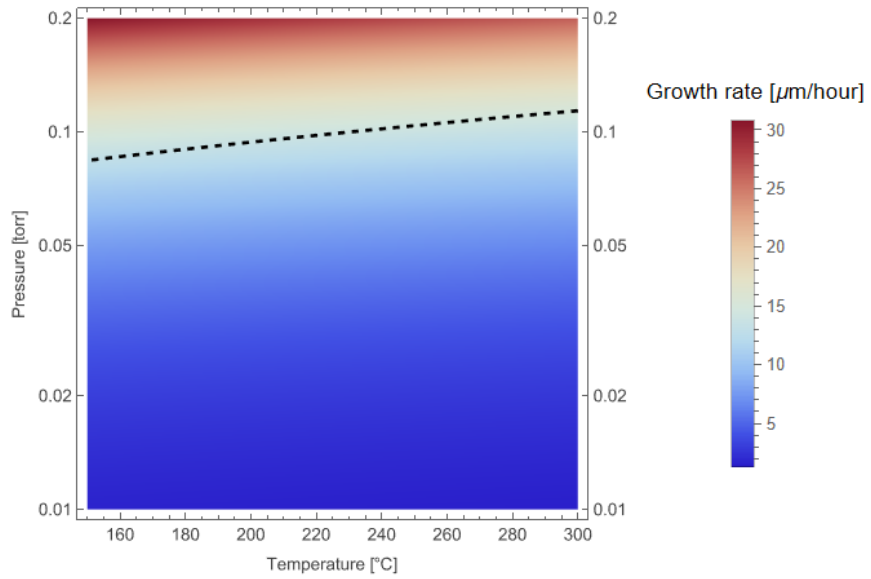


Figure 3.4: Same as Fig. 3.3 but with the color scale zoomed to the lower growth-rate regime accessible when enforcing $\lambda_{Ar} \gtrsim 10\, ID_{\mathrm{cap}}$.

$S = 0.168\,\mathrm{in}$; We got the triangle slot and clamp machined such that $S = 0.175\,\mathrm{in}$ to accommodate slight imperfections in capillary contact and machining tolerances. The triangle was centered on the flange such that its inscribed circle is concentric with the center of the CF flange, ensuring beam collimation along the chamber axis.

The nozzle consists of two machined parts. The first is a modified 2.75 in double-sided CF flange [23] into which the triangular capillary slot, clamp grooves, and screw holes are machined. The triangular slot requires high dimensional accuracy so that all capillaries sit parallel and normal to the flange face. Therefore, wire EDM was used for this feature, following Senaratne et al. [17]. The second part is a separate clamp whose contact edges are also wire-EDM cut to match the slot geometry. Wire EDM was additionally used to cut the 5 ft stock capillary tubing to the desired 0.3 in length. A dedicated fixture allowed multiple capillaries to be cut simultaneously. All parts were fabricated by the Northwestern Research Machine Shop [24].

3.3.6 Microcapillary Assembly and Loading

Assembling the nozzle requires placing all 231 microcapillaries—each roughly the diameter of a human hair—into the small triangular slot (Fig. 3.5).

To simplify this process I designed and 3D-printed a “nozzle assembler” using a resin LCD printer (Fig. 3.6). The assembler was designed to align precisely with the modified CF flange, with a small triangular extrusion that aligns to the slot and sets the correct

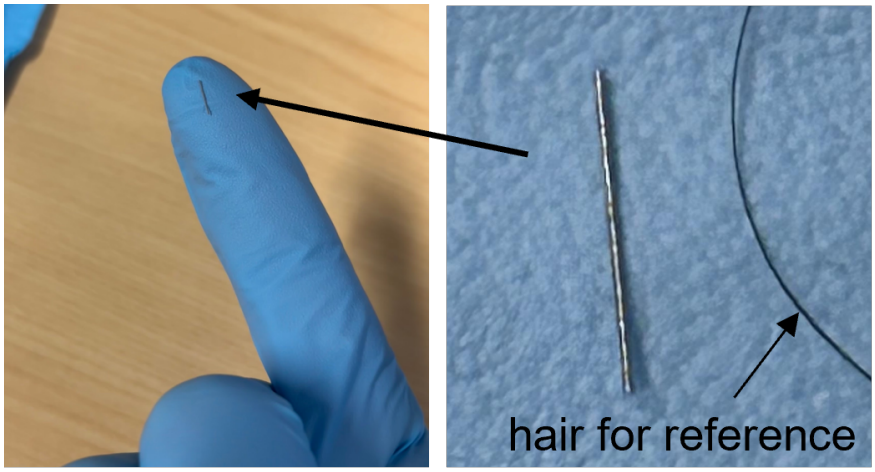


Figure 3.5: A single microcapillary (ID = 100 μm, OD = 200 μm) shown next to a human hair for scale.

capillary height to be flush with the face of the flange. The assembler also holds the nozzle at 45ř from horizontal so that capillaries should rest against the lower walls of the triangle under gravity.

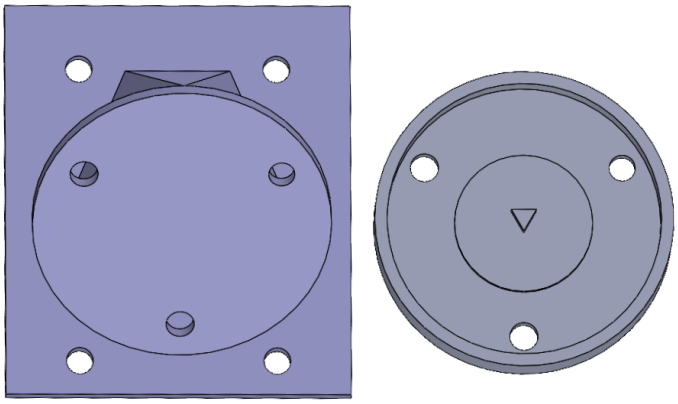


Figure 3.6: SolidWorks model of the 3D-printed nozzle assembler. The triangular extrusion mates with the CF flange slot to hold the nozzle at 45ř during capillary loading.

To prepare the assembly of the nozzle, the loading area is first cleaned with methanol and a tape barriers is made to hopefully contain any dropped capillaries. The 3D-printed parts are cleaned with isopropyl alcohol in a sonic bath and cured under UV light to ensure no liquid resin remains as is standard. The capillaries are cleaned and stored in methanol until placement. The methanol surface tension also causes the capillaries to

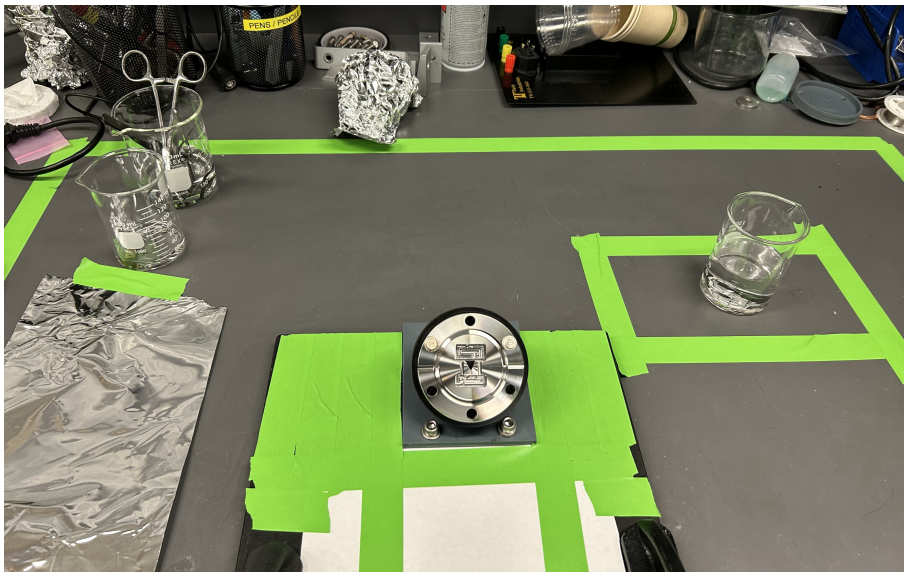


Figure 3.7: Nozzle assembly setup. The modified CF flange is held at 45ř in the 3D-printed assembler. Tape boundaries surround the work area to recover any dropped capillaries. The glass container at upper right holds the capillaries submerged in methanol prior to placement.

clump together, which turns out to be advantageous as large clumps of capillaries can be picked up and deposited into the triangle as a group, where they tend to self-arrange into the correct positions. Using this technique, loading all 231 capillaries took roughly two hours (Fig. 3.7).



Figure 3.8: Capillaries clumped together by methanol surface tension. Lifting these clumps and depositing them into the triangular slot allows many capillaries to be placed simultaneously.

After confirming that 21 rows were present and correctly seated, the clamp was slid

onto the flange and the screws and nuts were tightened just past hand-tight. Care must be taken when seating the clamp to avoid displacing capillaries as misalignment at this step can push capillaries out of position and require the entire array to be reloaded (speaking from experience). The completed nozzle, with both faces visible, is shown in Fig. 3.9.

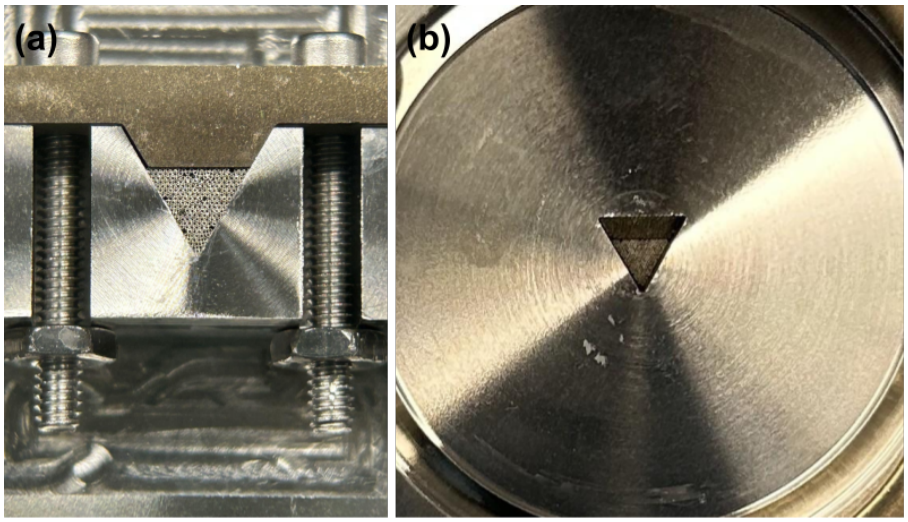


Figure 3.9: **(a)** Nozzle face toward the mixing chamber; **(b)** nozzle face toward the growth substrate.

3.4 Rubidium Dopant Source

3.4.1 Rb Reservoir and Vapor Pressure Control

To understand why a separate heated Rb reservoir with a variable-conductance valve is necessary, consider a one likely operating point: a growth rate of 10 μm/hr at a dopant density of 10^{16} dopants/cm^3.

At a nozzle temperature of $T_{\text{nozzle}} = 200$řC (a temperature we expect to operate at), this growth rate corresponds to $P_{Ar} \approx 0.07$ Torr (From equations of Sec. 3.3.2). Equation 3.13 then requires $P_{Rb} \approx 2 \times 10^{-8}$ Torr. The Rb vapor pressure is given by

$$P_{Rb,\text{res}} = 10^{(A+B/T)} \times 760 \text{ [Torr]}, \tag{3.18}$$

where $A = 4.312$ and $B = -4040$ or $A = 4.857$ and $B = -4215$ when Rb is in liquid or solid phase respectively (Rb melting point is 39.3°C) [25, 26], with T is Rb temperature in kelvin. A helpful Rb vapor pressure curve is also shown in Appendix B. Achieving $P_{Rb} \approx 2 \times 10^{-8}$ Torr only from temperature control would require cooling the Rb to

$T \approx 0°\text{C}$. The situation worsens for lower target dopant densities. Direct temperature-based control of P_{Rb} is therefore impractical.

Instead, the reservoir is heated to produce a high, stable vapor pressure, and a variable-conductance leak valve is used to control the equilibrium Rb partial pressure in the mixing chamber, giving

$$P_{\text{Rb}} = P_{Rb,\text{res}} \frac{C_V}{C_V + C_N}, \tag{3.19}$$

where C_V is the valve conductance and C_N is the nozzle conductance. Adjusting reservoir temperature T_{res} and the valve opening allows P_{Rb}—and therefore ρ_{dopant}—to be set independently of the Ar growth rate. In practice I use a MDC variable leak valve [27] that can be finely adjusted. Separating the reservoir temperature from the nozzle temperature also helps prevent Rb from condensing in and clogging the capillaries [17].

The reservoir itself is a flexible bellows [28], which allows a sealed glass Rb ampoule to be placed inside and pumped down before being broken open under vacuum. This procedure avoids the contamination and safety hazards common when handling alkali metals in air.

3.4.2 Rb Loading Procedure

We used Sigma-Aldrich 99.6% pure Rb with trace metal basis [29, 30]. The certification of the specific Rb sample used in this work is in Appendix B.

Loading Rb into the bellows reservoir requires care to handle a reactive alkali metal safely. The procedure is carried out inside a nitrogen-purged glovebox. All tools and vacuum components are cleaned beforehand and baked when possible to remove surface water. The Rb ampoule is placed into the bellows without breaking it; the leak valve and a blank flange are then used to seal the bellows while still inside the glovebox. Only after the assembly is removed from the glovebox and attached to the beam source is the ampoule broken by flexing the bellows under vacuum. Pumping down with the scroll pump first and only then engaging the turbopump prevents nitrogen from the glovebox atmosphere from overwhelming the turbopump. At minimum two people should be present during the loading procedure, both wearing appropriate PPE (fire-resistant lab coat, face shield, and gloves).

3.5 Custom Nichrome Heaters

To heat my beam source I use custom Nichrome-mica resistive heaters, a design originally developed while working in Professor Tim Kovachy's lab to heat a strontium vapor cell

and later adapted for this beam source.

The heaters use bare 22 AWG Nichrome wire with a resistivity of $r = 1.055\ \Omega/\text{ft}$ [31]. Because the wire is bare, electrical isolation from the surrounding conductive metal structure is provided by flexible mica sheets, which are both non-conductive and rated for sustained high-temperature operation [32].

To characterize the heater performance, I wound different numbers of Nichrome coils (5–13 turns) around a stainless steel cylindrical test reservoir (see Fig. A.3 in Appendix A for reservoir dimensions) and measured the equilibrium temperature reached at a fixed drive current of 5 A. Figure 3.10 shows the heated reservoir during one of these tests, and Fig. 3.11 shows the temperature as a function of time for each coil count. Equilibrium temperatures ranging from $\sim 320°\text{C}$ to $580°\text{C}$ were achieved. The exact resistance for each configuration was not recorded, but can be reconstructed from the wire resistivity and the reservoir geometry.

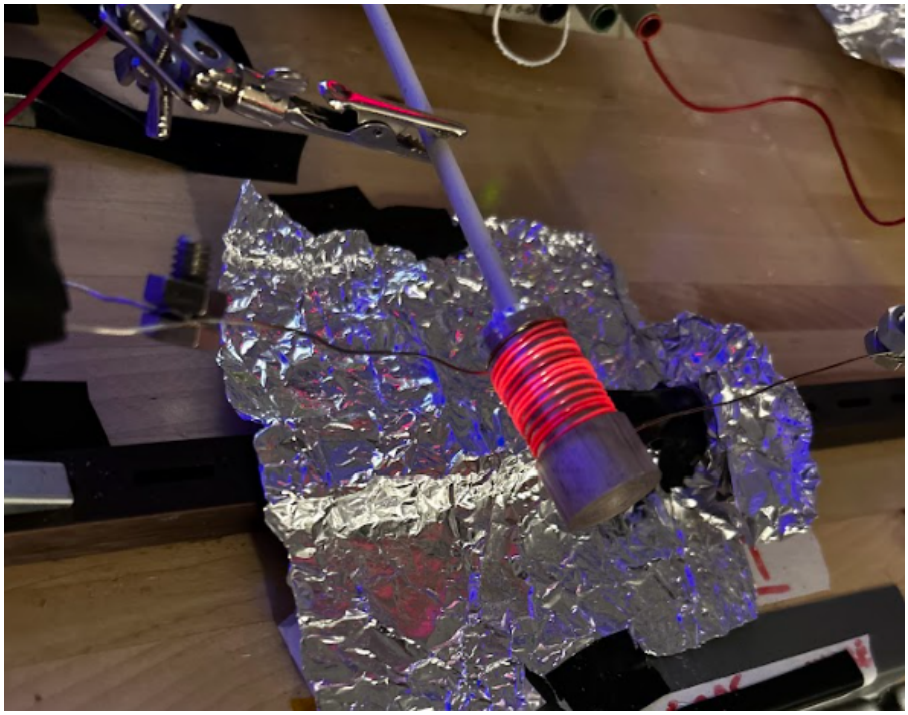


Figure 3.10: Stainless steel cylindrical test reservoir wrapped in a custom Nichrome-mica heater

3.5.1 Nozzle Heater

I now use the same heaters for my beam source, specifically using the same Nichrome-Mica insulated setup for my Nozzle heater, which has held at over 400°C for order ~ 1 week

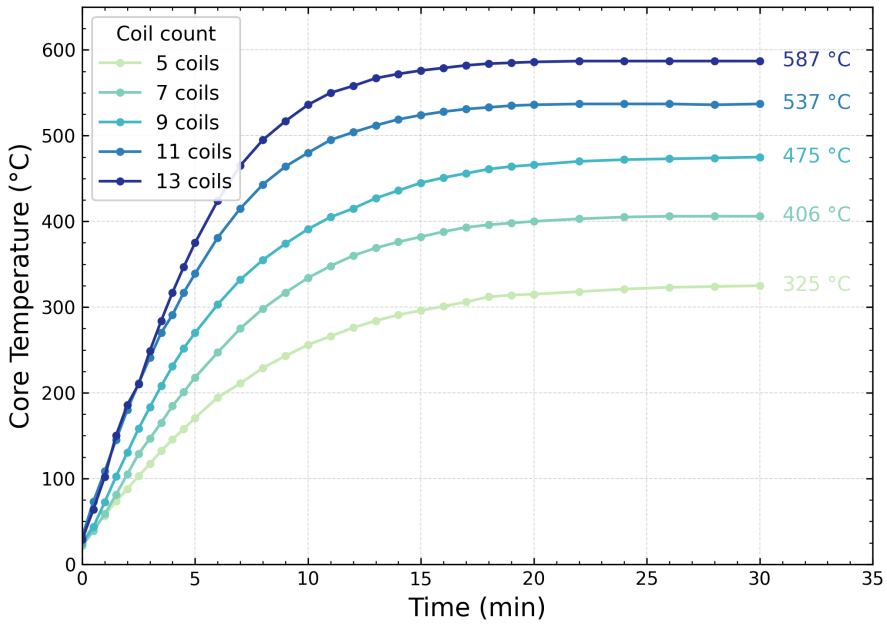


Figure 3.11: Temperature versus time for the stainless steel test reservoir wrapped with different numbers of Nichrome coil turns

when baking our vacuum chamber. Though the nozzle is usually operated around 230°C, we wanted to allow much larger temperatures to be met in case we decide to explore different dopant species with lower vapor pressures in future. In order to operate at temperatures this high for extended periods I also used high temperature crimps that can withstand over 450°C [33] to connect Nichrome to lead wires powered by a Variac Variable Transformer, typically set to ~ 25 V to achieve 230°C.

In order to hold the Nozzle heater around a CF flange, I first place a layer of mica completely covering the flange, then wrap Nichrome on top in a zig-zag pattern (Fig. 3.12), which reduces stray magnetic fields compared to using coils. I then place another sheet of mica on top and tighten everything down with two hose clamps around the flange [34].

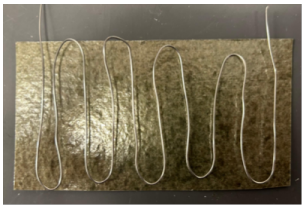


Figure 3.12: Example zig-zag Nichrome routing pattern used for the nozzle heater.

3.5.2 Rb Heaters

To heat the Rb reservoir, reservoir valve, and bellows to the pneumatic bypass valve, I use a simpler method of wrapping Kapton tape around the wires. I also arrange the Nichrome as a twisted pair to again reduce stray magnetic fields. The temperatures required here were low enough that Kapton insulation alone was sufficient. Fig. 3.13 shows and labels all the heaters used on the beam source as well as the resistances of each (see Fig. 3.18 for the same image labeling the rest of the beam source).

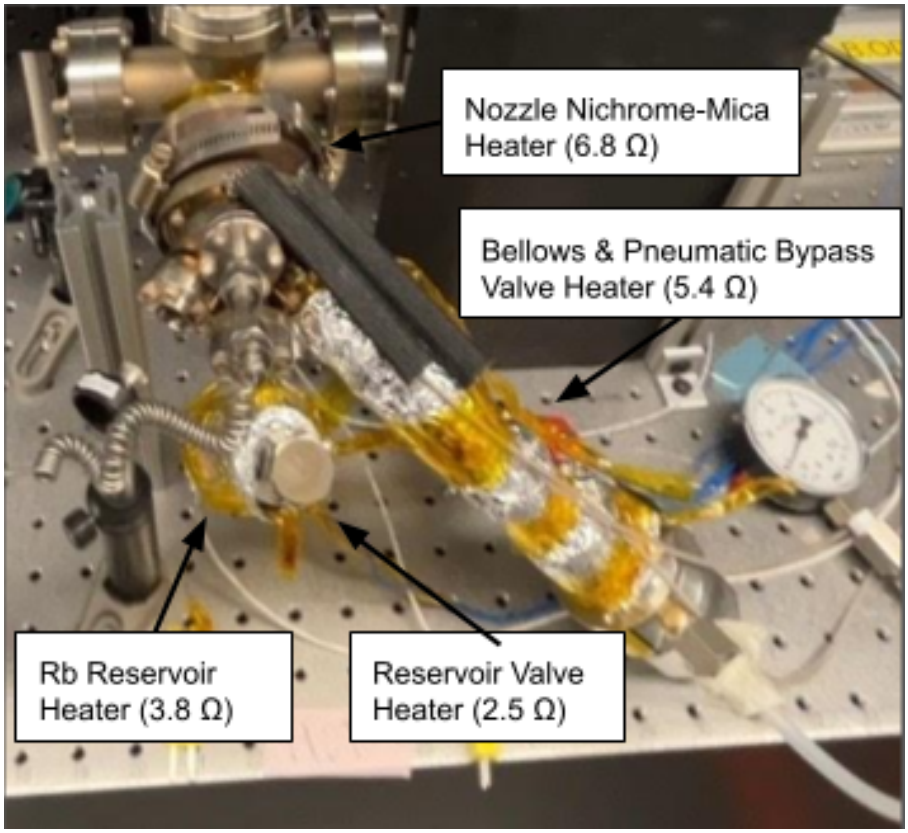


Figure 3.13: Assembled dual-species beam source labeling all heaters. See Fig. 3.18 for the same image with other beam source components labeled.

3.6 Argon Gas Handling System

Ar flow is controlled using an Alicat M-5SCCM-D-DB9M/CM mass flow controller [35] calibrated for argon, with a measurement range of 5×10^{-5} to 5 SCCM (standard cubic centimeters per minute; $\mathrm{cm}^3\,\mathrm{min}^{-1}$ at STP). Because gas can only enter or leave the beam source through the Ar inlet or the nozzle exit, at steady state the flow meter reading equals the Ar flux through the nozzle. It is useful to relate the SCCM reading $\dot{q}$ to the

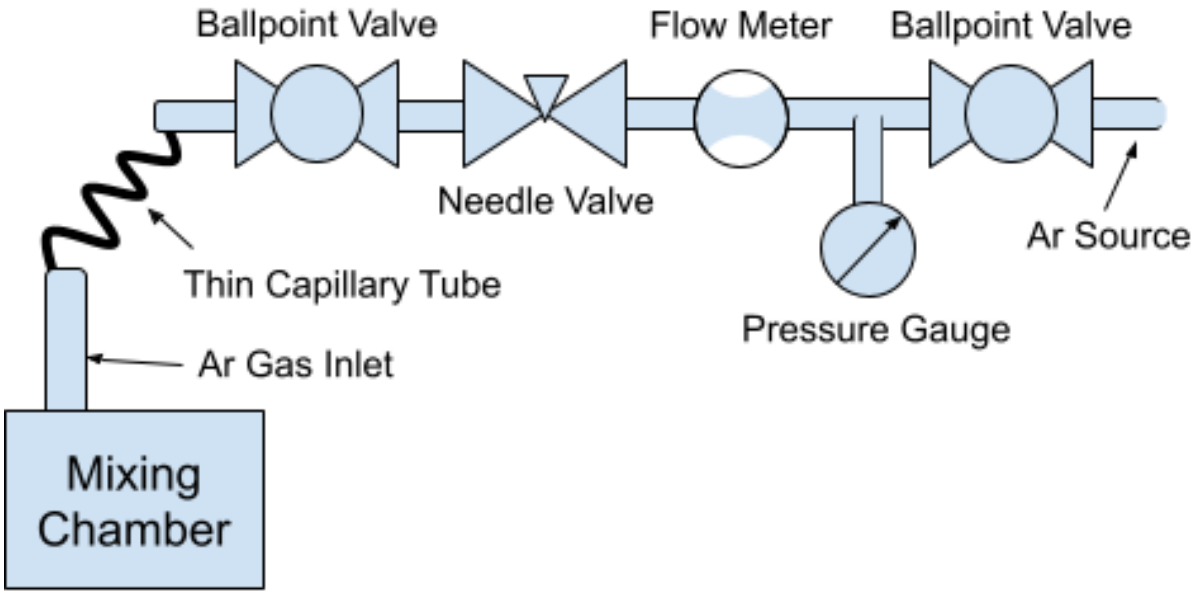


Figure 3.14: Schematic of the Ar gas handling system. A coarse ball valve controls upstream pressure, a pressure gauge ensures the flow controller operates within its specified inlet pressure range of 11.5–160 PSIA [35], and a downstream leak valve and coiled capillary tube provide additional conductance reduction. All fittings are stainless-steel Swagelok.

mass flow rate and growth rate. Using the STP density of argon, $\rho_{Ar,\mathrm{stp}} \approx 1.78$ kg/m^3 (from the ideal gas law at $T_{\mathrm{stp}} = 273.15\,\mathrm{K}$ and $P_{\mathrm{stp}} = 101325\,\mathrm{Pa}$),

$$\dot{m}_{Ar} = \rho_{Ar,\mathrm{stp}}\,\dot{q}, \tag{3.20}$$

and substituting into Eq. 3.10,

$$\dot{h}_{Ar} = \frac{\rho_{Ar,\mathrm{stp}}}{\rho_{Ar}\,\pi r_{gs}^2}\,\dot{q}. \tag{3.21}$$

Inverting, the target growth rates correspond to flow rates of approximately 100 μm/hr $\rightarrow$ 0.13 SCCM, 10 μm/hr $\rightarrow$ 0.013 SCCM, and 1 μm/hr $\rightarrow$ 0.0013 SCCM, well within the range of the chosen meter.

The gas handling system (Fig. 3.14) consists of a coarse ball valve, a pressure gauge, the mass flow controller, a needle valve, a second ball valve, and a thin coiled capillary tube that reduces conductance and provides flow stability. The pressure gauge is required to ensure the flow controller is operated within its specified inlet pressure range of 11.5–160 PSIA [35]. The system currently allows stable Ar flows down to $\sim$0.01 SCCM; reaching the lower growth rates desired will require upgrading the fine control, either through better leak valves or a redesigned conductance geometry.

An earlier version of the gas handling system included a getter filter immediately downstream of the flow meter, intended to further purify the Ar before it entered the beam source. In practice, however, I was never able to achieve stable flow with the getter in line. Even after flowing gas through the getter for $\sim$12 hours or holding at constant pressure for similar timescales with the beam source valved off in hopes of reaching some equilibrium, the flow meter consistently registered a nonzero flow of $\sim$0.01 SCCM toward the getter. Since this is comparable to the lowest growth rates we intend to operate at, it was impossible to determine whether the measured flow was actually entering the beam source or simply being absorbed by the getter. The getter was therefore removed for the current characterization and early crystal-growth work. Incorporating a getter or the full Ar purification system remains important for crystal quality and is needed for future iterations. Additionally, the getter was stored for years prior to my use, and contamination could be a reason for unexplained hysteretic affects.

Although Swagelok fittings are not conventional for UHV systems, the assembled gas handling line has been helium leak tested to below the instrument floor of 7.5×10^{-10} Torr L/s (Fig. 3.15). The Ar gas itself is "Ultra High Purity" grade (99.999% pure; $\leq$ 1 ppm each of O_2 and H_2O [36, 37]) and is not currently passed through a getter purifier, though incorporating one is planned for future crystal-growth experiments. With the gas handling system connected, the characterization chamber (pumped with a scroll pump and turbopump) reaches a pressure near the turbo of $P_{\text{turbo}} \approx 5 \times 10^{-9}$ Torr. In the current crystal growth chamber, the pressure measured immediately downstream of the nozzle exit is $\sim 5 \times 10^{-8}$ Torr.

3.6.1 Impurity Estimates

An important consideration for the gas handling system is whether impurities—either from the gas supply itself or from leaks into the system—could react with the Rb reservoir and deplete the Rb metal. Additionally, since Ar is the dominant species by several orders of magnitude, essentially all gas entering the oven exits through the nozzle and deposits in the growing crystal, so any impurities entering the oven may also be deposited directly into the crystal. The calculations below show that depletion of the Rb source is not a concern at current impurity levels, and they provide a framework for possibly estimating crystal contamination in future work.

For impurities in the gas supply itself, let f_{impur} be the impurity mole fraction of the Ar gas. The impurity mass flow rate is

$$\dot{m}_{\text{impur}} = f_{\text{impur}}\, \dot{m}_{Ar}. \tag{3.22}$$



Figure 3.15: Helium leak test result for the Ar gas handling system, showing a leak rate at or below the instrument floor of 7.5×10^{-10} Torr L/s.

The two most likely reactions are Rb with water ($2\mathrm{Rb} + 2\mathrm{H_2O} \rightarrow 2\mathrm{RbOH} + \mathrm{H_2}$) and Rb with oxygen ($\mathrm{Rb} + \mathrm{O_2} \rightarrow \mathrm{RbO_2}$) [38], both of which consume the Rb and leave the products bound inside the reservoir. Assuming a 1:1 molar reaction ratio, the time to deplete a mass m_{Rb} of Rb becomes

$$t_{\text{deplete}} = \frac{m_{Rb}}{M_{Rb}} \frac{M_{\text{impur}}}{\dot{m}_{\text{impur}}}. \tag{3.23}$$

For $m_{Rb} = 0.1\,\text{g}$, $f_{\text{impur}} = 2\,\text{ppm}$ of water, and a flow rate of 0.13 SCCM (corresponding to 100 μm/hr) $t_{\text{deplete}} \approx 85\,\text{years}$. Therefore, we should not need to worry about the impurity in our gas depleting our Rb.

For leakage from the gas handling system, the molar leak rate is $\dot{n}_{\text{leak}} = \dot{Q}_{\text{leak}}/(RT)$. Assuming the leaked gas reacts with Rb in a 1:1 molar ratio and that 100% of the leak reacts (an overestimate), the depletion time is

$$t_{\text{deplete}} = \frac{m_{Rb}/M_{Rb}}{\dot{n}_{\text{leak}}}. \tag{3.24}$$

Using the measured leak rate $\dot{Q}_{\text{leak}} \leq 7.5 \times 10^{-10}$ Torr L/s gives $t_{\text{deplete}} \approx 900\,\text{years}$, so at the leak rates we currently observe, this is not an issue in terms of depleting our Rb.

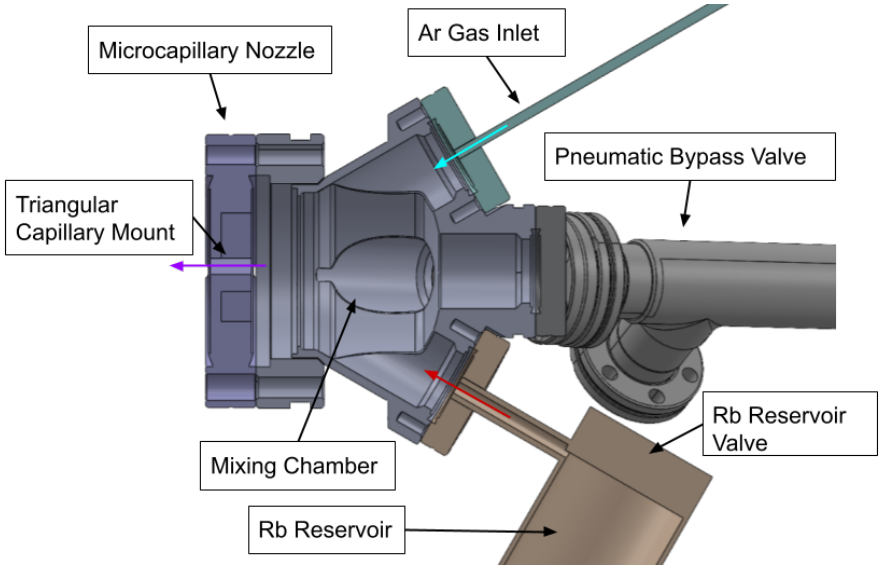


Figure 3.16: **Cross-sectional CAD render of the dual-species beam source assembly.** Argon enters through the Ar gas inlet (top, blue arrow) and Rubidium vapor enters from the heated reservoir (bottom, red arrow) through the reservoir valve. Both species mix in the mixing chamber before passing through the microcapillary nozzle (purple arrow). The pneumatic bypass valve allows the system to be pumped down without flowing gas through the capillaries, reducing pump-down time.

These impurities, however, may be a larger issue in terms of crystal purity, but that estimate is left for future work.

3.7 Beam Source Full Assembly

A diagram of the assembled dual-species beam source is shown as a cross-section in Fig. 3.16 and with an exterior view in Fig. 3.17. A labeled image of the physical assembly is seen in Fig. 3.18.

Ar enters from the top through the gas inlet and Rb vapor enters from the bottom through the reservoir leak valve. Both mix in the central mixing chamber before exiting through the microcapillary nozzle toward the growth substrate. An additional pneumatic bypass valve is added to connect the mixing chamber directly to the growth chamber, allowing the system to be pumped down without flowing gas through the capillaries and thereby significantly reducing pump-down time. An optical viewport is added to the mixing chamber allowing optical access for diagnostics (e.g. checking for florescence to ensure we have Rb).

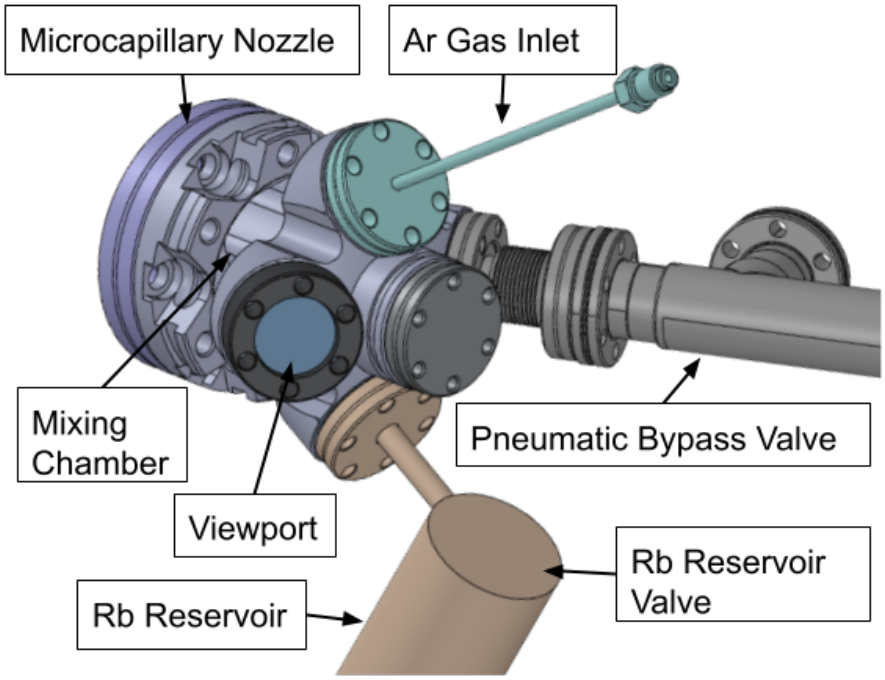


Figure 3.17: **External CAD render of the dual-species beam source assembly.** The exterior view shows the overall geometry of the assembled source, including the optical viewport on the mixing chamber. Component labels are consistent with Fig. 3.16.

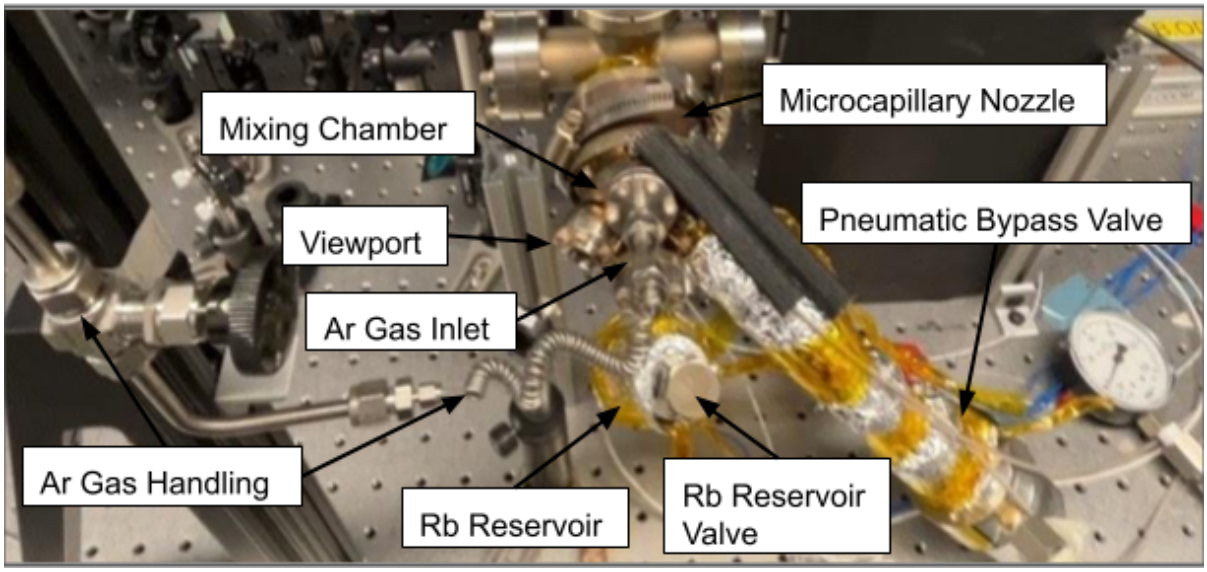


Figure 3.18: **Assembled dual-species beam source.** Component labels correspond to those in the CAD renders of Figs. 3.16 and 3.17. The Ar gas handling hardware visible at left connects to the flow meter and the rest of the gas handling system. Heater foil and wiring are described in Fig. 3.13.

Chapter 4

Beam Characterization: Setup and Methods

This chapter describes the experimental methods used to characterize the dual-species Rb-Ar beam source. Rubidium absorption spectroscopy serves as the primary diagnostic. By scanning a narrow 780 nm probe beam across the Rb atomic beam and recording the transmitted intensity, we extract the Rb column density, spatial profile, divergence angle, and total flux. The Ar component of the beam is not probed optically in the same manner, but from arguments in Chapter 3, we assume the Ar and Rb beam follow same path; additionally, its flux is inferred from the calibrated mass-flow meter described in Chapter 3.

The chapter is organized as follows: Sec. 4.1 describes the UHV chamber geometry; Sec. 4.2 describes the optical spectroscopy setup and probe beam characterization; Sec. 4.3 covers the signal-conditioning circuit; and Secs. 4.4–4.6 develop the data analysis pipeline for extracting divergence and flux from the absorption data.

4.1 Rb-Ar Beam Characterization Chamber

To characterize the dual-species Rb-Ar beam source, I assembled a dedicated UHV chamber separate from the crystal growth chamber (not ready yet at time of characterization). The beam source mounts to the top of a vertical stainless-steel cross, with the beam traveling downward along the z direction as defined in Fig. 4.1. The chamber is pumped by a scroll and turbo pump. Without Ar gas flowing or beam source heaters on the base pressure measured near the turbo reaches $P_{\text{turbo}} \approx 5 \times 10^{-9}$ Torr. A Stanford Research Systems residual gas analyzer 300 [39] is used to both leak check chamber and ensure Ar flow during dual-species beam characterization.

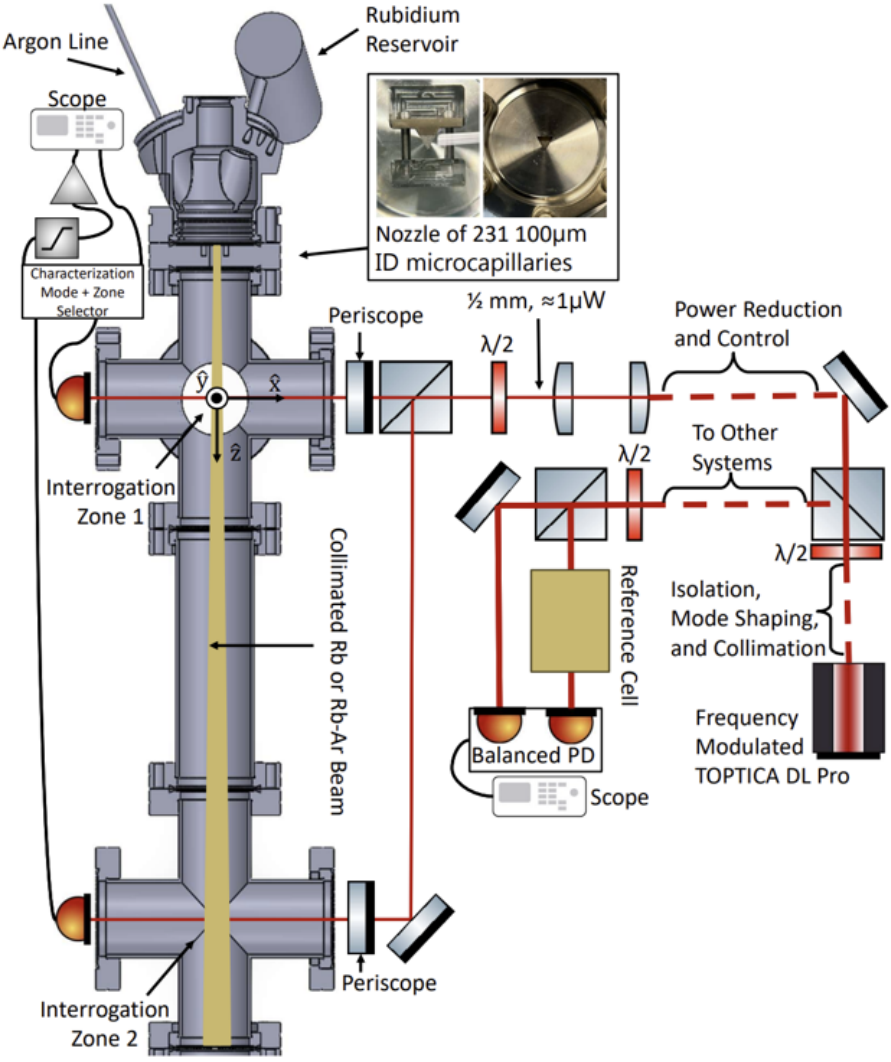


Figure 4.1: **Schematic diagram of dual-species beam source characterization setup.**

Two view-ports serve as optical interrogation zones at distances $z_1 \approx 2.46\,\text{in}$ and $z_2 \approx 12.3\,\text{in}$ from the nozzle exit face, measured along axis of Rb-Ar beam propagation. The growth substrate in the actual crystal growth chamber will be located at $z_{\text{gr}} \approx 19.7\,\text{in}$ from the nozzle face. z_1 and z_2 give the two positions where transverse absorption profiles of the Rb beam are recorded. A periscope arrangement at each zone (described in Sec. 4.2.3) redirects the 780 nm probe beam to perpendicularity intersect the Rb beam, and allows the probe height Δy to be scanned across the beam profile.

Images of full characterization chamber and setup seen in Fig. 4.2 and 4.3

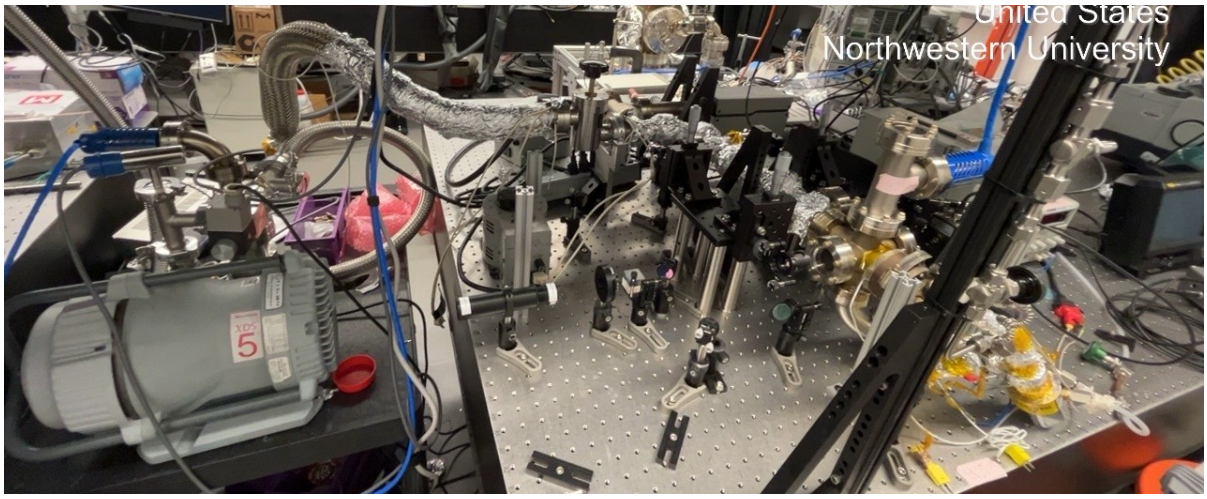


Figure 4.2: **Image of dual-species beam source characterization chamber.**

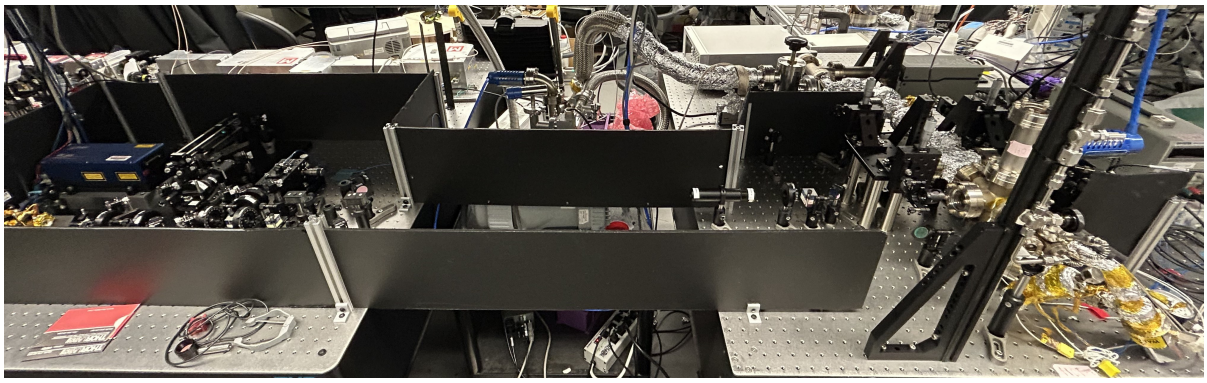


Figure 4.3: Image of dual-species beam source characterization chamber and optics

4.2 Rubidium Absorption Spectroscopy: Optical Setup

4.2.1 Laser source and controller

To probe the Rb component of the dual-species beam, we use an 80 mW Toptica DL Pro External-Cavity Diode Laser (ECDL) operating near 780 nm [40]. The ECDL used, however, is older and recommissioned, and the output power only reaches $\sim$ 20 mW. Frequency and intensity control are provided by a Toptica DC 110 Supply Rack holding an SC 110 scan controller, a DTC 110 temperature controller, and a DCC 110 current controller [41].

4.2.2 Probing Desired Transition

We characterize the beam by probing the ^{85}Rb D_2 line, specifically the $F = 3 \rightarrow F' = 4$ hyperfine transition, which is the most prominent absorption feature of natural-abundance

Rb [25]. Because the probe beam crosses the Rb beam perpendicularly, the thermal atomic velocities along the probe direction is small, strongly suppressing Doppler broadening. This allows us to resolve the individual hyperfine components that would otherwise be blurred into a single Doppler-broadened spectrum (see Fig. 4.5).

A simplified schematic of the optical path from the laser to the vacuum chamber is shown in Fig. 4.4. To identify the correct resonance we first use a Rb reference cell with a balanced photodiode. The reference cell provides an absorption spectrum that confirms we are near the ^{85}Rb D_2 $F = 3$ ground-state manifold, but the $F' = 2$, 3, 4 excited-state features are blurred together and unresolved at room temperature. Fine-tuning to the specific $F = 3 \rightarrow F' = 4$ component is accomplished using the beam absorption signal itself (Fig. 4.5), where the diode temperature is adjusted via the DTC 110 to shift the laser frequency while keeping the output power constant. The scan controller is not used for this step, as enabling the scan modulation caused the laser frequency to drift more rapidly than with it off. Throughout all measurements the laser was unlocked as the $F = 3 \rightarrow F' = 4$ absorption feature remained at a stable position on the timescale of a full divergence measurement run ($\sim$ 1 to 2 hours).

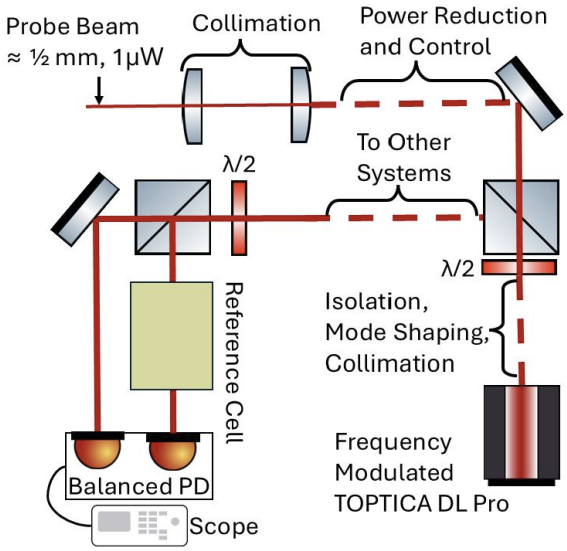


Figure 4.4: Simplified optics diagram of probe beam preparation for Rb beam spectroscopy and analysis.

4.2.3 Spatial scanning and periscope system

In order to get the divergence of our beam, we first need to map the transverse profile of the Rb beam. The probe is scanned vertically across the Rb beam using a periscope arrangement (Fig. 4.6). A first mirror redirects the horizontally propagating probe beam

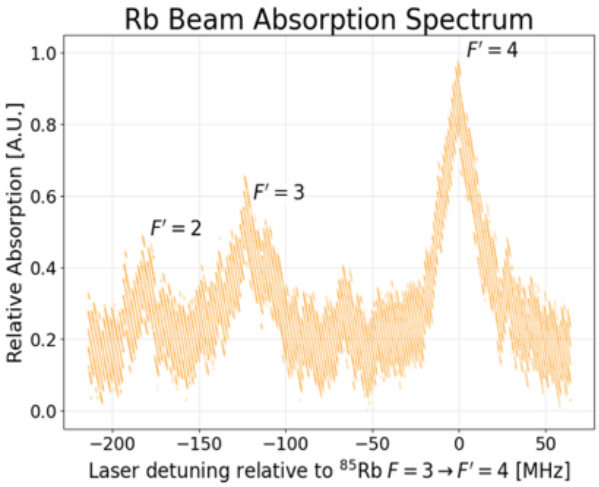


Figure 4.5: Rb absorption spectrum from collimated Rb beam probed perpendicularly to Rb beam propagation. Due to high collimation Doppler broadening is negligible, allowing one to fully resolve all hyperfine excited state transitions.

upward along the y-direction, and a second, upper mirror then redirects it back along x so that it crosses perpendicularly to the Rb-Ar beam (which travels along z) and reaches the photodiode on other far side. Both the upper periscope mirror and the photodiode are mounted on independent manual translation stages and aligned, allowing the probe height Δy to be varied with fine control. Before taking absorption measurements, the stages are aligned by verifying uniform probe intensity across several Δy positions with no Rb beam present, ensuring that the probe-photodiode alignment does not shift as the stages are moved.

A simple schematic of the characterization setup—including the laser optical chain, reference cell, periscope, and photodetector—is shown in Fig. 4.1.

4.2.4 780 nm Probe Beam Characterization

Accurate absorption measurements require knowing both the spatial extent and the intensity of the probe beam. For a Gaussian beam the effective cross-sectional area is

$$A_{\text{eff}} = \pi w^2, \tag{4.1}$$

where w is the $1/e^2$ intensity radius [42].

Beam-width measurement: The full $1/e^2$ beam diameter $2w$ is measured by imaging the 780 nm beam on a ThorCam DCC1545 monochrome camera (square pixels with side

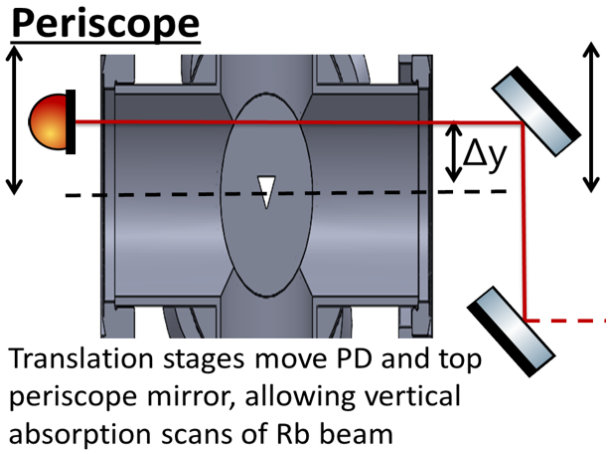


Figure 4.6: Periscope setup to move probe beam up and down along Rb beam and record its spatial profile,

length of 5.2 μm) [43]. A Gaussian fit to the intensity profile (Fig. 4.7) gets $w_{\text{probe}} = 0.275\,\text{mm}$.

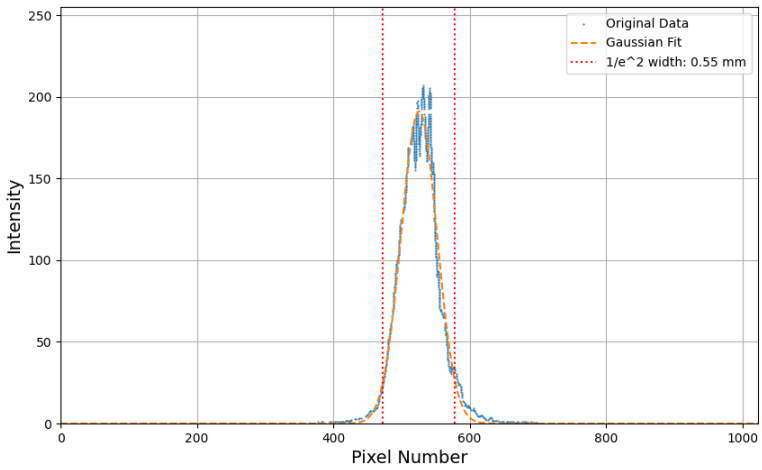


Figure 4.7: Gaussian fit to the 780 nm probe beam intensity profile imaged on a ThorCam DCC1545 camera.

We also verify that the probe beam is sufficiently small that its finite width does not blur the divergence profiles. The inscribed-circle diameter of the triangular microcapillary nozzle array is $D_{\text{nozzle}} \approx 2.5\,\text{mm}$, so

$$2w_{\text{probe}} = 0.55\,\text{mm} \approx 0.22\,D_{\text{nozzle}}, \tag{4.2}$$

which should be below the nozzle scale enough. Additionally, because the Rb beam is

expected to be wider than D_{nozzle} when we probe it, this probe diameter should provide adequate spatial resolution. In practice, making the beam significantly smaller also becomes difficult as keeping the optical power low enough to prevent saturation becomes more difficult.

Probe beam intensity: The probe intensity is

$$I_{\text{probe}} = \frac{P_{\text{probe}}}{\pi w_{\text{probe}}^2}, \tag{4.3}$$

where P_{probe} is the incident power. We measure P_{probe} using a ThorLabs PDA36A amplified silicon photodetector at the 70 dB gain setting, which gives a transimpedance gain of 2.38×10^6 V/A with a 50 Ω terminator and a responsivity $R(780) \approx 0.48$ A/W at 780 nm [44], so the incident power is then

$$P_{\text{probe}} = \frac{V_{\text{out}}}{\text{Gain} \times R(\lambda)}. \tag{4.4}$$

During characterization measurements the scope typically reads $V_{\text{out}} \approx 1$ V, giving $P_{\text{probe}} \approx 0.9\,\mu$W and therefore

$$I_{\text{probe}} \approx 0.37\,\text{mW/cm}^2 \ll I_{\text{sat}} = 3.895\,\text{mW/cm}^2. \tag{4.5}$$

With $I_{\text{probe}}/I_{\text{sat}} \approx 0.1$, power broadening of the transition linewidth is negligible (see Eq. 4.7 below) and the optically thin, low-saturation approximations used in Sec. 4.6 are well justified.

Operating far below saturation serves two purposes. The primary one is that Beer-Lambert law in its simple form (Eq. 4.16) is only valid when $I \ll I_{\text{sat}}$. At high intensity, stimulated emission partially cancels absorption, and the absorption coefficient becomes intensity-dependent [45],

$$\kappa(\omega, I) = \frac{N\sigma(\omega)}{1 + I/I_{\text{sat}}}, \tag{4.6}$$

which reduces to $\kappa \approx N\sigma(\omega)$ only when $I \ll I_{\text{sat}}$. This intensity-independent limit is what allows Beer-Lambert law to hold and the column-density derivation in Sec. 4.6 to be valid. The secondary consequence is power broadening of the transition linewidth (Eq. 4.7), which would bias the Lorentzian fits in Sec. 4.4 if not operating with $I \ll I_{\text{sat}}$.

$$\Delta_{\omega_{\text{FWHM}}} = \Gamma\left(1 + \frac{I}{I_{\text{sat}}}\right)^{1/2}, \tag{4.7}$$

4.3 Signal Conditioning: Filter-Amplifier Circuit

The raw photodetector output contains a fractional absorption signal of only $\sim 0.05\,\%$ riding on a $\sim 1\,\mathrm{V}$ DC background, with an additional 250 Hz, $\sim 4\,\mathrm{mV}$ amplitude sawtooth modulation imposed by the laser frequency scan (Fig. 4.8). Near the edges of the beam where the Rb density is low, the absorption signal is even smaller. An additional practical limitation comes from the vertical resolution of the oscilloscope, as at maximum resolution, each absorption peak spans only a few counts, making raw data imprecise.

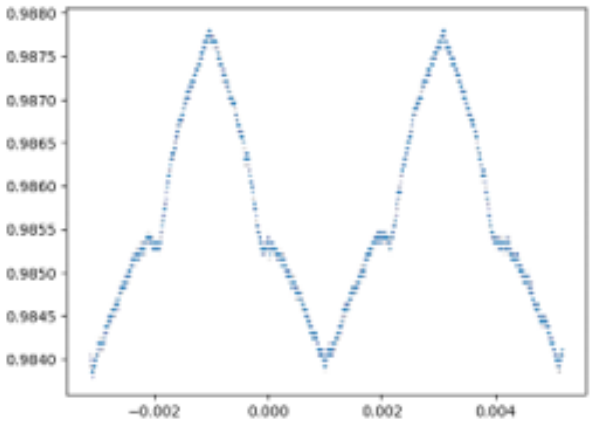


Figure 4.8: Raw photodetector output showing the $\sim 1\,\mathrm{V}$ DC background with 250 Hz, 4 mV sawtooth modulation from the laser frequency scan. $\sim 0.05\,\%$ fractional absorption signal.

To recover the absorption signal, the detector output passes through a two-stage signal conditioning circuit. A RC high-pass filter that removes the DC offset, followed by a non-inverting op-amp stage that amplifies the AC component containing the absorption features. A schematic diagram and image of the circuit are shown in Figs. 4.9 and 4.10.

The high-pass cutoff frequency is

$$f_c = \frac{1}{2\pi RC} = \frac{1}{2\pi \times 1\,\mathrm{M\Omega} \times 10\,\mathrm{nF}} \approx 15.9\,\mathrm{Hz}, \tag{4.8}$$

which passes the 250 Hz scan signal while suppressing the DC component. The non-inverting amplifier gain is set by a $100\,\mathrm{k\Omega}$ potentiometer in series with a $1.5\,\mathrm{k\Omega}$ resistor, with a second $1.5\,\mathrm{k\Omega}$ resistor to ground, giving a variable gain with a maximum of

$$G = 1 + \frac{R_f}{R_g} = 1 + \frac{101.5\,\mathrm{k\Omega}}{1.5\,\mathrm{k\Omega}} \approx 68.7\times . \tag{4.9}$$

At 250 Hz the high-pass filter introduces a phase shift of $\varphi = \arctan(f_c/f) \approx 3.6^\circ$ [46], which causes a slight curvature of the signal after the conditioning circuit. This residual

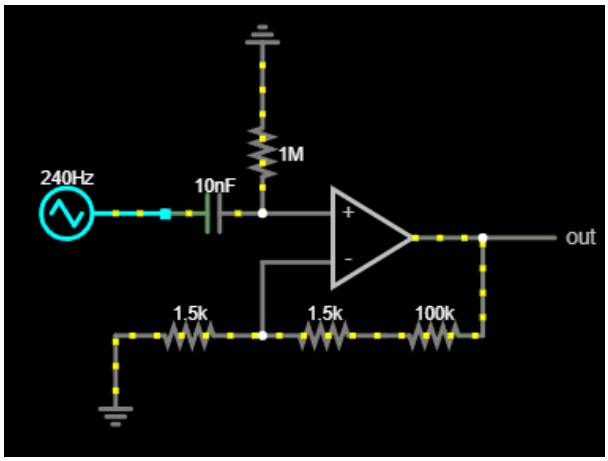


Figure 4.9: Schematic of the two-stage signal-conditioning circuit.

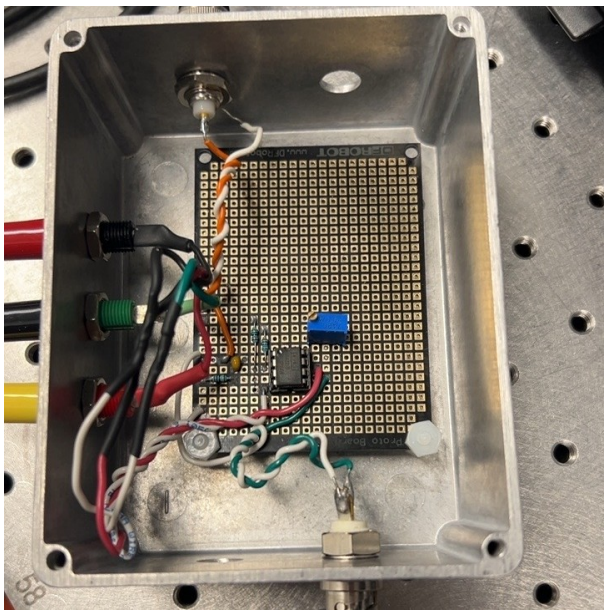


Figure 4.10: Photograph of the assembled filter-amplifier circuit.

curvature is removed during analysis by fitting and subtracting a second-order polynomial from each sweep to account for ramp background and phase shift curvature (Sec. 4.4).

4.3.1 Validity of Conditioned Signal for Relative Absorption

The conditioning circuit is used for divergence measurements, which require only the *relative* spatial variation of the absorption across the beam profile. It is not used for flux measurements, which require the absolute incident intensity I_0 (Sec. 4.6).

The fractional absorption at any probe position is $A = 1 - I/I_0$, where I_0 is the incident probe intensity and I is the transmitted intensity on resonance. The key point

is that I_0 is the same at every transverse position Δy, determined by the probe beam power, which does not change as the translation stages are moved. The only quantity that varies with position is the transmitted intensity $I(\Delta y)$, which carries the spatial absorption information.

The high-pass filter removes the DC component (effectively removing information on the absolute value of I_0) but since I_0 is constant across all probe positions, the relative variation of $I(\Delta y)$ between positions is retained. The subsequent amplification rescales all signals by the same factor G, leaving relative absorption unchanged. For flux measurements, where I_0 must be known absolutely, the raw photodiode voltages are recorded directly.

4.4 Data Acquisition and Analysis Pipeline

The oscilloscope records voltage traces of the amplified photodetector signal as the laser frequency is swept through the $F = 3 \rightarrow F' = 4$ resonance. Each acquisition is time averaged and captures both two rising and two falling ramp halves of the sawtooth sweep, which are treated as independent samples and averaged to reduce systematic effects (See Fig. 4.11 **(a)**).

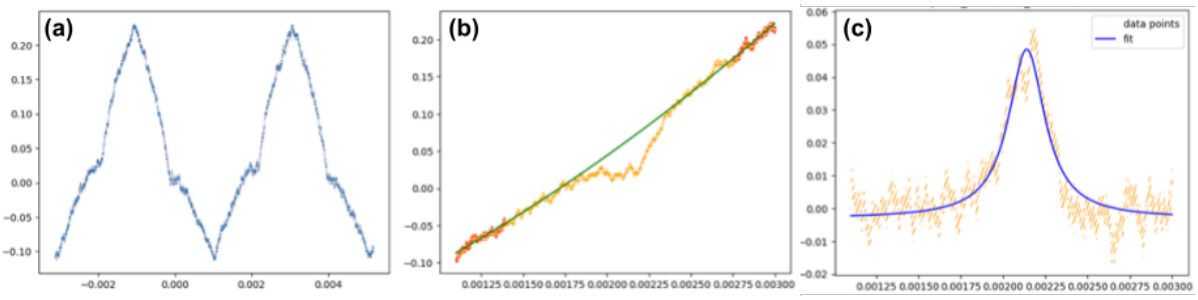


Figure 4.11: **Data acquisition and analysis pipeline visualized**. (a) Full sawtooth ramp showing two rising and two falling sweeps used as independent samples. (b) Degree-2 polynomial background fit (green) to subtract from each ramp. (c) Lorentzian fit to the absorption feature after background removal to extract relative absorptions.

The analysis pipeline proceeds as follows. All steps are first performed manually for one or two locations of probe beam in order to properly assign initial fit parameters, and then the same parameters are blindly used on all other probe positions to reduce bias.

1. Separate the raw trace into individual ramp sides (up-sweep and down-sweep).
2. Fit and subtract a degree-2 polynomial background from each side to remove the ramp caused by the frequency modulation of ECDL. The reason for degree-2

polynomial instead of linear fit is again from the slight curvature introduced by the filter phase shift (Sec. 4.3). Practically, when doing this the fit is done on the extreme sides of the signal to prevent capturing the absorption dip itself. See Fig. 4.11 **(b)** for example of fit that will be subtracted..

3. Fit a Lorentzian (Eq. 4.10) to the absorption feature after subtracting background from ECDL ramp (Fig. 4.11 **(c)**). Because Doppler broadening is significantly suppressed in our setup, a Lorentzian is more appropriate to capture linewidth than gaussian.

$$\mathcal{L}(\Delta\nu) = \frac{S}{1 + \left(\Delta\nu \,/\, (\Gamma/2)\right)^2}, \tag{4.10}$$

where S is the peak relative absorption and Γ is the full width at half-maximum (Technically not fitting with $\Delta\nu$ but time, as the scope trace is over time, but because we are using a linear frequency ramp these are directly proportional). In practice, this fit is performed numerically using the `scipy.optimize.curve_fit` function in Python [47].

4. Using the fitted Lorentzian we can then extract the height of each peak at given probe position Δy. We then average over each of the 4 different ramp sections (See Fig. 4.11 **(a)**) to report a spatial profile of $A(\Delta y)$, which corresponds to the relative absorption distribution to be used for divergence measurements (Sec. 4.5) and rescaled for flux analysis (Sec. 4.6)

5. To get the error of the height, we use the standard deviation between each of the 4 different ramp sections (See Fig. 4.11 **(a)**). The standard deviation between each side of the ramp is already significantly larger (more than order of magnitude) than the error from the fit parameters. Standard deviation is also used rather than standard error of the mean as the difference between ramp appears to reflect systematic variability, not statistical noise on a single well-defined quantity.

4.5 Divergence Measurement

Once a spatial profile is created by sweeping the probe beam over the Rb beam as described in Sec. 4.2.3 and we extract the relative absorption of each point to create a spatial profile of absorption, $A(\Delta y)$, as described in Sec. 4.4, we can use these distributions and their widths to extract divergence. Specifically, we fit with both a Gaussian and Lorentzian. The reason for fitting with both is first motivated by Senaratne et al.'s claim

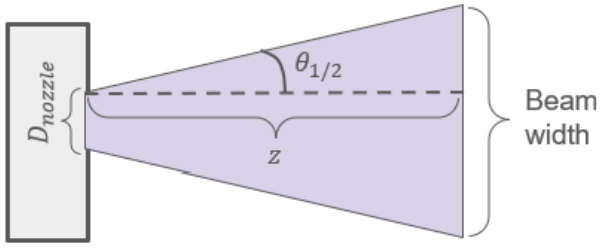


Figure 4.12: Diagram of how divergence is defined using method A. Eq. 4.11

that the edges of the intensity distribution from their simulated capillaries have broad non-gaussian shoulders and a tall central peak [17]. Additionally, it is again not clear how a large array of a triangularly bundled capillaries convolve the individual capillary profile. Chapter 5 will go into much more detail on both these methods.

After fitting $A(\Delta y)$ with a Gaussian or Lorentzian we can extract the FWHM to define the beam width w. The half-angle divergence of the Rb beam can then be extracted by two different methods, which differ in how they relate the measured beam width to a geometric angle.

Method A — single-zone nozzle geometry. In this approach the beam width is measured at a single distance z from the nozzle exit and the half-angle is defined as

$$\theta_{1/2}^{(\mathrm{A})} \equiv \arctan(\delta/z), \tag{4.11}$$

where

$$\delta = (w - D_{\mathrm{nozzle}})/2. \tag{4.12}$$

See Fig. 4.12 for simple visual of how this divergence is measured and defined.

Method B — two-zone differential. The preferred method uses beam-width measurements at two axial positions z_1 and z_2, converting the growth in width to a half-angle directly:

$$\theta_{1/2}^{(\mathrm{B})} \equiv \arctan\left(\frac{(w_2 - w_1)/2}{z_2 - z_1}\right). \tag{4.13}$$

By taking the *difference* of widths, Method B cancels the contribution of the finite source size and measures only the geometrical expansion of the beam between the two interrogation zones (See Fig. 4.13). While this method is more informative, it has unfortunately only been performed with just a Rb beam as it is more time consuming and

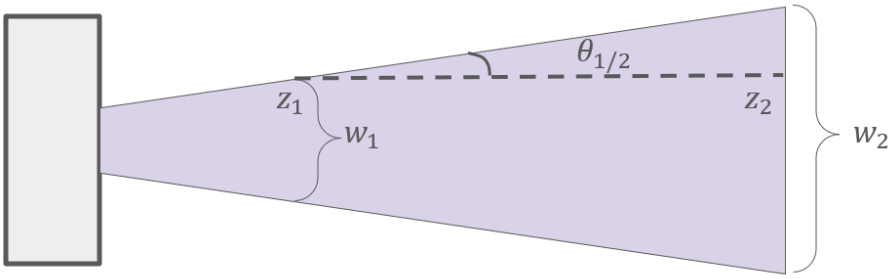


Figure 4.13: Diagram of how divergence is defined using method B. Eq. 4.13

complicated. This method is also unusable in the current apparatus of growing crystals and continued characterization of dual species beam due to geometry constraints.

4.5.1 Capture Efficiency

With the beam divergence $\theta_{1/2}$ and a measured width w measured at distance z from the nozzle we can extract a "capture efficiency" P_{capt}. This will represent the fraction of total beam flux that makes it all the way down the tube towards the growth substrate. However, it does not account for the capture efficiency purely where the crystal is being grown, as this may differ, but regardless, the capture efficiency will give a growth rate at that location z regardless of actual area of crystal we grow.

The beam travels down a 1 cm diameter aperture to the growth substrate, located at $z_{\text{gr}} = 19.685$ inches from the nozzle. Propagating the beam geometrically from the measurement zone, the predicted full beam width at the substrate is estimated to be

$$w_{\text{gs}} = w + 2\,(z_{\text{gr}} - z)\tan\theta_{1/2}. \tag{4.14}$$

Given this width, we model the beam profile at the substrate using the same functional form used to fit the measured spatial profile but normalized, $f(y)$, and integrate across the aperture

$$P_{\text{capt}} = \int_{\text{aperture}} f(y)\,dy. \tag{4.15}$$

4.6 Flux Measurement

This section derives the expression relating the measured fractional absorption at each probe position to a total Rb flux. The chain has four steps: (i) extract column density

N_{col} from the absorption, (ii) integrate across the beam profile to obtain a linear density N_{slice}, (iii) multiply by the mean atomic speed to get the partial flux $\Phi_{^{85}\text{Rb},\,F=3}$, and (iv) apply statistical correction factors to recover the total Rb flux.

4.6.1 Column Density from Beer-Lambert Law

In the limit $I \ll I_{\text{sat}}$, stimulated emission is negligible and nearly all atoms remain in the ground state. Under this condition the absorption coefficient $\kappa = N\sigma(\omega)$ is intensity-independent, and integrating $dI/dz = -\kappa I$ over the beam path through the atomic sample gives the Beer-Lambert law [45]

$$I = I_0 \exp(-\text{OD}), \tag{4.16}$$

where the optical depth is

$$\text{OD} = \sigma_{\text{eff}}\, N_{\text{col}}. \tag{4.17}$$

Here $N_{\text{col}} = \int n\, dz$ (cm^{-2}) is the column density integrated through the beam along the probe direction, and $\sigma_{\text{eff}} = 1.246 \times 10^{-9}\,\text{cm}^2$ is the resonant cross-section for the ^{85}Rb D_2 $F = 3 \to F' = 4$ transition averaged over isotropic light polarization [25]. The isotropic average is appropriate here because the Rb atoms have a thermal distribution across all m_F sublevels and the probe is linearly polarized with no preferred axis relative to the atomic quantization.

Because we operate in the optically thin limit (OD $\ll 1$, see Fig. 4.8), the exponential can be expanded to first order Taylor approximate to give the fractional absorption as

$$A \equiv 1 - \frac{I}{I_0} = 1 - \exp(-\text{OD}) \approx \text{OD}, \quad \text{OD} \ll 1, \tag{4.18}$$

and inverting for column density,

$$N_{\text{col}} \approx \frac{A}{\sigma_{\text{eff}}} \quad [\text{cm}^{-2}]. \tag{4.19}$$

In practice, column density is only extracted for one position of the probe beam, then the relative absorption distribution is rescaled appropriately. This is largely because, as explained in Sec. 4.3, without the amplification set up, getting a pure signal with good enough resolution near the sides of the Rb beam become intractable.

4.6.2 Linear Density and Flux

Integrating the column-density profile across the transverse extent of the beam (i.e. over the probe scan axis y) gives the linear density of a slice of the Rb beam in the direction of its propagation:

$$N_{\text{slice}} = \int_{\text{beam profile}} N_{\text{col}}(y)\, dy \quad [\text{cm}^{-1}]. \tag{4.20}$$

Converting this linear density to a flux (atoms/s) requires multiplying by the mean atomic speed. For atoms in an effusive beam at source temperature T, the mean speed is [19]

$$\bar{v} = \sqrt{\frac{8k_B T}{\pi m_{\text{Rb}}}}, \tag{4.21}$$

giving the flux of the probed state,

$$\Phi_{^{85}\text{Rb},\, F=3} = N_{\text{slice}}\, \bar{v}. \tag{4.22}$$

4.6.3 Isotopic and Hyperfine Population Corrections

Equation 4.22 accounts only for the ^{85}Rb atoms in the $F = 3$ ground state. Two correction factors are needed to recover the total Rb flux.

Hyperfine population fraction. At thermal equilibrium the ground-state population is distributed among the hyperfine levels in proportion to their degeneracies $(2F+1)$. For ^{85}Rb ($I = 5/2$) the ground states are $F = 2$ (five sublevels) and $F = 3$ (seven sublevels), so the fraction in $F = 3$ is

$$f_{F=3} = \frac{(2 * 3 + 1)}{(2 * 2 + 1) + (2 * 3 + 1)} = \frac{7}{12}. \tag{4.23}$$

The total ^{85}Rb flux is therefore

$$\Phi_{^{85}\text{Rb}} = \frac{\Phi_{^{85}\text{Rb},\, F=3}}{f_{F=3}} = N_{\text{slice}}\, \bar{v}\, \frac{12}{7}. \tag{4.24}$$

Natural-abundance correction. Our Rb sample is of natural isotopic composition. ^{85}Rb has a natural abundance of $P_{85} = 72.17\,\%$ [25]. The total Rb flux is then

$$\Phi_{\text{Rb}} = \frac{\Phi_{^{85}\text{Rb}}}{P_{85}} = \frac{N_{\text{slice}}\, \bar{v}}{P_{85}\, f_{F=3}} = N_{\text{slice}}\, \bar{v} \times \frac{12}{7 \times 0.7217}. \tag{4.25}$$

Numerical results for Φ_{Rb} under the experimental conditions studied are presented in Chapter 5.

Chapter 5

Beam Characterization: Results and Discussion

This chapter presents results from the characterization of my dual-species Rb-Ar beam source described in Chapters 3 and 4. The final results are summarized in Table. 5.1 and Fig. C.7 in Appendix C. The results here should be understood as first-order estimates, as this is an early-stage characterization and many of the findings depend substantially on how the beam profile is modeled and how divergence is defined.

The central goal of the characterization is to determine the beam half-angle divergence $\theta_{1/2}$, the Rb atomic flux, and the capture efficiency at the growth substrate. I assume the Ar flow rate in and out of the beam source are the same and Ar and Rb follow the same path. What we can say now comes from Rb absorption spectroscopy and mass-flow measurements along with the assumption that Rb and Ar travel the same path through the microcapillary array (discussed in Chapter 3).

Operating conditions. All data in this chapter were taken under the following conditions:

- Nozzle temperature: $\sim 230°C$
- Rb reservoir temperature: $\sim 100°C$
- Bellows temperature: $\sim 100°C$
- Background pressure during operation (no Ar flow): $\sim 8 \times 10^{-9}$ Torr (Turbo)
- Ar flow rate (mass-flow controller): ~ 0.01 SCCM

5.1 Beam Divergence: Pure Rubidium

In these measurements only the Rb beam was present. This will be a good comparison to see what changes when we introduce an Ar beam. All individual per-position relative absorption fits as well as percent absorption fits used to rescale distribution for this dataset are shown in Appendix C, Sec. C.0.1.

5.1.1 Method A: Single-Zone Nozzle Geometry

Method A (Eq. 4.11–4.12) uses the width of the beam profile at a single distance z from the nozzle, combined with the known nozzle diameter (diameter of inscribed circle of triangular nozzle) $D_{\text{nozzle}} \approx 0.1$ inch, to infer the geometric half-angle. Results from Zone 1 (distance $z_1 \approx 2.46$ in from nozzle exit) and Zone 2 ($z_2 \approx 12.3$ in) are shown in Figs. 5.1–5.4, for both Gaussian and Lorentzian fits to the transverse profile $A(\Delta y)$.

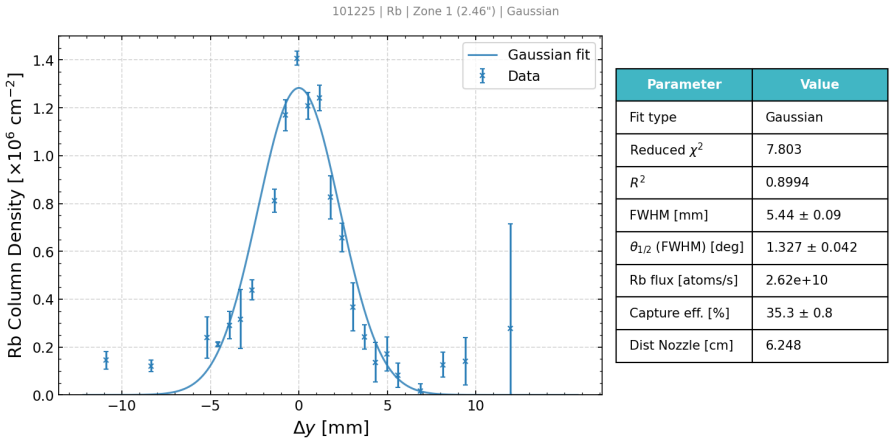
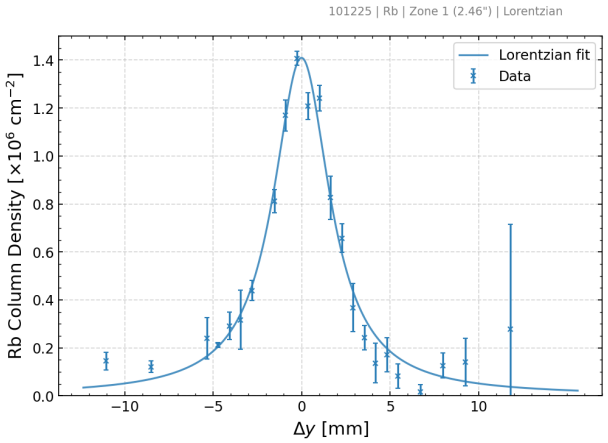


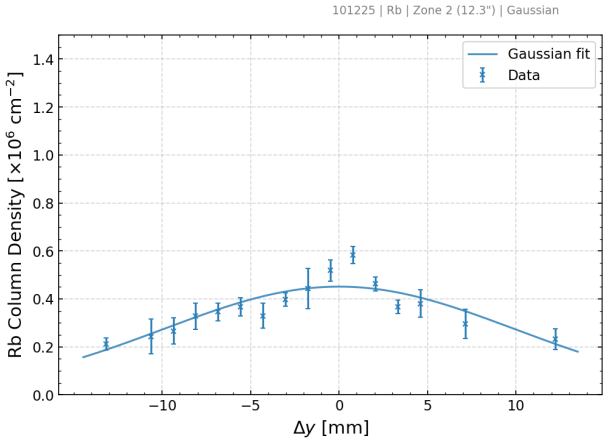
Figure 5.1: Zone 1 pure-Rb spatial profile fitted with a Gaussian. The relatively large reduced chi-squared indicates the Gaussian is not an ideal model for the Zone 1 profile; see Sec. 5.4.

Zone 1 Measurement:



Parameter	Value
Fit type	Lorentzian
Reduced χ^2	2.462
R^2	0.9569
FWHM [mm]	3.90 ± 0.10
$\theta_{1/2}$ (FWHM) [deg]	0.621 ± 0.046
Rb flux [atoms/s]	2.74e+10
Capture eff. [%]	40.8 ± 1.6
Dist Nozzle [cm]	6.248

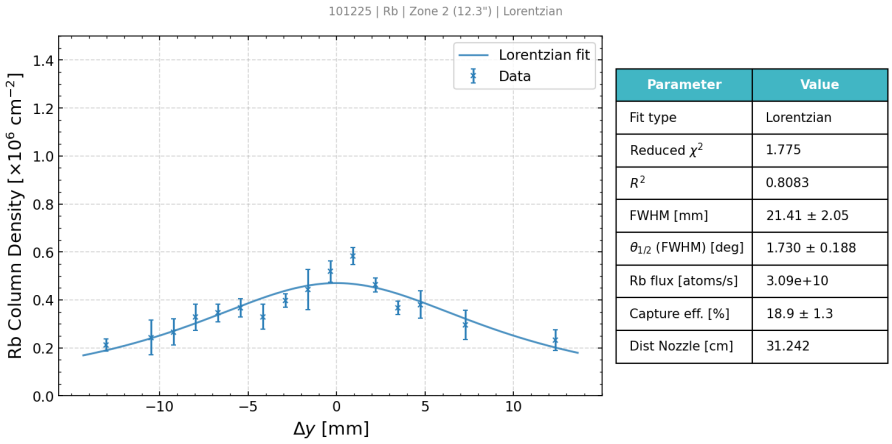
Figure 5.2: Zone 1 pure-Rb spatial profile fitted with a Lorentzian. The Lorentzian provides a substantially better reduced chi-squared at Zone 1. The origin of this improvement and its physical significance are discussed in Sec. 5.4.



Parameter	Value
Fit type	Gaussian
Reduced χ^2	2.175
R^2	0.7532
FWHM [mm]	23.42 ± 1.74
$\theta_{1/2}$ (FWHM) [deg]	1.914 ± 0.160
Rb flux [atoms/s]	3.17e+10
Capture eff. [%]	25.7 ± 1.4
Dist Nozzle [cm]	31.242

Figure 5.3: Zone 2 pure-Rb spatial profile fitted with a Gaussian. The Gaussian fit quality improves at the farther zone, consistent with the beam profile becoming more Gaussian-like as it propagates (Sec. 5.4).

Zone 2 Measurement: It is important to note that the two zones give significantly different divergence estimates when Method A is applied. From the Gaussian fits: $\theta_{1/2}^{(\mathrm{A,\ Gauss})} = 1.33°$ at Zone 1 vs. 1.91° at Zone 2. From the Lorentzian fits: $\theta_{1/2}^{(\mathrm{A,\ Lor})} = 0.62°$ vs. 1.73°.



Parameter	Value
Fit type	Lorentzian
Reduced χ^2	1.775
R^2	0.8083
FWHM [mm]	21.41 ± 2.05
$\theta_{1/2}$ (FWHM) [deg]	1.730 ± 0.188
Rb flux [atoms/s]	3.09e+10
Capture eff. [%]	18.9 ± 1.3
Dist Nozzle [cm]	31.242

Figure 5.4: Zone 2 pure-Rb spatial profile fitted with a Lorentzian. At Zone 2 the gap in fit quality between Lorentzian ($\chi^2_\nu = 1.78$) and Gaussian ($\chi^2_\nu = 2.18$) narrows compared to Zone 1, suggesting the two models may converge as the beam expands.

5.1.2 Method B: Two-Zone Differential

Method B (Eq. 4.13) uses the *growth* in beam width between two zones to extract the divergence angle, completely bypassing the need to use the poorly defined finite source size. Using the Gaussian FWHM values $w_1 = 5.44$ mm and $w_2 = 23.42$ mm, and $z_2 - z_1 = 312 - 62$ mm:

$$\theta_{1/2}^{(\mathrm{B,\ Gauss})} = 2.1^\circ. \tag{5.1}$$

Using the Lorentzian FWHMs $w_1 = 3.90$ mm and $w_2 = 21.41$ mm:

$$\theta_{1/2}^{(\mathrm{B,\ Lor})} = 2^\circ. \tag{5.2}$$

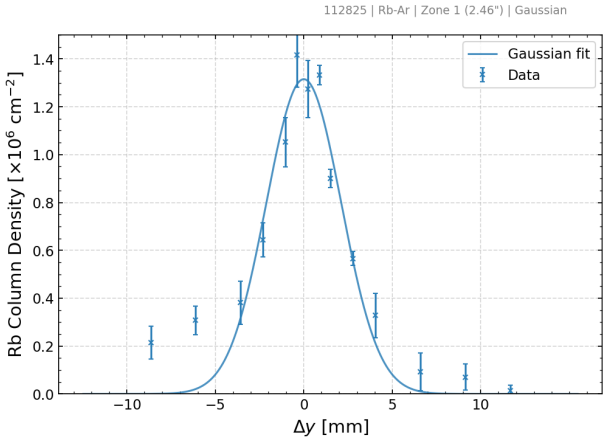
5.2 Beam Divergence: Dual-Species Rb-Ar Beam

For the dual-species Rb-Ar measurements, Ar was flowing at $\dot{q} \approx 0.01$ [SCCM]. Only Zone 1 data is available for this dataset, so only Method A is used. All individual per-position relative absorption fits as well as percent absorption fits used to rescale distribution for this dataset are shown in Appendix C, Sec. C.0.2.

The Zone 1 spatial profile $A(\Delta y)$ is shown in Figs. 5.5 and 5.6 for Gaussian and Lorentzian fits, respectively.

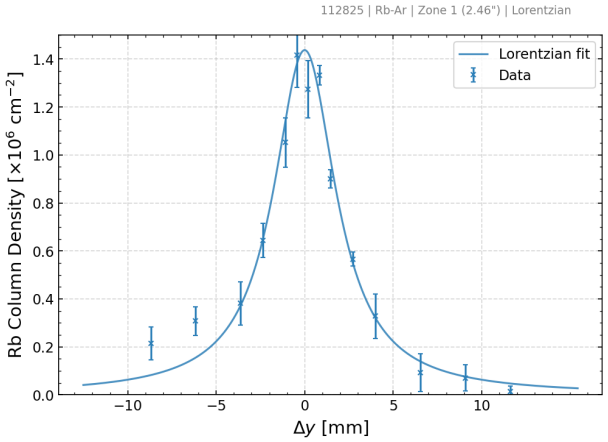
Comparing these results with the pure-Rb Zone 1 data, the Rb-Ar beam width is slightly narrower (FWHM $\approx$ 4.3-5.0 mm vs. 3.9-5.4 mm), and the estimated divergence is $\theta_{1/2} \approx 0.80^\circ$ (Lorentzian) and 1.12° (Gaussian).

Without a corresponding Zone 2, unfortunately, we cannot test what Method B be



Parameter	Value
Fit type	Gaussian
Reduced χ^2	5.513
R^2	0.9297
FWHM [mm]	4.99 ± 0.18
$\theta_{1/2}$ (FWHM) [deg]	1.122 ± 0.084
Rb flux [atoms/s]	2.46e+10
Capture eff. [%]	40.5 ± 2.2
Dist Nozzle [cm]	6.248
ρ_{Rb} [cm^{-3}]	1.47e+17

Figure 5.5: Rb-Ar dual-species beam spatial profile fitted with a Gaussian. $\chi^2_\nu \approx 5.5$ indicates a poor Gaussian fit to profile, consistent with the same behavior seen in the pure-Rb data.



Parameter	Value
Fit type	Lorentzian
Reduced χ^2	2.175
R^2	0.9716
FWHM [mm]	4.28 ± 0.22
$\theta_{1/2}$ (FWHM) [deg]	0.800 ± 0.100
Rb flux [atoms/s]	3.05e+10
Capture eff. [%]	34.7 ± 2.6
Dist Nozzle [cm]	6.248
ρ_{Rb} [cm^{-3}]	1.81e+17

Figure 5.6: Rb-Ar dual-species beam spatial profile fitted with a Lorentzian. As with the pure-Rb Zone 1 data, the Lorentzian fit quality is better than Gaussian.

would get, but based on results of Rb only, it is possible the divergences reported here for the Rb-Ar beam is an underestimate.

5.3 Discussion: Fit Model and Data Quality

Across all datasets, a Lorentzian provides a better reduced chi-squared than a Gaussian. Although, the two models become much more similar further away at Zone 2 (compare Figs. 5.1–5.2 with Figs. 5.3–5.4). It is not fully clear yet whether this Lorentzian is simply a better physical model or only an artifact of data analysis.

Senaratne et al. noted that the edges of the intensity distribution from their simulated capillaries have broad non-gaussian shoulders and tall central peak [17]. Whether this for sure means they are suggesting a Lorentzian profile is not clear. Additionally, it is again not clear how a large array of a triangularly bundled capillaries convolve the individual capillary profile. One possibility is a Lorentzian is a good approximation for the capillaries and near the nozzle itself but as we get further from the source, each capillary profile becomes more mixed and we recover a more gaussian profile. This would be consistent with the Zone 1 measurements getting a decently better fit with a Lorentzian, but Zone 2 measurements aren't significancy improved between a Lorentzian versus Gaussian.

It is also worth noting that the preference for Lorentzian could be partially or entirely a data-quality artifact. Some of the outermost data points in the translation stage sweeps appear to fit to noise rather than to a physical absorption signal (See Appendix. C, specifically sweep positions 700-900 for Rb-Ar), artificially inflating the profile tails and thus favoring the heavier-tailed Lorentzian. These data points are all taken automatically, so it includes when poor fits are made. It may be useful to improve fitting procedures to prevent fitting to noise, and see if a Lorentzian is still a better fit.

Furthermore, looking at Fig. 5.7 we see a physical image of our triangular microcapillary array superimposed on the spatial distribution with Gaussian fit for our Rb-Ar beam (conclusion is similar if you use the pure Rb beam distribution as well). The array is *not* to scale, but the direction it is orientated matches the direction of sweep and direction of Δy on plot.

Looking carefully at the nozzle, you will notice what appears to be a small space between the nozzle clamp and the modified CF flange (look at bottom versus top of clamp, visually different spacings relative to flange). Additionally, when looking at raw data in Appendix C (i.e. the 100 and 200 position), unlike the right hand side which I argued might be the result of fitting to noise, visually, these data points look much more like physical peaks, so this is likely the result of physical Rb being seen. One could

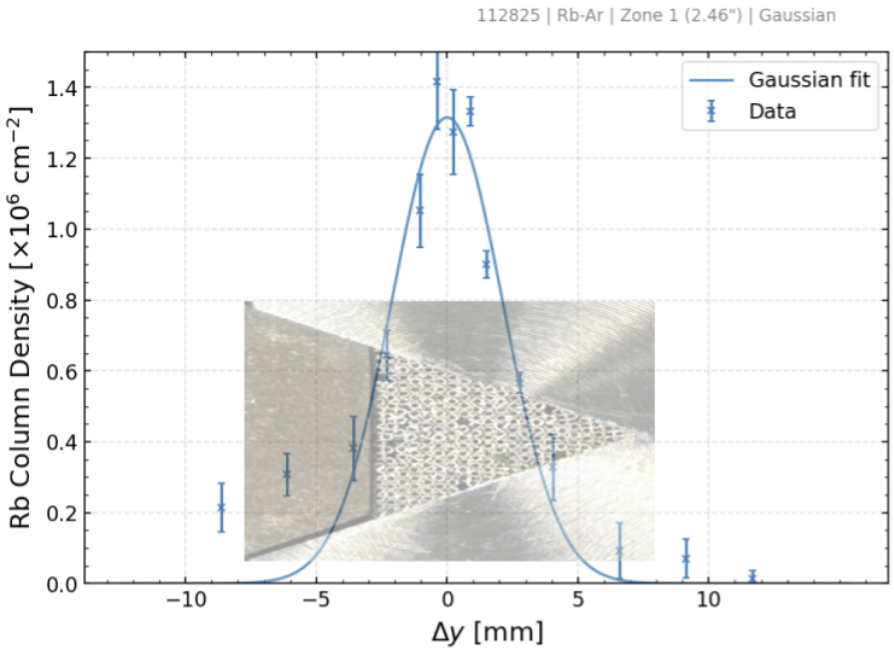


Figure 5.7: Triangular microcapillary array image superimposed on the Rb-Ar spatial absorption profile (Gaussian fit). The array orientation matches the periscope and probe beam sweep direction. A visible gap between the nozzle clamp and CF flange (bottom) could be consistent with Rb escaping outside the capillary array, potentially explaining the elevated left-side tail.

argue that this raised left hand side, may be the result of Rb also escaping through the small opening between the nozzle clamp and flange. An easy way we plan to test this, is to machine a copper gasket such that it covers everything except the capillaries. If this raised left side is from this slit, then it would disappear.

Considering both these possible explanations for why the right and left tail may be larger than expected, there is reason to believe the profile may not be a Lorentzian, and again the better fit could just be from these data and physical artifacts, but both modifications suggested above are needed to confirm this. Additionally, fixing these artifacts may show the divergence is less than expected, as both artifacts would make our distribution, especially when fitting with a gaussian, wider.

5.4 Discussion: Mean Free Path and Flow Regime

In Sec. 3.3.1 and 3.3.2 I discuss different regimes of operating the beam source in terms of the particles mean free, λ, path relative to the capillaries length, L_{cap}, and inner diameter ID_{cap}. When $\lambda \gg L_{\text{cap}}$ it is expected that divergence is defined by one of the definitions given in Eq. 3.3 or Eq. 3.4 [17, 20], which exact one for our given system is not fully

clear yet but discussed more below (Sec. 5.5). When $L_{\text{cap}} > \lambda > ID_{\text{cap}}$, some claim the divergence remains relatively unchanged from before [17], but others claim it begins decreasing [20].

When operating a pure Rb only beam, the Rb reservoir is heated to 100°C so we expect $P_{\text{Rb}} \approx 10^{-4}$ Torr (from characterization and as will be discussed below the actual P_{Rb} seems to be less than this due to lower flux than expected from expected vapor pressure). From Eq. 3.2 we expect $\lambda \approx 480$ mm, so much greater than $L_{\text{cap}} = 7.62$ mm, and in $\lambda \gg L_{\text{cap}}$ regime. With $\theta_{1/2} \approx 0.62 \pm 0.05°$ (Lorentzian) and $1.33 \pm 0.04°$ (Gaussian)–here I am only using Zone 1 measurement method A to directly compare to same measurement type with Rb-Ar beam.

When operating a Rb-Ar beam, the dominant pressure is now Argon. With $\dot{q}_{\text{Ar}} = 0.01$ SCCM, and back propagating with Eq. 3.20, 3.9, and 3.8, we get $\lambda \approx 2$ mm, still an order of magnitude greater than $ID_{\text{cap}} = 0.1$ mm. But now the beam is in the $L_{\text{cap}} > \lambda > ID_{\text{cap}}$ regime. With $\theta_{1/2} \approx 0.80 \pm 0.1°$ (Lorentzian) and $1.12 \pm 0.08°$ (Gaussian).

Depending on which fitting method used either regime can have a slightly higher or lower divergence than the other, so it is not clear whether or not operating in the $L_{\text{cap}} > \lambda > ID_{\text{cap}}$ regime has an impact of divergence. Regardless, it is clear that whatever effect being in the $L_{\text{cap}} > \lambda$ regime may have, at least up to

$$\lambda \gtrsim 20 \times ID_{\text{cap}}, \tag{5.3}$$

it is relatively insignificant as capture efficiency only varies between $\sim 35 - 40\%$, a rather negligible effect by the growth substrate. Considering there is no obvious difference so far, this suggests we should be able to push the Ar flow rate (and therefore λ) even closer to the ID_{cap}. To what extent this is true is still unknown, but something we intend to test.

5.5 Summary and Discussion of Results

Table 5.1 summarizes all key beam characterization results shown above for easy comparison of characterization methods and beam type.

First, it is good to notice that the Rb flux is fairly consistent between both methods used, zone of measurement, and different measurement times (over a month between Rb and Rb-Ar beam measurements). However, the flux measured is lower than expected. First, all these measurements were taken with the Rb reservoir valve fully open. In this case the conductance of the valve is significantly higher than the nozzle such that

Table 5.1: Beam Characterization Summary

Dataset	Method	Fit Model	χ^2_{red}	FWHM [mm]	$\theta_{1/2}$ [deg]	Capture Eff. [%]	Rb Flux [atoms/s]	Density [cm^{-3}]
Rb	A, Zone 1	Gaussian	7.8	5.4 ± 0.1	1.33 ± 0.04	35 ± 1	2.6×10^{10}	–
Rb	A, Zone 1	Lorentzian	2.5	3.9 ± 0.1	0.62 ± 0.05	41 ± 2	2.7×10^{10}	–
Rb	A, Zone 2	Gaussian	2.2	23 ± 2	1.9 ± 0.2	26 ± 1	3.2×10^{10}	–
Rb	A, Zone 2	Lorentzian	1.8	21 ± 2	1.7 ± 0.2	19 ± 1	3.1×10^{10}	–
Rb	B	Gaussian	–	–	2.1 ± 0.2	25 ± 2	–	–
Rb	B	Lorentzian	–	–	2 ± 0.2	18 ± 2	–	–
Rb-Ar	A, Zone 1	Gaussian	5.5	5.0 ± 0.2	1.1 ± 0.1	41 ± 2	2.5×10^{10}	1×10^{17}
Rb-Ar	A, Zone 1	Lorentzian	2.2	4.3 ± 0.2	0.8 ± 0.1	35 ± 3	3.0×10^{10}	2×10^{17}

at equilibrium Eq. 3.19 suggests the partial pressure of Rb in the mixing chamber is the same as that in the reservoir, so at 100°C we expect $P_{\text{Rb}} \approx 10^{-4}$ Torr. Using Eq. 3.9, but replacing molar mass with Avogadro constant gives us an expected Rb flux of $\Phi_{\text{Rb,expect}} \approx 5 \times 10^{12}$ atoms/s, about two orders of magnitude higher than being observed. Considering our probe beam is well below saturation, and the methods of Chapter. 4 seem reasonable, I am uncertain what is causing the discrepancy at this time. It is possible Rb is sticking to capillary walls, reservoir valve, or beam source more than expected. We have also opened the chamber a few times while Rb was actively inside. Despite taking precautions of filling chamber with Ar and sealing Rb reservoir, its possible much of the Rb got contaminated or expelled during this, making it harder to fill full beam source with desired vapor pressure. Additionally, Eq. 3.19 is a naive first order approximation.

Looking at divergences we see a very wide range of results from $\theta_{1/2} = 0.62°$ or 2.1°. Remember from Eq. 3.14 and3.15 we expect half angle divergences of $\theta_{1/2} \approx 0.75°$ or 1.26° respectively. The current inconclusive results do not appear to heavily favor one version over another. If we take the mean and standard deviation we get

$$\theta_{1/2}^{\text{ave}} = 1.4 \pm 0.6°, \tag{5.4}$$

which is consistent within error to both Eq. 3.14 and 3.15. Much more work and thought is needed to confirm which method is most accurate especially when considering possible issues discussed in Sec. 5.4

5.5.1 Example Crystal Growth

Its important to recall what the actual end goal is here as explained in Chapter 2. We hope to improve the Doped Cryogenic platform, to allow for a competitive electron electric dipole moment (eEDM) measurement, specifically, given the current characterized oven constraints, how long would it take to isolate 10^{13} dopants here. Let us assume we have the divergence from Eq. 5.4, giving a capture efficiency of $P_{\text{capt}} \approx 23 - 34\%$. Using the

lower capture efficiency with $\dot{q}_{\mathrm{Ar}} = 0.01$ SCCM and Eq. 3.21, we can expect a growth rate at growth substrate of $\dot{h}_{\mathrm{Ar}} \approx 2\ \mu$m/hr. With a dopant density of 10^{17} atoms/cm^3, and a growth and observation area of $A_{\mathrm{crystal}} = 4$ mm^2, it would take $t_{\mathrm{grow}} = 16$ hrs. Said another way, after just 16 hours of growth, we will have more spins that can be probed repeatedly, rather than thrown away after each trial (like in most current leading eEDM measurements), than ACME-II probed over 350 hours.

That being said, this only becomes competitive if we also improve T_2^* coherence times closer to a ms. However, as will be discussed in Chapter 6, even with no other sources of broadening, in order to have dipolar interaction limited coherence times down to the ms level, one needs to grow Rb at a density of $\rho_{\mathrm{ms}} \sim 10^{15}$ dopants/cm^3. This may require significantly more time to grow a crystal to get same number of spins to probe. But this current design is also expected to push to higher growth rates, possibly up to an order of magnitude higher, and in principle, one can also increase the crystal growth area up to tube diameter to grow an even larger crystal, both of which could allow us to still capture the number of spins desired in this short or shorter time scale.

Chapter 6

Spin-Spin Interaction Broadening: Monte Carlo Simulation

In this chapter I develop a Monte Carlo simulation of spin-spin interactions between dopants, modeled as spins generating magnetic fields resulting in a corresponding Zeeman shift. I compare both to an analytic result for an electron for verification and compare to experimental data of doped cryogenic crystals. Besides acting as a way to better understand coherence limitations in these crystals and try to better understand if broadening currently observed is predominantly dopant-dopant interactions or something else like dopant-crystal or dopant-impurity interactions, the results here would also give a near "fundamental" limit on coherence times and broadening as even if we grow perfect crystals, remove all impurities, and deal with any other stray inhomogeneous fields in our apparatus, dopants will still interact to some degree through these spin-spin interactions.

Additionally, while this simulation is currently setup to model how alkali dopants interact with each other, in principle slight modifications can be made to model how impurities or nuclear spins in certain crystal hosts (e.g. Neon-21) also interact with dopants and cause broadening.

It should also be noted, that this simulation was originally inspired by a similar model proposed in [14], which also simulates spin–spin interactions. However, my results differ from those reported there by roughly two orders of magnitude. While the source of this discrepancy has not yet been identified, the verification in Section 6.3, where my simulation agrees with an analogous analytic solution, gives me confidence in the results of this model. [1]

[1] Resolving this discrepancy is an important direction for future work, and I intend to investigate its origin further. Should this be resolved, an updated version of this manuscript will be made available. Remarks regarding this discrepancy are welcome at icross2@jh.edu

6.1 Spin-Spin Interaction Model

We consider a single atom at the origin and a chosen hyperfine transition

$$|F_{\mathrm{g}}, m_{F,\mathrm{g}}\rangle \rightarrow |F_{\mathrm{e}}, m_{F,\mathrm{e}}\rangle\,, \tag{6.1}$$

within a manifold defined by the electronic angular momentum J and nuclear spin I [48].

6.1.1 Transition frequency and Zeeman coefficient

For each hyperfine level F we use the standard hyperfine Landé g-factor [25],

$$g_F = g_J \frac{F(F+1) - I(I+1) + J(J+1)}{2F(F+1)}, \tag{6.2}$$

with $g_J \simeq 2.0023$ for the alkali ground state, $J = 1/2$, and where we drop the nuclear term as it corresponds to correction of order 0.1% [25]. The magnetic moment of a spin in state $|F, m_F\rangle$ oriented along $\hat{\mathbf{m}}$ is

$$\mathbf{m} = \mu_B g_F m_F \hat{\mathbf{m}}, \tag{6.3}$$

where μ_B is the Bohr magneton. Note, for this simulation the ground m_f state can not be zero, but excited state can be; therefore, for any broadening simulations involving $m_f = 0$, it must be "set" as an excited state, the results should be the same.

In the presence of a magnetic field B_z along the quantization axis, each hyperfine level experiences a first-order Zeeman energy shift

$$\Delta E_{|F,m_F\rangle} = \mu_B g_F m_F B_z. \tag{6.4}$$

The shift in the *transition* frequency between two states is

$$\Delta\nu = \frac{\Delta E_{|F_{\mathrm{e}},m_{F,\mathrm{e}}\rangle} - \Delta E_{|F_{\mathrm{g}},m_{F,\mathrm{g}}\rangle}}{h} = \gamma_{\mathrm{eff}}\, B_z, \tag{6.5}$$

where the effective Zeeman coefficient is

$$\gamma_{\mathrm{eff}} = \frac{\mu_B}{h}\Big(g_{F_{\mathrm{e}}} m_{F,\mathrm{e}} - g_{F_{\mathrm{g}}} m_{F,\mathrm{g}}\Big). \tag{6.6}$$

Any local magnetic field B_z at the test atom therefore shifts its transition frequency by $\Delta\nu = \gamma_{\mathrm{eff}} B_z$.

6.1.2 Dipole magnetic field

Each neighboring dopant is modeled as a point magnetic dipole. For a dipole with moment $\mathbf{m}$ located at position $\mathbf{r}$ relative to the origin, the magnetic field at the origin is [49]

$$\mathbf{B}(\mathbf{r}, \mathbf{m}) = \frac{\mu_0}{4\pi r^3}\Big[3(\mathbf{m} \cdot \hat{\mathbf{r}})\hat{\mathbf{r}} - \mathbf{m}\Big], \tag{6.7}$$

where μ_0 is the permeability of free space, $r = |\mathbf{r}|$, and $\hat{\mathbf{r}} = \mathbf{r}/r$. This is the standard free-space dipole field (embedding in a crystal matrix is not accounted for at this level of the model).

6.2 Monte Carlo Method

6.2.1 Sampling dopant configurations

We model a single "test cell" as a cube of side length L containing a Poisson-distributed number of dopants at density ρ (in atoms/cm^3). The mean number of dopants in the volume is

$$\bar{N} = \rho L^3. \tag{6.8}$$

For each Monte Carlo run we draw

$$N_{\text{neighbors}} \sim \text{Poisson}(\bar{N}) - 1, \tag{6.9}$$

where the -1 accounts for the central test atom fixed at the origin. The $N_{\text{neighbors}}$ dopants are placed at random positions uniformly distributed in the cube,

$$\begin{aligned} \mathbf{r}_i = (x_i, y_i, z_i) \sim \text{Uniform}\Big[-\frac{L}{2}, \frac{L}{2}\Big]^3, \\ i = 1, \ldots, N_{\text{neighbors}}. \end{aligned} \tag{6.10}$$

An example realization of such a configuration is shown in Fig. 6.1.

6.2.2 Assigning spin states and orientations

Each neighbor dopant i is assigned a hyperfine manifold and Zeeman state using simple "pumping-efficiency" parameters that roughly mimics optical pumping into a desired state $|F_{\text{pump}}, m_{F,\text{pump}}\rangle = |F_{\text{g}}, m_{F,\text{g}}\rangle$. We define:

- p_F: probability of being pumped into the desired hyperfine level F_{g};

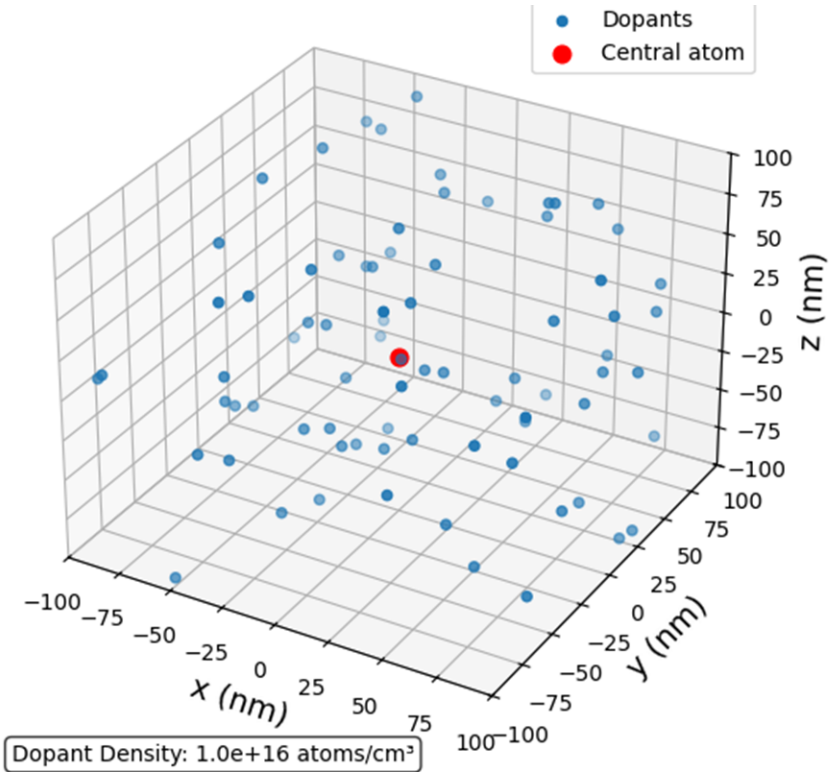


Figure 6.1: Example Monte Carlo realization of a dopant configuration. The central test dopant is fixed at the origin, while all other dopants are placed randomly and uniformly in a cubic volume of side L at target density ρ. For each realization, the dipole magnetic field from all neighbors is summed at the origin and converted to a hyperfine transition frequency shift of the central test dopant.

- p_{m_F}: probability of being pumped into the desired sublevel $m_{F,\mathrm{g}}$ within that manifold;
- p_{align}: probability that the magnetic moment is aligned to the quantization axis $\hat{z}$.

For each neighbor we sample

$$F_i = \begin{cases} F_{\mathrm{g}}, & \text{with probability } p_F, \\ F_{\mathrm{e}}, & \text{with probability } 1 - p_F, \end{cases} \tag{6.11}$$

$$m_{F,i} = \begin{cases} m_{F,\mathrm{g}}, & \text{with probability } p_{m_F}, \\ \text{uniform in } \{-F_{\mathrm{g}}, \ldots, +F_{\mathrm{g}}\}, & \text{otherwise}, \end{cases} \tag{6.12}$$

and for the orientation

$$\hat{\mathbf{m}}_i = \begin{cases} \hat{z}, & \text{with probability } p_{\text{align}}, \\ \text{random unit vector on } S^2, & \text{with probability } 1 - p_{\text{align}}. \end{cases} \tag{6.13}$$

The full magnetic moment vector of neighbor i is then $\mathbf{m}_i = \mu_B g_{F_i} m_{F,i} \hat{\mathbf{m}}_i$.

In practice, the results turn out to be relatively insensitive to the exact pumping efficiencies. Changing p_{m_F} can shift T_2^* by up to a factor of ~ 2, while p_F and p_{align} have even smaller effects. The dominant control on the predicted linewidth is the dopant density ρ and the choice of transition.

6.2.3 Computing the field and frequency shift

For each Monte Carlo trial k, we compute the magnetic field at the origin due to all $N_{\text{neighbors}}$ neighbor dipoles using Eq. (6.7), noting that the field from a dipole at position $\mathbf{r}_i^{(\text{dopant})}$ evaluated at the origin requires the displacement vector from dipole to field point, $\mathbf{r}_i = -\mathbf{r}_i^{(\text{dopant})}$. We project onto the quantization axis and sum,

$$B_z^{(k)} = \hat{z} \cdot \sum_{i=1}^{N_{\text{neighbors}}} \mathbf{B}(\mathbf{r}_i, \mathbf{m}_i), \tag{6.14}$$

and convert to a frequency shift

$$\Delta\nu_k = \gamma_{\text{eff}} B_z^{(k)}, \tag{6.15}$$

using Eq. (6.6).

6.2.4 Extracting the linewidth and T_2^*

Repeating the above over $N_{\text{MC}} \sim 10^5$ independent trials generates a distribution of frequency shifts $\{\Delta\nu_k\}$. We construct a histogram $H(\Delta\nu)$ from these samples (Fig. 6.2) and fit it to a Lorentzian,

$$L(\nu) = A \, \frac{\Gamma/2}{(\nu - \nu_0)^2 + (\Gamma/2)^2}, \tag{6.16}$$

where Γ is the full-width at half-maximum (FWHM). The fitted FWHM is then converted to an inhomogeneous coherence time via

$$T_2^* = \frac{1}{\pi\Gamma}. \tag{6.17}$$

Equation (6.17) is the standard relation between a Lorentzian FWHM and the corresponding exponential decay time.

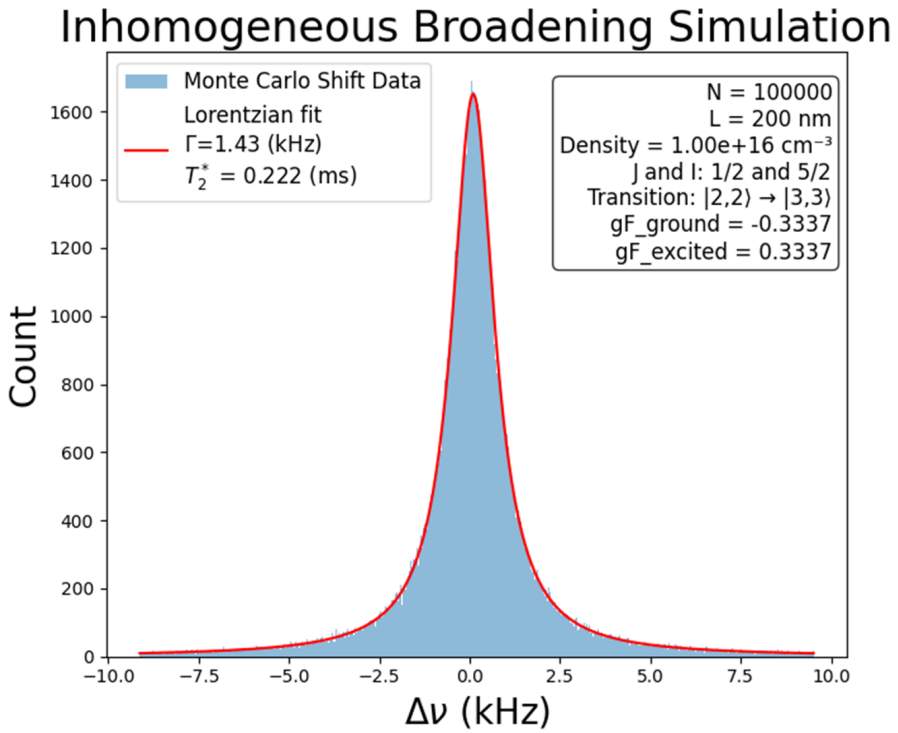


Figure 6.2: Example histogram $H(\Delta\nu)$ of Monte Carlo frequency shifts. Each bin counts how often a given shift $\Delta\nu$ appears over many random configurations of neighboring dopants. The histogram is fit to a Lorentzian (Eq. (6.16)) to extract an effective inhomogeneous linewidth Γ, which is then mapped to a coherence time $T_2^* = 1/(\pi\Gamma)$.

Overall, this simulation takes as inputs the density ρ, box size L, transition quantum numbers, and pumping/alignment efficiencies $\rightarrow$ generates N_{MC} independent configurations $\rightarrow$ computes the set of $\Delta\nu_k$ $\rightarrow$ performs the Lorentzian fit $\rightarrow$ extracts Γ and T_2^*.The full Python implementation is given in Appendix D.

6.3 Verifying Simulation Against Analytic Estimate

Kittel and Abrahams give an analytic estimate for dipolar broadening of magnetic resonance lines in magnetically dilute crystals [50]. Upadhyay applies this result to

alkali-doped cryogenic crystals, specifically rubidium in solid parahydrogen [13]. I show the analytic result here in a form appropriate for an argon host lattice, then compare it to Monte Carlo simulation results to verify my simulation.

Dipolar-limited broadening in the dilute limit produces a Lorentzian lineshape whose FWHM is given by [13, 50]

$$\mathrm{FWHM} = \frac{\mu_0}{4\pi} \times 10.6 \times f \times g_s \frac{\mu_B^2}{h a^3}, \tag{6.18}$$

where $g_s \approx 2$ is the electron g-factor, h is Planck's constant, $f = \rho_{\mathrm{dopant}}/\rho_{\mathrm{host}}$ is the fractional dopant concentration, and a is the host lattice constant. For an FCC lattice such as solid argon, each conventional unit cell contains 4 atoms [51], so

$$\rho_{\mathrm{Ar}} = \frac{4}{a_{\mathrm{Ar}}^3}. \tag{6.19}$$

Substituting $f = \rho_{\mathrm{dopant}}/\rho_{\mathrm{Ar}}$ into Eq. 6.18, the lattice constant cancels and one obtains a broadening relationship expressed directly in terms of absolute dopant density,

$$\mathrm{FWHM} = \frac{\mu_0}{4\pi} \times \frac{10.6}{4} \times \rho_{\mathrm{dopant}} \times g_s \frac{\mu_B^2}{h}. \tag{6.20}$$

6.3.1 Comparing Simulation to Analytic Estimate

The Kittel-Abrahams result treats neighboring spins as bare electrons. To model neutral alkali dopants, we replace the electron g-factor with the hyperfine Landé g-factor g_F, following Upadhyay [13]. I compare against the ^{85}Rb transition

$$|F_{\mathrm{g}} = 3,\, m_{F,\mathrm{g}} = -1\rangle \rightarrow |F_{\mathrm{e}} = 3,\, m_{F,\mathrm{e}} = 0\rangle\,,$$

for which $g_s \rightarrow g_F \approx 1/3$, and all pumping and alignment efficiency parameters are set to 1.0.

Figure 6.3 shows the Monte Carlo simulation results alongside the analytic prediction of Eq. 6.20. The two agree to within a factor of ~ 2 across the full density range tested, and both exhibit a $T_2^* \propto 1/\rho_{\mathrm{dopant}}$ scaling.

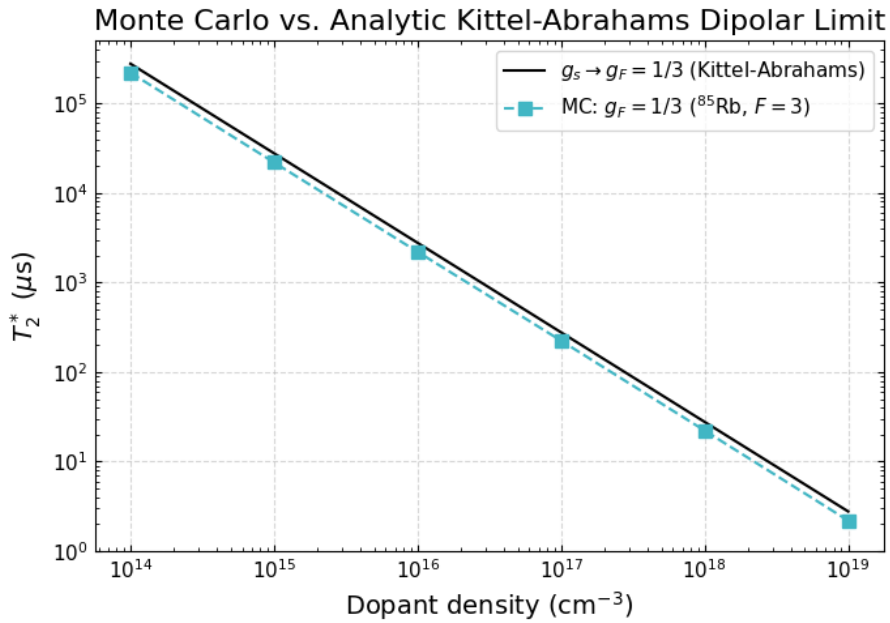


Figure 6.3: Monte Carlo simulated T_2^* versus dopant density (blue squares) compared to the Kittel-Abrahams analytic dipolar limit (black line), evaluated for the ^{85}Rb transition $|F = 3, m_F = -1\rangle \to |F = 3, m_F = 0\rangle$ with $g_F = 1/3$. Both curves follow $T_2^* \propto 1/\rho_{\text{dopant}}$ scaling, and agree to within a factor of ~ 2 across five orders of magnitude of density.

6.4 Results

6.4.1 Sensitivity to simulation parameters

Figure 6.4 shows how varying the pumping and alignment efficiencies defined in Sec. 6.2 affects T_2^*, with all other efficiencies held at 1.0 while varying each one individually. In general, changing these parameters has only a modest effect on T_2^*. The only significant change is that decreasing p_{m_F} can increase the coherence time by up to a factor of ~ 2. This relative insensitivity justifies treating the pumping efficiencies as secondary parameters; the dominant control on the predicted linewidth is the dopant density and the choice of transition.

6.4.2 Comparison to experimental data

To see where the dipolar model works and where it fails, I compare its predictions to several experimental systems where both the dopant density and an inhomogeneous linewidth or T_2^* have been reported. These comparisons divided into two regimes:

- a "high-density" regime, where dopant densities are $\rho \gtrsim 10^{17}$ atoms/cm^3;

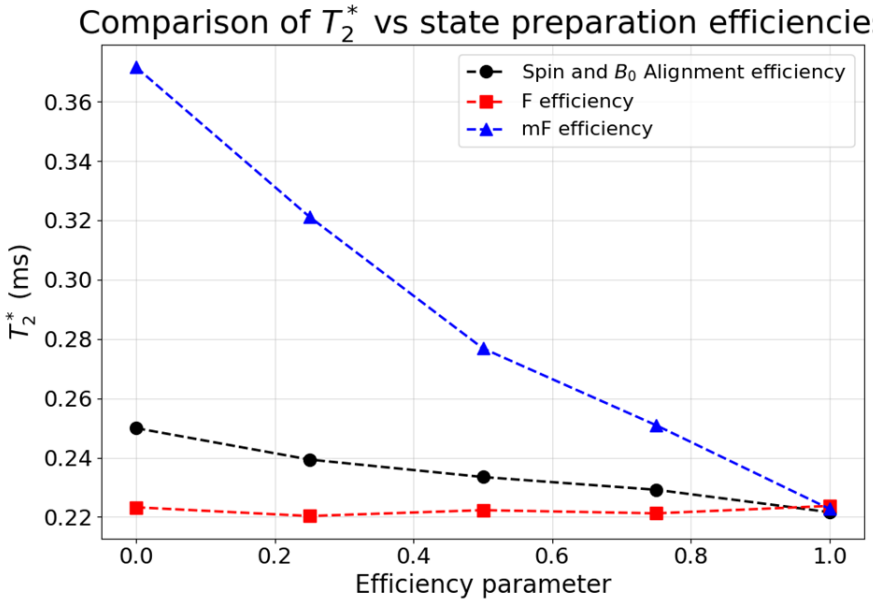


Figure 6.4: Dependence of the simulated T_2^* on the three pumping and alignment efficiency parameters (p_F, p_{m_F}, p_{align}) for ^{85}Rb at fixed density. All other efficiencies are held at 1.0 while each is varied individually. The result is relatively insensitive to all three, with p_{m_F} producing the largest effect at up to a factor of ~ 2.

- a "low-density" regime, with $\rho \lesssim 10^{16}$ atoms/cm^3.

The high-density regime turns out to be reasonably predicted using the dipole-dipole interaction broadening model, at least to within an order of magnitude. At low densities, however, the model fails, predicting linewidths at least two orders of magnitude smaller than what is observed. This suggests that in most existing doped rare-gas crystals, dipole-dipole interactions are alone *not* the main source of inhomogeneous broadening.

High dopant densities: solid parahydrogen As a high-density test case, I use the data from Upadhyay *et al.* [11], who reports the linewidths for several neighboring m_F transitions within the $F = 3$ ground-state manifold of ^{85}Rb embedded in solid parahydrogen. They report that changing the dopant density does not significantly affect the linewidth until a certain upper density limit is reached of $\rho \sim 10^{18}$ atoms/cm^3 , beyond which the broadening becomes noticeably worse. I take this "limit" density as the input for testing the Monte Carlo model. Fig. 6.5 compares my simulated results against the experimentally reported values. The model reproduces the overall scale and relative ordering of linewidths to within an order of magnitude

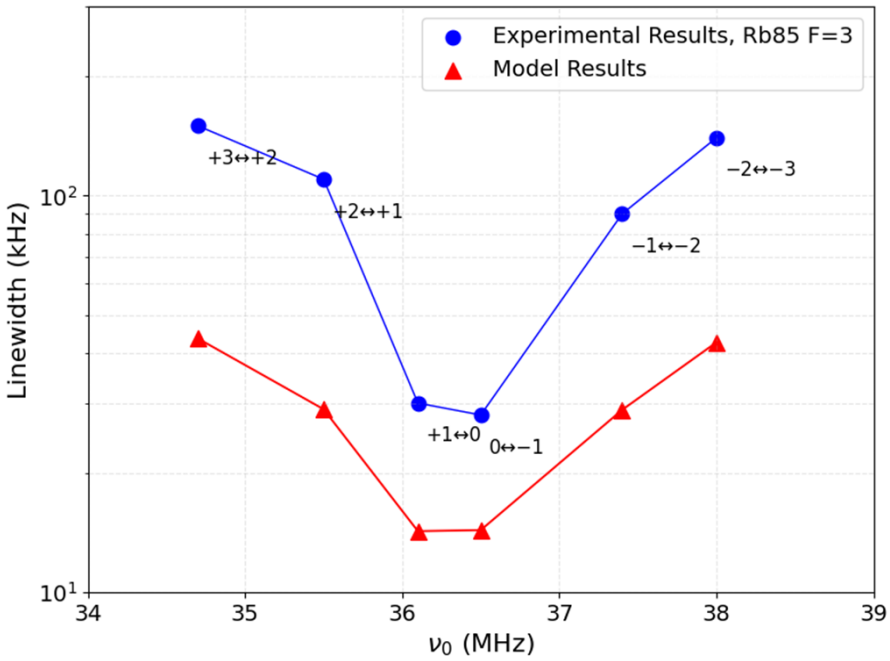


Figure 6.5: Simulated versus experimental inhomogeneous broadening for several neighboring m_F transitions within the $F = 3$ ground-state manifold of ^{85}Rb in solid parahydrogen, using values reported in Ref. [11].

Low dopant densities: Rb:Ne and Na:Ne The situation looks very different at lower dopant densities. Two examples are Rb in solid neon and Na in solid neon.

Dargyte *et al.* study ^{85}Rb in solid neon at densities around $\rho \sim 10^{16}\,\text{atoms/cm}^3$ and report linewidths for several neighboring m_F transitions within the $F = 3$ ground-state manifold [10]. Using their densities and transitions as inputs to the Monte Carlo model, I obtain dipole-dipole-limited linewidths that are almost two orders of magnitude smaller than the experimental values. The comparison is summarized in Fig. 6.6.

This discrepancy is even more striking when we note that the Rb:Ne linewidths at $\rho \sim 10^{16}\,\text{atoms/cm}^3$ are comparable to the Rb:parahydrogen linewidths at densities roughly two orders of magnitude higher. If dipole-dipole interactions were the dominant broadening mechanism in both systems, we would expect a strong density dependence across these experiments, which is not observed.

Na-doped neon crystals grown at a density of roughly $\rho \sim 3 \times 10^{16}\,\text{atoms/cm}^3$ are probed on the hyperfine transition $|F = 1, m_F = 1\rangle \rightarrow |F = 2, m_F = 2\rangle$ in ^{23}Na [14]. The reported inhomogeneous linewidth for this transition is about 989 kHz. Running my Monte Carlo dipolar model at the same density and for the same transition [52], I obtain a simulated linewidth of only 2.29 kHz — more than two orders of magnitude lower. The simulation broadening is shown in Fig. 6.7.

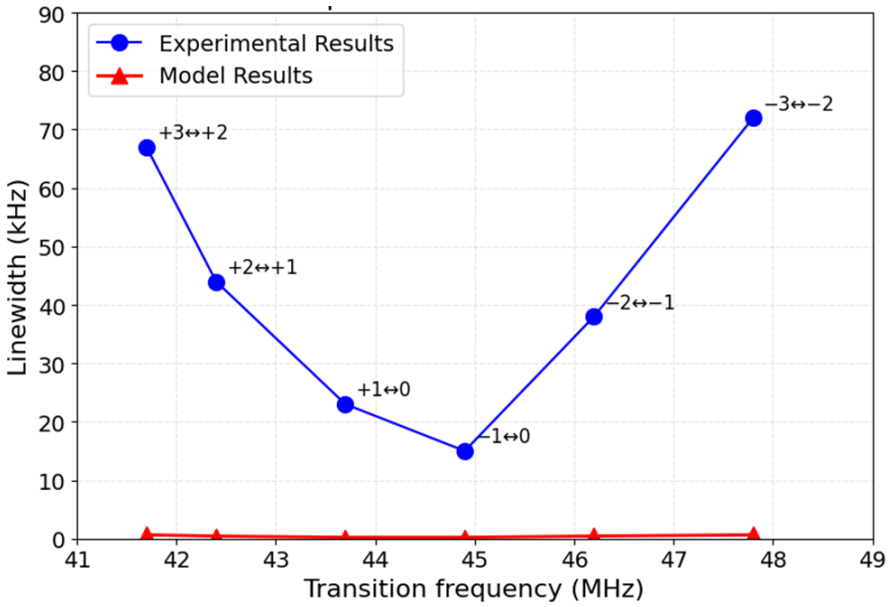


Figure 6.6: Comparison between experimental inhomogeneous linewidths for ^{85}Rb in solid neon at densities $\rho \sim 10^{16}$ atoms/cm^3 [10] and the dipole-dipole-limited values predicted by the Monte Carlo model. At these "low" densities, the simulated broadening is nearly two orders of magnitude smaller than observed.

6.5 Discussion and Limitations

6.5.1 Implications for the dominant broadening mechanism

Taken together, these comparisons suggest that:

- At very high dopant densities, the dipole-dipole broadening model predicts linewidths that are comparable (within an order of magnitude) to experiment. In this regime, it is plausible that dipole-dipole interactions are a main source of inhomogeneous broadening.
- At lower dopant densities, the same model predicts linewidths that are much smaller than observed, often by factors of 100 or more. Here, something other than dipole-dipole interactions between dopants is likely dominating the inhomogeneous broadening.

The near insensitivity of measured linewidths to dopant density across different hosts and densities, combined with the large discrepancy between simulated and observed linewidths at low ρ, supports the belief that structural disorder and multiple trapping sites in the crystal are the main culprits for the short T_2^* observed.

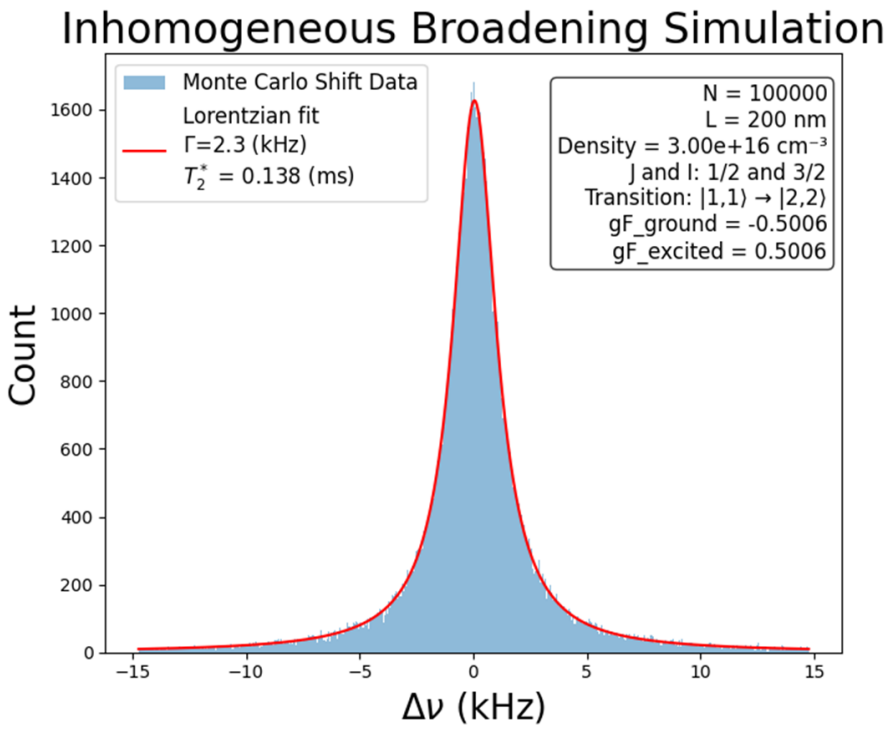


Figure 6.7: Dipole-dipole inhomogeneous broadening model for the $|F = 1, m_F = 1\rangle \rightarrow |F = 2, m_F = 2\rangle$ microwave transition of ^{23}Na in solid neon at a dopant density of $\rho \sim 3 \times 10^{16}\,\text{atoms/cm}^3$ [14]. The experimental inhomogeneous linewidth is approximately 980 kHz, whereas the model predicts only about 2.29 kHz, more than two orders of magnitude lower.

6.5.2 Consequences for growing Rb doped-crystals

Optimistically, if the broadening is structural in origin, then it is improvable with better growth techniques. This is exactly the direction being pursued in the Odom lab at Northwestern. By understanding and controlling growth conditions, trapping sites, and strain in the host crystal, it should be possible to systematically reduce this structural inhomogeneity and push T_2^* much closer to T_2. Importantly, the dipole-dipole interaction mode results here suggest that if crystal defects and site disorder can be significantly reduced, densities on the order of

$$\rho_{\text{ms}} \sim 10^{15}\text{atoms/cm}^3, \tag{6.21}$$

would be sufficient to keep the dipolar-limited T_2^* in the millisecond regime, as shown in Fig. 6.3.

6.5.3 Model limitations

This treatment of spin-state preparation and moment orientation is fairly crude. In a real experiment these variables are correlated and changing one can influence the others. However, for the order-of-magnitude estimates presented here, this simple model is sufficient. Regardless, the model is useful in providing a lower bound on inhomogeneous broadening (equivalently, an upper bound on T_2^*) that one could expect with improved crystal quality.

References

[1] A. C. Vutha, M. Horbatsch, and E. A. Hessels, "Oriented polar molecules in a solid inert-gas matrix: a proposed method for measuring the electric dipole moment of the electron", Atoms **6**, 3 (2018).

[2] C. Braggio, R. Calabrese, G. Carugno, G. Fiscelli, M. Guarise, A. Khanbekyan, A. Noto, R. Passante, L. Rizzuto, G. Ruoso, and L. Tomassetti, "Spectroscopy of alkali atoms in solid matrices of rare gases: experimental results and theoretical analysis", arXiv preprint, arXiv:2105.05276 (2022).

[3] A. N. Kanagin, N. de Zordo, A. Angerer, W. Kersten, N. Lagos, J. Schmiedmayer, and E. S. Redchenko, "Impurities in cryogenic solids: a new platform for hybrid quantum systems", arXiv preprint, arXiv:2508.21651 (2025).

[4] L. C. Balling and J. J. Wright, "Laser excitation of excited states of Rb and Cs atoms in an Ar matrix", The Journal of Chemical Physics **78**, 592 (1983).

[5] D. M. Lancaster, U. Dargyte, S. Upadhyay, and J. D. Weinstein, "Radiative properties of rubidium atoms trapped in solid neon and parahydrogen", Phys. Rev. A **103**, 052614 (2021).

[6] A. N. Kanagin, S. K. Regmi, P. Pathak, and J. D. Weinstein, "Optical pumping of rubidium atoms frozen in solid argon", Physical Review A **88**, 063404 (2013).

[7] ACME Collaboration, "Improved limit on the electric dipole moment of the electron", Nature **562**, 355 (2018).

[8] T. S. Roussy, L. Caldwell, T. Wright, W. B. Cairncross, Y. Shagam, K. B. Ng, N. Schlossberger, S. Y. Park, A. Wang, J. Ye, and E. A. Cornell, "An improved bound on the electron's electric dipole moment", Science **381**, 46 (2023).

[9] S. I. Kanorsky, S. Lang, S. Lücke, S. B. Ross, T. W. Hänsch, and A. Weis, "Millihertz magnetic resonance spectroscopy of cs atoms in body-centered-cubic ^{4}He", Phys. Rev. A **54**, R1010 (1996).

[10] U. Dargyte, D. M. Lancaster, and J. D. Weinstein, "Optical and spin-coherence properties of rubidium atoms trapped in solid neon", Physical Review A **104**, 032611 (2021).

[11] S. Upadhyay, U. Dargyte, V. D. Dergachev, R. P. Prater, S. A. Varganov, T. V. Tscherbul, D. Patterson, and J. D. Weinstein, "Spin coherence and optical properties of alkali-metal atoms in solid parahydrogen", Physical Review A **100**, 063419 (2019).

[12] G. Gabrielse, *Physics 480: advanced topics in amo physics — lecture notes*, Course notes, Northwestern University, Fall 2025, unpublished, 2025.

[13] S. Upadhyay, "Spin coherence of alkali-metal atoms in cryogenic solid matrices", Ph.D. dissertation (University of Nevada, Reno, 2020).

[14] A. N. Kanagin, "Coupling in quantum solids: from atoms towards molecules", PhD thesis (Technische Universität Wien, Vienna, Austria, 2025).

[15] O. G. Peterson, *Lattice constant, thermal expansion, and isothermal compressibility measurements on argon single crystals.* (University of Illinois at Urbana-Champaign, 1965).

[16] S. K. Regmi, "Optical Pumping of Rubidium Spin in a Solid Argon Matrix", MA thesis (University of Nevada, Reno, Jan. 2013).

[17] R. Senaratne, S. V. Rajagopal, Z. A. Geiger, K. M. Fujiwara, V. Lebedev, and D. M. Weld, "Effusive atomic oven nozzle design using an aligned microcapillary array", Review of Scientific Instruments **86**, 023105 (2015).

[18] M. Francois and W. Shyy, "Micro-scale drop dynamics for heat transfer enhancement", Progress in Aerospace Sciences **38**, 275 (2002).

[19] J. H. Moore, C. C. Davis, M. A. Coplan, and S. C. Greer, *Building scientific apparatus*, 4th ed. (Cambridge University Press, 2009).

[20] K. J. Ross and B. Sonntag, "High temperature metal atom beam sources", Review of Scientific Instruments **66**, 4409 (1995).

[21] R. H. Beaumont, H. Chihara, and J. A. Morrison, "Thermodynamic properties of krypton: vibrational and other properties of solid argon and solid krypton", Proceedings of the Physical Society **78**, 1462 (1961).

[22] MicroGroup, *304H33RW hypodermic tubing, 33 RW gauge, 304 stainless steel, 5 ft*, `https://www.microgroup.com/product/304h33rw/`, Nom. OD: 0.008 in, Nom. ID: 0.004 in, Nom. Wall: 0.002 in. Accessed: April 27, 2026, 2026.

[23] Kurt J. Lesker Company, *DFF275X000 — Flange, UHV, SS, Double-Sided, Blank, 2.75" CF*, https://www.lesker.com/flanges/flanges-cf-doublefaced/part/dff275x000, 304L stainless steel, DN35CF–DN40CF (2.75" OD), blank bore, double-faced ConFlat® flange. Accessed: 2026-04-30, 2026.

[24] Northwestern University Research Shop, *Research shop — professional machine shop services*, https://researchshop.facilities.northwestern.edu/, Fabrication services provided by Robert Golenia and Thang Bui. Accessed: 2026-04-30, Technological Institute, Room NG46, 2145 Sheridan Rd, Evanston, IL 60208, 2026.

[25] D. A. Steck, *Rubidium 85 D Line Data*, available online at https://steck.us/alkalidata, revision 2.3.4, 8 August 2025, 2025.

[26] D. A. Steck, *Rubidium 87 D Line Data*, available online at https://steck.us/alkalidata, revision 2.3.4, 8 August 2025, 2025.

[27] MDC Precision, *Uhv leak valve (part no. uhv-133)*, Accessed: 2026-04-27, 2026.

[28] LDS Vacuum Products, Inc., *1.33" od conflat flexible metal hose (bellows), 3.20" oal (part no. 133-f)*, Product specification page, accessed April 27, 2026, 2026.

[29] Sigma-Aldrich, *Rubidium ingot, 99.6% (trace metals basis), product no. 276332-1g*, CAS: 7440-17-7; packaged in break-seal ampule under inert gas; accessed 2026-05-01, n.d.

[30] Sigma-Aldrich, *Certificate of analysis for rubidium (rb)*, tech. rep. Product 276332, Batch MKCS4993, Quality release date: 28 Nov 2022; purity 99.6% (trace metals basis) (Sigma-Aldrich, St. Louis, MO, USA, 2022).

[31] McMaster-Carr, *Easy-form nickel chromium alloy wire (part no. 8880k77)*, Accessed: 2026-05-01, n.d.

[32] McMaster-Carr, *Mica/silicone insulating sheet (part no. 85955k112)*, Accessed: 2026-05-01, n.d.

[33] McMaster-Carr, *High-temperature noninsulated butt splice connector (part no. 7971k41)*, Accessed: 2026-05-01, n.d.

[34] McMaster-Carr, *Vibration-resistant 316 stainless steel worm-drive hose clamp (part no. 5682k15)*, Accessed: 2026-05-01, n.d.

[35] Alicat Scientific, *M series mass flow controllers and meters specifications*, Accessed: 2026-04-29 (n.d.).

[36] Airgas USA, LLC, *Uhp grade argon, size 300 high pressure steel cylinder, cga 580 (part #ar uhp300)*, 336 CF, DOT 3AA-2400, Ultra High Purity Grade.

[37] Airgas USA, LLC, *Safety data sheet: argon, compressed (sds #001004)*, Version 7.05. CAS #7440-37-1, Mar. 2025.

[38] J. L. Dye, *Rubidium*, Encyclopædia Britannica, Accessed: April 29, 2026.

[39] Stanford Research Systems, *Models rga100, rga200, and rga300 residual gas analyzer operating manual and programming reference*, Accessed: 2026-05-01, Stanford Research Systems (1996).

[40] TOPTICA Photonics AG, *Dl pro tunable external cavity diode laser*, Accessed: 2026-05-01, TOPTICA Photonics AG (n.d.).

[41] TOPTICA Photonics AG, *Digilock 110 feedback controller manual for sys dc 110 rack*, Accessed: 2026-05-01, TOPTICA Photonics AG (2023).

[42] R. Paschotta, *Effective mode area*, RP Photonics Encyclopedia, Accessed: 2026-04-28.

[43] Thorlabs Scientific Imaging, *DCx camera functional description and SDK manual*, Version 4.82 (July 2018).

[44] Thorlabs, *PDA36A operating manual: switchable gain, amplified silicon detector*, Document No. 13053-S01 (Newton, NJ).

[45] C. J. Foot, *Atomic physics*, Oxford master series in atomic, optical, and laser physics (Oxford University Press, Oxford, 2007).

[46] Electronics Tutorials, *Active filter tutorial*, https://www.electronics-tutorials.ws/filter/filter_3.html, Accessed: 2026-04-29.

[47] SciPy Developers, *`scipy.optimize.curve_fit` — SciPy reference guide*, Accessed: 2026-04-29, 2024.

[48] J. S. Townsend, *A modern approach to quantum mechanics*, 2nd ed. (University Science Books, Sausalito, CA, 2012).

[49] D. J. Griffiths, *Introduction to electrodynamics*, 5th ed. (Cambridge University Press, Cambridge, 2023).

[50] C. Kittel and E. Abrahams, "Dipolar broadening of magnetic resonance lines in magnetically diluted crystals", Phys. Rev. **90**, 238 (1953).

[51] Y. Wang, A. K. Vallabhaneni, B. Qiu, and X. Ruan, "Phonon spectral energy density analysis of solids: the k point reduction in the first Brillouin zone of FCC crystals and a case study on solid argon", Nanoscale and Microscale Thermophysical Engineering **18**, 155 (2014).

[52] D. A. Steck, *Sodium D Line Data*, available online at https://steck.us/alkalidata, revision 2.3.4, 8 August 2025, 2025.

Appendix A

Cad Drawings

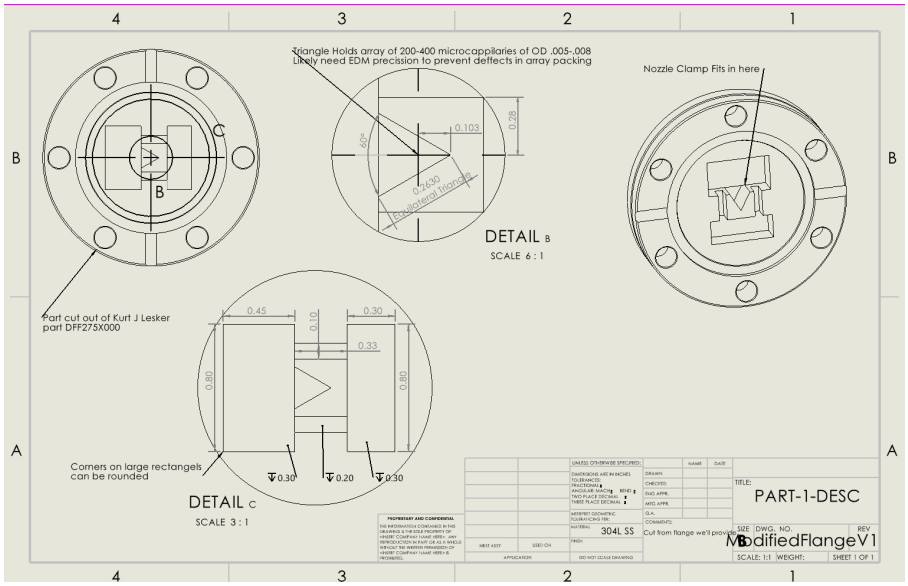


Figure A.1: Sketch of modified 2.75" CF flange. Cut to fit triangular array of microcapillaries as discussed in Sec. 3.3

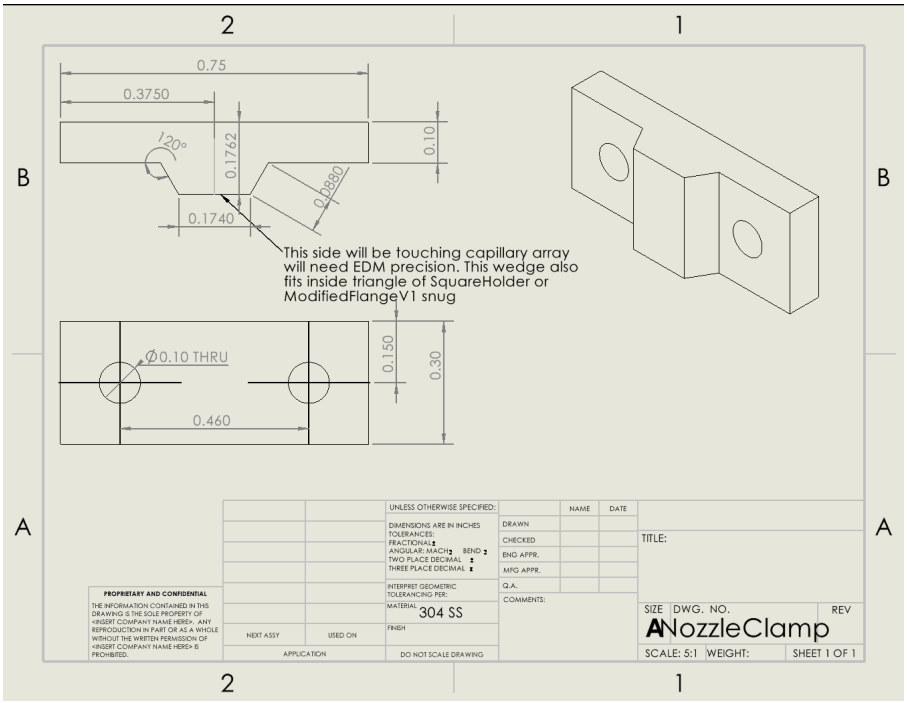


Figure A.2: Sketch of clamp to pressure fit microcapillary array into modified flange in Fig. A.1. Discussed in Sec. 3.3

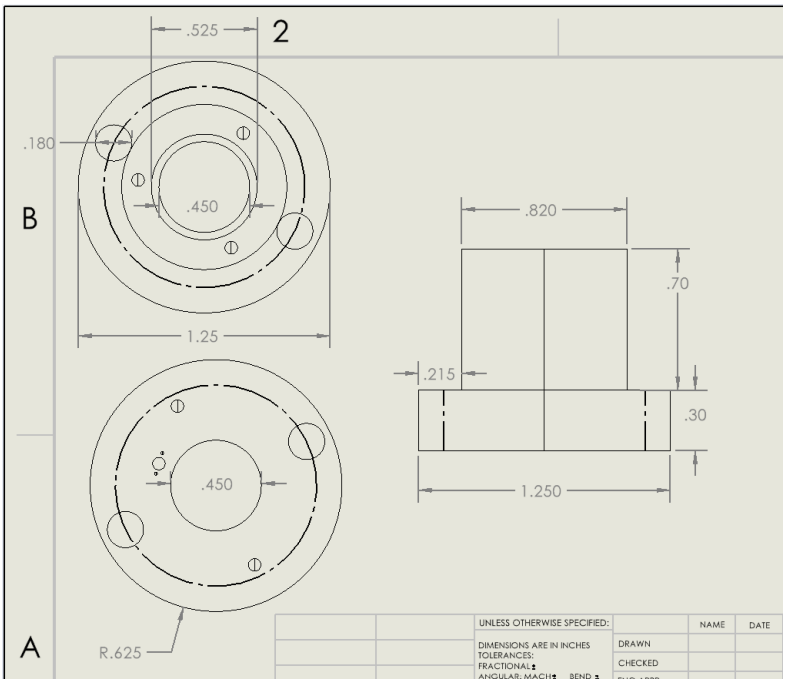
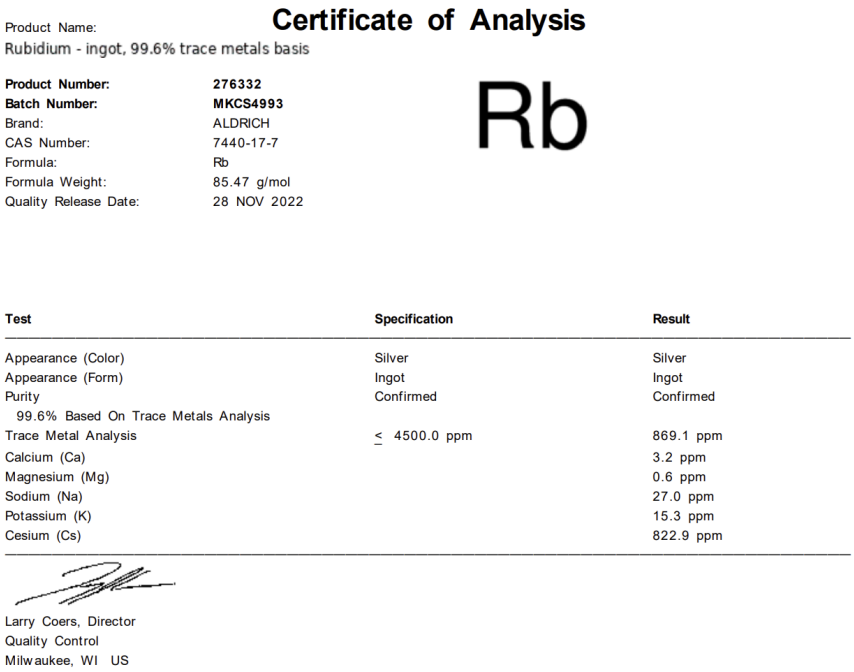


Figure A.3: Sketch of stainless steel strontium reservoir discussed in Sec. 3.5

Appendix B

Rubidium



Certificate of Analysis

Product Name:
Rubidium - ingot, 99.6% trace metals basis

Product Number:	**276332**
Batch Number:	**MKCS4993**
Brand:	ALDRICH
CAS Number:	7440-17-7
Formula:	Rb
Formula Weight:	85.47 g/mol
Quality Release Date:	28 NOV 2022

Rb

Test	Specification	Result
Appearance (Color)	Silver	Silver
Appearance (Form)	Ingot	Ingot
Purity	Confirmed	Confirmed
99.6% Based On Trace Metals Analysis		
Trace Metal Analysis	≤ 4500.0 ppm	869.1 ppm
Calcium (Ca)		3.2 ppm
Magnesium (Mg)		0.6 ppm
Sodium (Na)		27.0 ppm
Potassium (K)		15.3 ppm
Cesium (Cs)		822.9 ppm

Larry Coers, Director
Quality Control
Milwaukee, WI US

Figure B.1: Certificate of Analysis of rubidium used and discussed in this thesis [30]

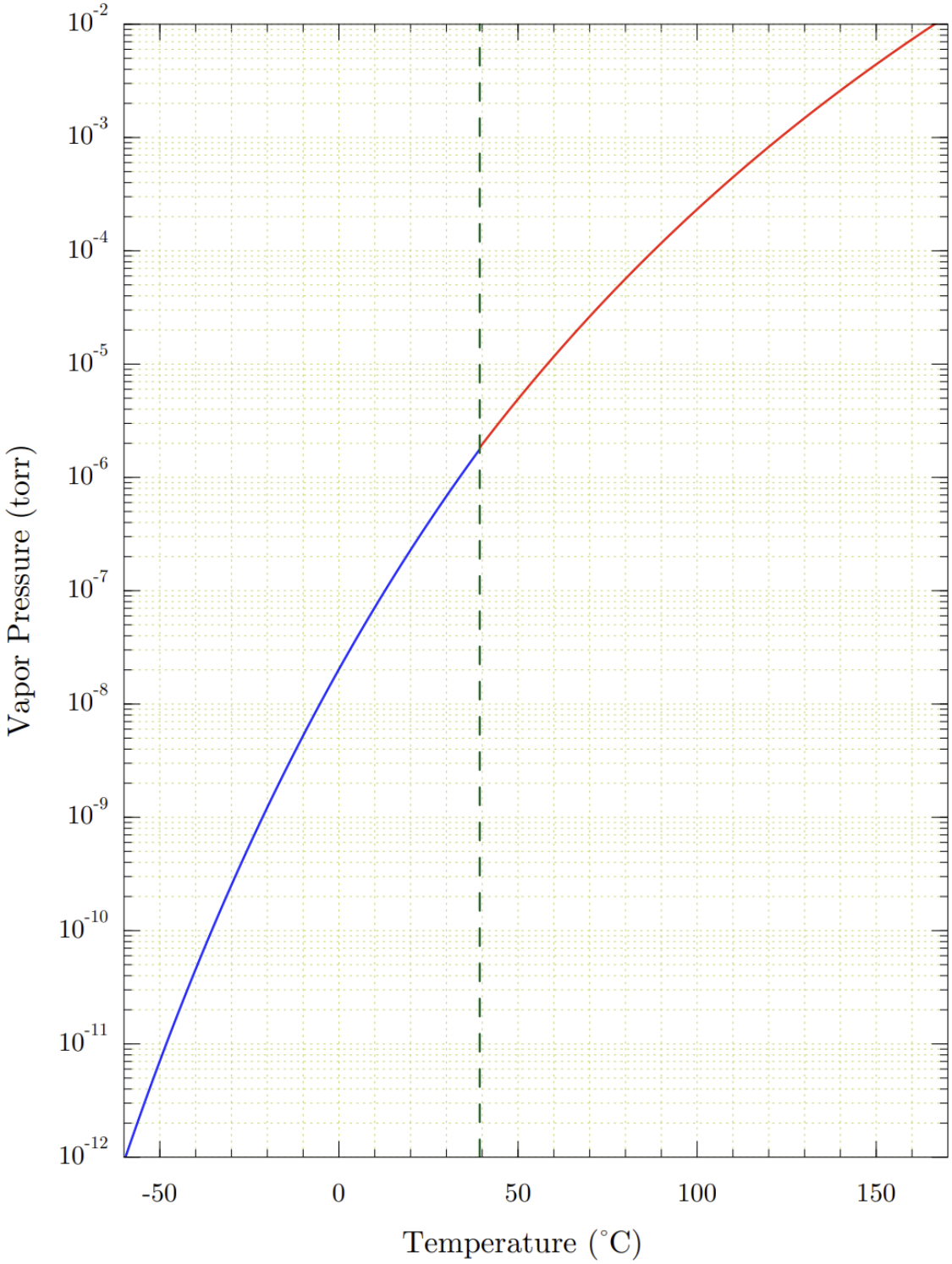


Figure B.2: Rubidium vapor pressure curve [25]

Appendix C

Rubidium Absorption Data

C.0.1 Rb Beam

Fig. C.1 shows the relative absorption data and Lorentzian fits for all probe positions taken when probing a pure Rb beam at Zone 1, 2.46" from the nozzle. Fig. C.2 shows the unfiltered and amplified signal at the 450 position, used to extract the absolute absorption fraction and rescale all other Zone 1 data points to flux.

Fig. C.3 shows the same measurements for a pure Rb beam at Zone 2, 12.3" from the nozzle. Fig. C.4 shows the unattenuated signal at the 500 position, used to rescale all Zone 2 data points to flux.

C.0.2 Rb-Ar Beam

Fig. C.5 shows the relative absorption data and Lorentzian fits for all probe positions taken when probing a mixed Rb-Ar beam at Zone 1, 2.46" from the nozzle. Fig. C.6 shows the unattenuated signal at the 450 position (bypassing the amplifier), used to extract the absolute absorption fraction and rescale all other data points to flux.

C.0.3 Comparison of All Beam Profile Plots

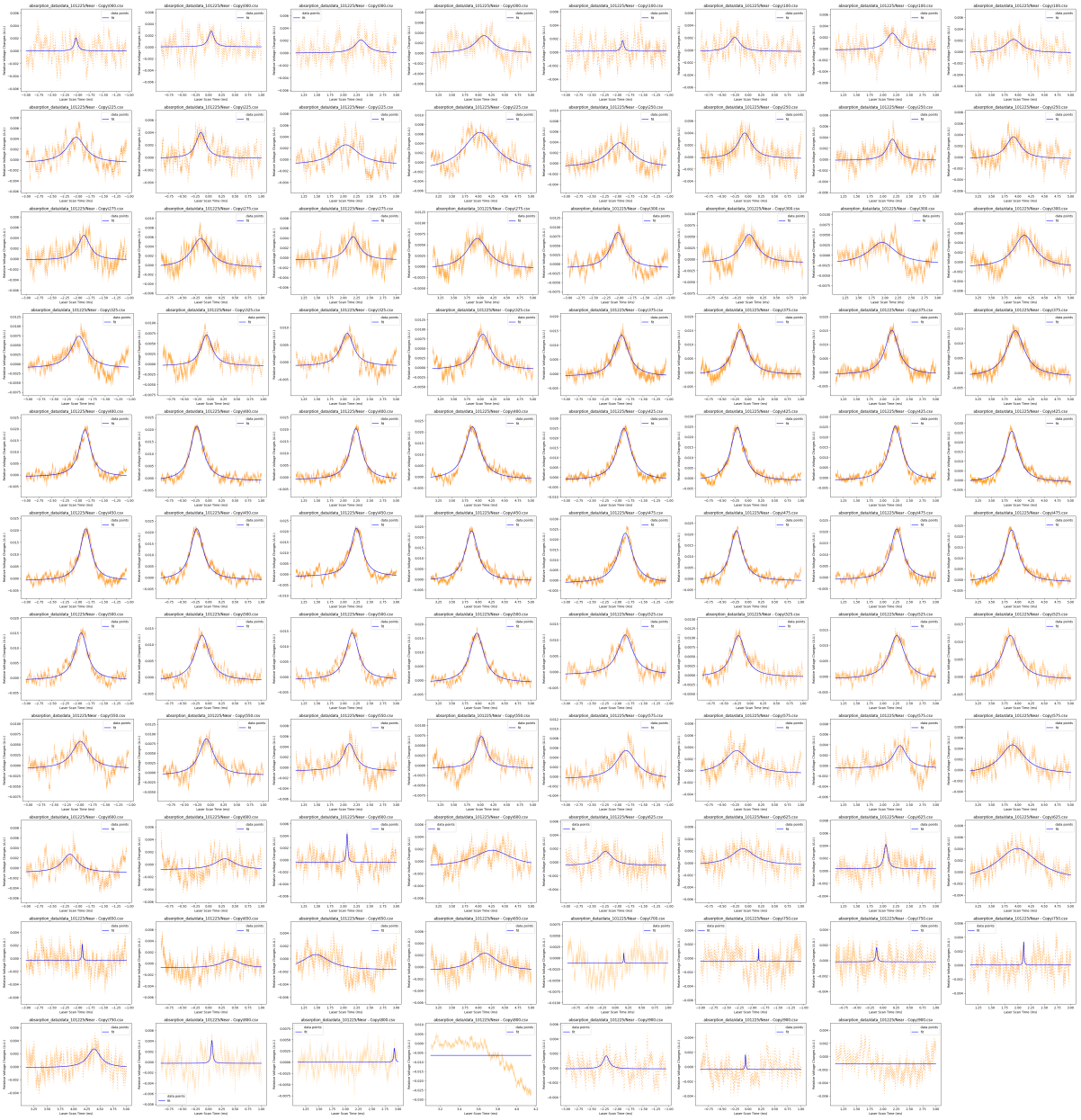


Figure C.1: Pure Rb beam spatial absorption profile at Zone 1 (2.46” from nozzle). Each panel shows the photodetector signal with a Lorentzian fit at a given probe height y.

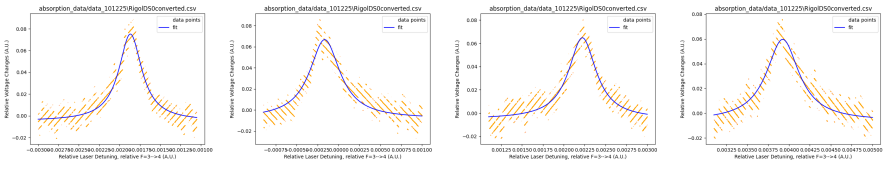


Figure C.2: Unattenuated absorption signal at Zone 1 (probe position 450, bypassing amplifier), used to determine absolute absorption fraction for flux rescaling.

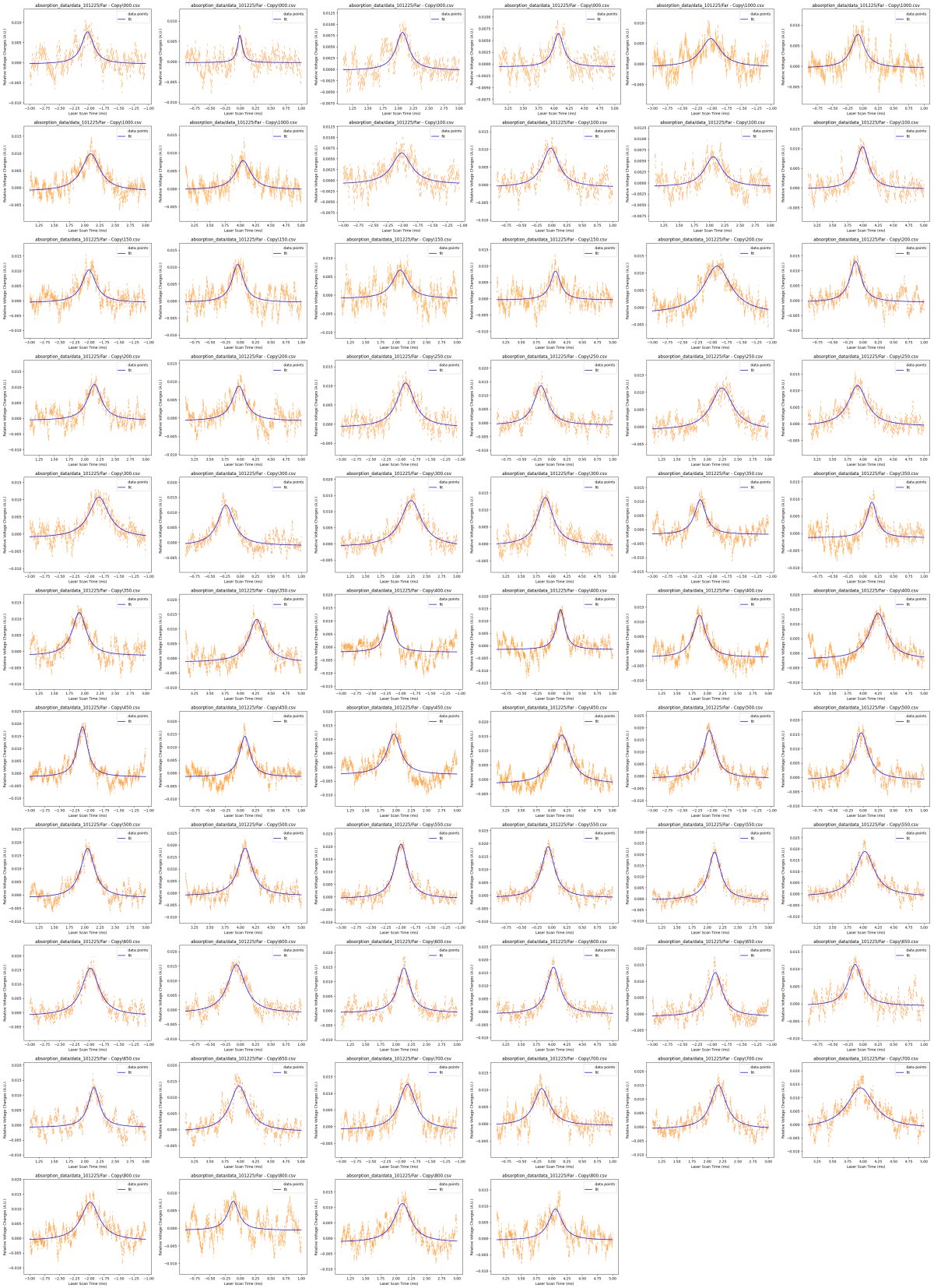


Figure C.3: Pure Rb beam spatial absorption profile at Zone 2 (12.3” from nozzle). Each panel shows the photodetector signal with a Lorentzian fit at a given probe height y.

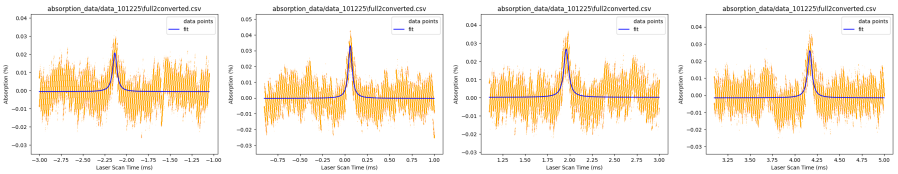


Figure C.4: Unattenuated absorption signal at Zone 2 (probe position 500, bypassing amplifier), used to determine absolute absorption fraction for flux rescaling.

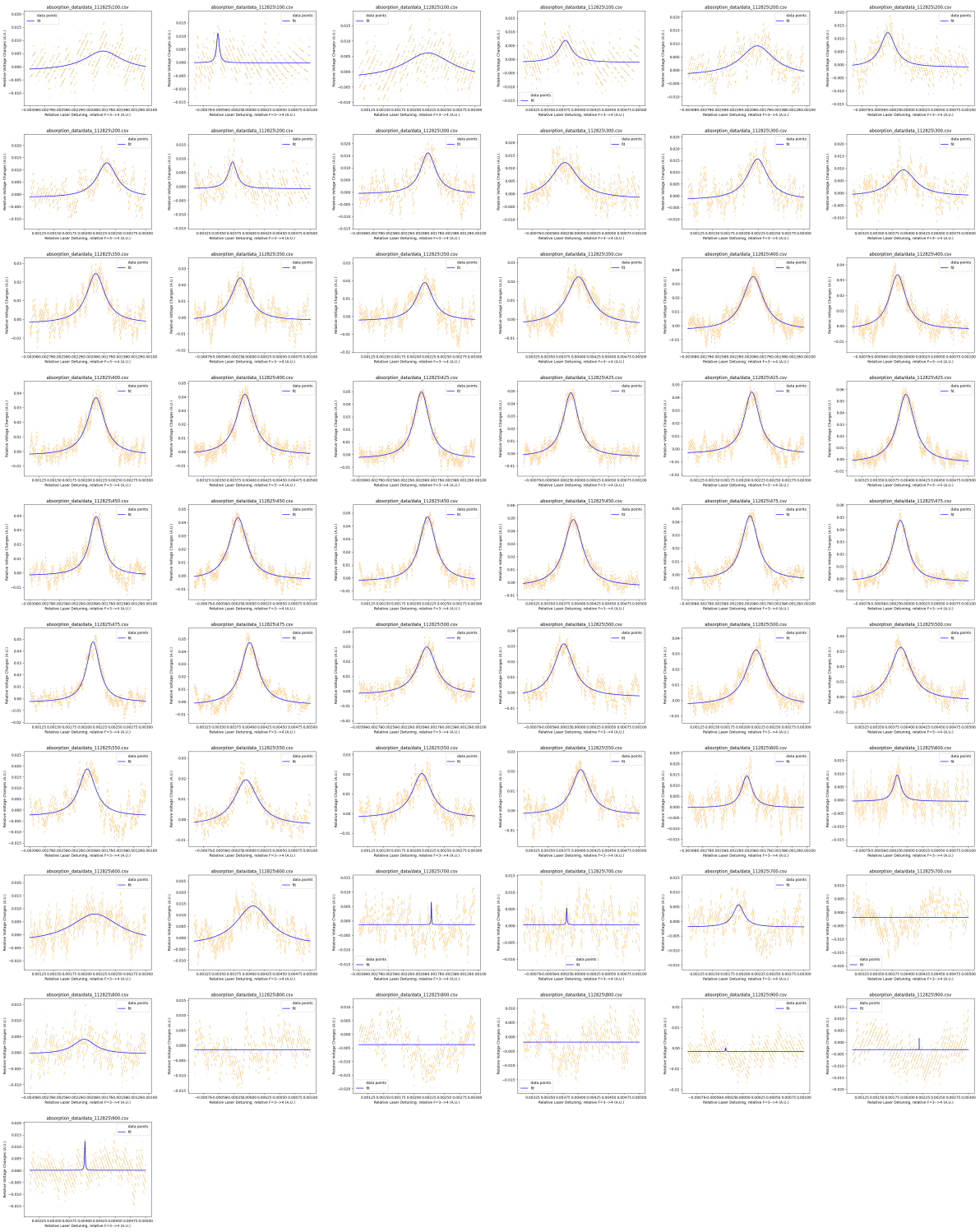


Figure C.5: Mixed Rb-Ar beam spatial absorption profile at Zone 1 (2.46” from nozzle). Each panel shows the photodetector signal with a Lorentzian fit at a given probe height y.

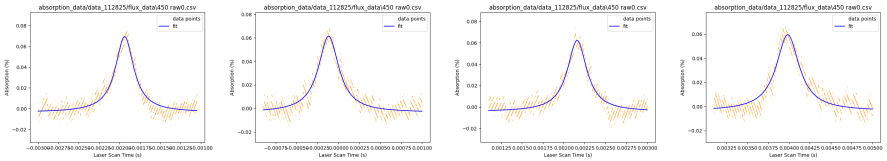


Figure C.6: Unattenuated absorption signal for the Rb-Ar beam (probe position 450, bypassing amplifier), used to determine absolute absorption fraction for flux rescaling.

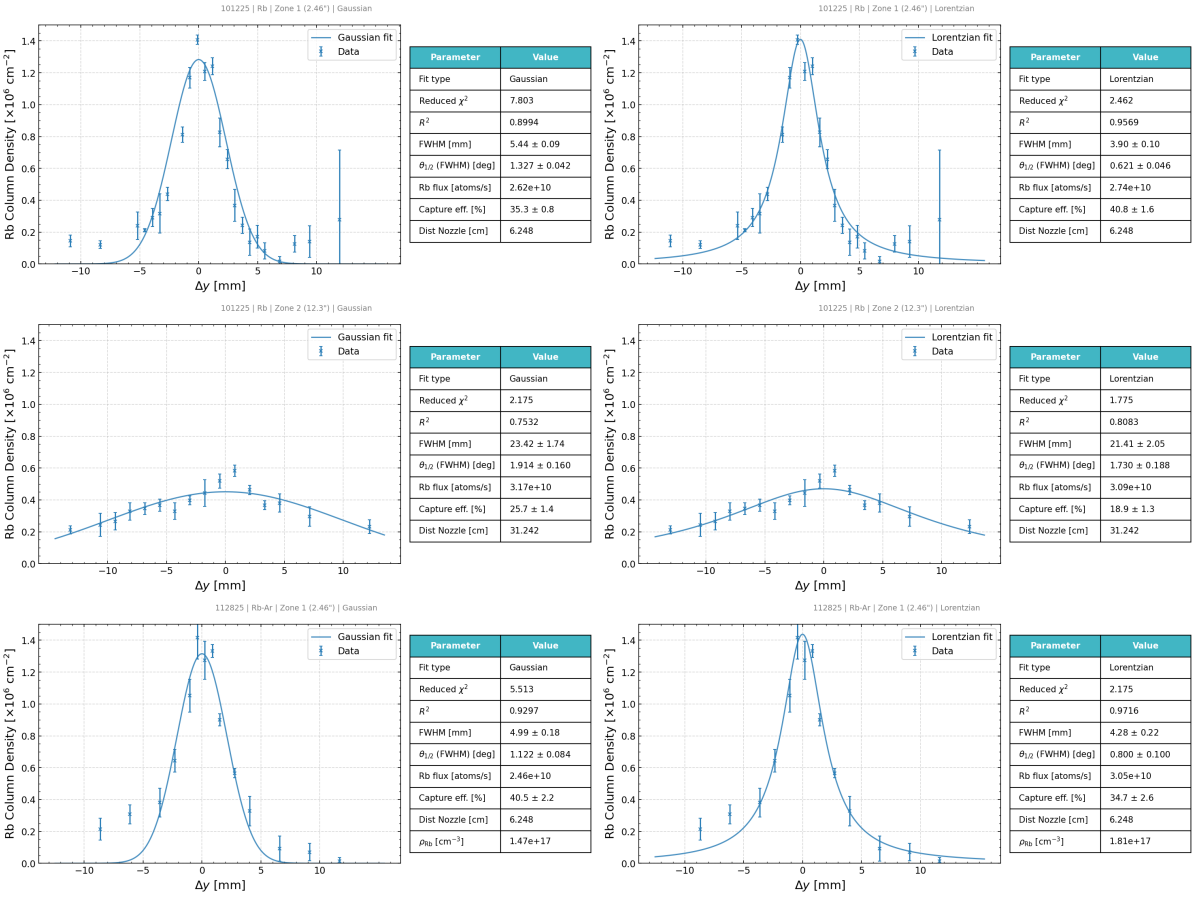


Figure C.7: Overlay of all Rb beam spatial absorption profiles and divergence fits across all measurement runs and zones. Gaussian and Lorentzian fits are shown for direct comparison.

Appendix D

Dipole-Dipole Broadening Monte Carlo Simulation Code

The full Python code used for my spin-spin interaction induced inhomogeneous broadening simulation is show below.

```
"""
broadening_sim.py

ES_APPM 421 Final Project:
Modeling Inhomogeneous Broadening through Spin-Spin Interactions
   in Matrix Isolated Spin Ensembles

Author: Isaac Cross (crossisaac114@gmail.com and/or
   isaaccross2026@u.northwestern.edu)
Date: December 8, 2025
"""

#Import needed packages
import numpy as np
import matplotlib.pyplot as plt
from mpl_toolkits.mplot3d import Axes3D
from scipy.optimize import curve_fit
from fractions import Fraction

#define constants to be used
mu0 = 4*np.pi*1e-7 #permeability of free space T m/A
muB = 9.2740100783e-24 #Bohr magneton,J/T
```

```
h = 6.62607015e-34 #planck's const J*s
gJ = 2.0023 #electron Lande g-factor, assumed free electron (alkali)

B_const = mu0/(4*np.pi) #const prefactor for B from dipole used later


#Define all helper functions to be called in Monte Carlo broadening simulation
"""
space_dopants:
Creates test cell and fills with atoms/dopants

Sec. "Matrix-Isolated Spin Ensemble"
"""
def space_dopants(density_cm3, L_box_nm):
    #get expected number of dopants
    rho_m3 = density_cm3 * 1e6 # dopant density in atoms/m^3
    V_box_m3 = (L_box_nm * 1e-9)**3 # box volume m^3
    N_mean = rho_m3 * V_box_m3 #ave num dopants in our box

    #generate number of actual dopants, assuming a Poisson distribution
    N_dopants = np.random.poisson(N_mean) - 1 #subtract 1 for the central dopant

    #assume random uniform dist in box, positions in nm, spaced from central spin @ (0,0,0)
    dopant_locations = np.random.uniform(
        low=-L_box_nm/2,
        high=L_box_nm/2,
        size=(N_dopants, 3) # Nx3 array. N dopants, at (x,y,z)
    )

    return dopant_locations

"""
```

```
53 lande_gF_factor
54 Calculates the hyperfine Lande g-factor for the spin state we are
       looking at
55
56 Sec. "Spin-Spin Interaction Model"
57 """
58 def lande_gF_factor(J,I,F):
59     return gJ*((F*(F+1.0)-I*(I+1)+J*(J+1))/(2*F*(F+1)))
60
61
62 """
63 zeeman_coeff_calc
64 Calculatye gamma_eff
65 Sec. "Spin-Spin Interaction Model"
66 """
67 def zeeman_coeff_calc(gF_ground,mF_ground,gF_excited,mF_excited):
68     return  muB*(gF_excited*mF_excited-gF_ground*mF_ground)/h #Hz
          /T
69
70
71
72 """
73 magnetization_dopants
74 Sec."Determing Spin States and Oreintation" in writeup
75
76 Uses gFi determined by possible Fi instead of just F as in
       writeup
77 as this is more efficient. Practically they are equivalent.
78 """
79 def magnetization_dopants(size,
80                           gFs, gF_pump, gF_pump_efficiency,
81                           mFs, mF_pump, mF_pump_efficiency,
82                           allignment_efficiency):
83
84     #pick mF for each state with efficiency mF_pump_efficiency to
           end in mF_pump
85     mF = np.empty(size, dtype=float)
86     mF_pumped_mask = np.random.rand(size)<mF_pump_efficiency
```

```
87      mF[mF_pumped_mask] = mF_pump
88      mF[~mF_pumped_mask] = np.random.choice(mFs,size=(~
            mF_pumped_mask).sum())
89
90      #pick gF for each state with efficiency gF_pump_efficiency to
            end in gF_pump
91      gF = np.empty(size, dtype=float)
92      gF_pumped_mask = np.random.rand(size)<gF_pump_efficiency
93      gF[gF_pumped_mask] = gF_pump
94      gF[~gF_pumped_mask] = np.random.choice(gFs,size=(~
            gF_pumped_mask).sum())
95
96      #magnitude of magnetic moment each dopant
97      m_mag = gF * mF * muB
98
99      #Magnetic moment orientation
100     m = np.tile(np.array([0., 0., 1.]), (size, 1))
101     mis = np.random.rand(size) > allignment_efficiency
102     n_mis = mis.sum()
103     if n_mis > 0:
104         #random unit vectors on S^2
105         v = np.random.normal(size=(n_mis, 3))
106         v /= np.linalg.norm(v, axis=1)[:, None]
107         m[mis] = v
108
109     #output final magnetic moment list for all dopants
110     return m_mag[:, None] * m #J/T
111
112
113 """
114 Bz_origin_calc
115
116 Calcualte magnetic field at central test spin caused by all
        neighboring spins
117 Sec. "Spin-Spin Interaction Model" and
118 Sec. "Central Spin's Frequency Shift"
119 """
120 def Bz_origin_calc(dopant_locations, m_dopants):
```

```
121     # Bz given ~ consts*(3rhat(m dot rhat) - m)/rmag^3
122
123     # dopant r is currently relative to origin, but want
124     # magnetic field located at -r relative to dopant
125     R = -dopant_locations*1e-9 #convert from nm to m
126
127     R_mag = np.linalg.norm(R, axis = 1)[:,None] #get magnitude of
            R, will be importnat for Rhat used in B field  calc
128     R_hat = R/R_mag
129
130     m_dot_R_hat = np.sum(m_dopants*R_hat, axis=1)[:,None]
131
132     B_vecs = B_const*(3*m_dot_R_hat*R_hat - m_dopants)/(R_mag**3)
            #get full vector B field from each dipole (N,3)
133     B_z = B_vecs[:,2] #only care about Bz (N,1)
134     B_z_tot = np.sum(B_z) #sum to get total effective B field at
           origin
135     return B_z_tot #T
136
137
138 """
139 lorentzian
140
141 Lorentzian function for fitting
142 Sec. "ANALYSIS"
143 """
144 def lorentzian(v, A, v0, Gamma):
145     return A * (Gamma/2)/((v - v0)**2 + (Gamma/2)**2)
146
147
148 """
149 broadening_simulation
150
151 key to Monte Carlo model of spin-spin interaction and
       corresponding inhomogeneous broadening
152 Uses all helper functions defined above.
153 Sec. "ANALYSIS"
154 """
```

```
155 def broadening_simulation(N,density_cm3,L_box_nm,
156                          J,I,F_ground,mF_ground,
157                          F_excited,mF_excited,
158                          F_pump_efficiency,mF_pump_efficiency,
                                allignment_efficiency,
159                          plot = True):
160 
161     #get coefficients/constants
162     #gF consts
163     gF_ground = lande_gF_factor(J,I,F_ground)
164     gF_excited = lande_gF_factor(J,I,F_excited)
165     #zeem shift coeff
166     zeeman_coeff = zeeman_coeff_calc(gF_ground,mF_ground,
           gF_excited,mF_excited) #Hz/T
167 
168     gFs =[gF_ground,gF_excited]
169     mFs = np.arange(-F_ground,F_ground+1,1)
170 
171     #create empty list to fill with shifts
172     delta_freqs = np.empty(N)
173 
174     #simualte new configuration and calculate shifts N times
175     for k in range(N):
176 
177         dopant_locations = space_dopants(density_cm3, L_box_nm) #
               nm
178 
179         num_dopants = dopant_locations.shape[0]
180 
181         m_dopants = magnetization_dopants(num_dopants,
182                                           gFs, gF_ground,
                                                F_pump_efficiency,
183                                           mFs, mF_ground,
                                                mF_pump_efficiency,
184                                           allignment_efficiency) #J
                                                /T
185 
186         magnetic_field_z = Bz_origin_calc(dopant_locations,
```

```
            m_dopants)  #T
187
188         delta_freqs[k] = zeeman_coeff*magnetic_field_z #Hz
189
190     #convert from Hz to kHz
191     delta_freqs_khz = delta_freqs*1e-3 #kHz
192
193     #get guesses for p0 in lorentzian fit, and set bounds on fit
194
195     #use central 97% of the data as the fitting range
196     low_q, high_q = np.percentile(delta_freqs_khz, [3, 97])
197     padding = 0.1 * (high_q - low_q)
198
199     rangeset = (low_q - padding, high_q + padding)
200
201     # create histogram bins but do NOT use the counts for fitting
202     hist_vals, bin_edges = np.histogram(delta_freqs_khz, bins
            =500, range = rangeset)
203     bin_centers = (bin_edges[:-1] + bin_edges[1:]) / 2
204
205     # initial guesses
206     A0 = max(hist_vals)
207     x0_0 = 0
208
209     indices = np.where(hist_vals >= A0/2)[0]
210     FWHM_est = bin_centers[indices[-1]] - bin_centers[indices[0]]
211     gamma0 = FWHM_est
212
213     popt, pcov = curve_fit(lorentzian, bin_centers, hist_vals, p0
            =[A0, x0_0, gamma0])
214     A, x0, gamma = popt
215
216     T2_star_ms = 1/(np.pi*gamma)
217
218     #determine if we output a plot
219     if plot:
220         #create figrue/plot
221         fig = plt.figure(figsize=(13,6))
```

```
222
223         #plot example dopant dist
224         ax1 = fig.add_subplot(1,2,1,projection="3d")
225         x_nm = dopant_locations[:,0]
226         y_nm = dopant_locations[:,1]
227         z_nm = dopant_locations[:,2]
228
229         ax1.scatter(x_nm, y_nm, z_nm, s=20, label='Neighbor Spins
                ') # neighbor spins
230         ax1.scatter(0, 0, 0, s=60, color='red', label='Central
                Test Spin') # central test spin
231         ax1.legend(loc='upper right', fontsize=10)
232
233         ax1.set_xlabel("x (nm)", fontsize=14)
234         ax1.set_ylabel("y (nm)", fontsize=14)
235         ax1.set_zlabel("z (nm)",fontsize=14)
236         ax1.set_xlim(-L_box_nm/2,L_box_nm/2)
237         ax1.set_ylim(-L_box_nm/2,L_box_nm/2)
238         ax1.set_zlim(-L_box_nm/2,L_box_nm/2)
239
240         ax1.text(
241             0.02, 0.10,0.0,
242             f"Dopant Density: {density_cm3:.1e} atoms/cm ",
243             transform=ax1.transAxes,
244             fontsize=10,
245             va='top',
246             ha='left',
247             bbox=dict(boxstyle="round", fc="white", ec="black",
                    alpha=0.8)
248         )
249
250         ax1.set_title("Example dopant configuration", fontsize
                =24)
251
252         #Plot historgram with relevant output values, T2*, Gamma,
                as well as input paramters.
253         ax2 = fig.add_subplot(1,2,2)
254
```

```
255         ax2.hist(delta_freqs_khz, bins=500,range=rangeset,alpha
                =0.5, label="Monte Carlo Shift Data")
256
257         x=np.linspace(rangeset[0],rangeset[1],2000)
258         ax2.plot(x, lorentzian(x, *popt), 'r-',
259                 label=f"Lorentzian fit\n$\Gamma$={gamma:.3g} (kHz
                    )\n"
260                      f"$T_2^*$ = {T2_star_ms:.3g} (ms)")
261
262         param_text = (
263             f"N = {N}\n"
264             f"L = {L_box_nm} nm\n"
265             f"Density = {density_cm3:.2e}  c m  \n"
266             f"J and I: {Fraction(J).limit_denominator()} and {
                    Fraction(I).limit_denominator()}\n"
267             f"Transition: |{F_ground},{mF_ground}        |{
                    F_excited},{mF_excited}  \n"
268             f"gF_ground = {gF_ground:.4f}\n"
269             f"gF_excited = {gF_excited:.4f}"
270         )
271
272         ax2.text(0.98, 0.95, param_text, fontsize=12,
273                 transform=plt.gca().transAxes,
274                 va='top', ha='right',
275                 bbox=dict(boxstyle="round", fc="white", ec="black
                    ", alpha=0.8))
276
277
278         ax2.set_xlabel(r"$\Delta\nu$ (kHz)", fontsize=20)
279         ax2.set_ylabel("Count", fontsize=20)
280         ax2.legend(loc="upper left", fontsize=12)
281         ax2.set_title("Inhomogeneous Broadening Simulation",
                fontsize=24)
282
283         plt.tight_layout()
284         plt.show()
285
286     # return values so can run simulation and compare results in
```

```
        different document
    return {
        "gamma_kHz": gamma,
        "T2_star_ms": T2_star_ms,
        "delta_freqs_kHz": delta_freqs_khz,
        "F_ground": F_ground,
        "mF_ground": mF_ground,
        "F_excited": F_excited,
        "mF_excited": mF_excited
    }
```

Listing D.1: Python code used to simulate spin-spin-induced inhomogeneous broadening